UQAC

Université du Québec à Chicoutimi

Aluminum Alloys for Additive Manufacturing: Towards Higher Strength Alloys

By

Esmaeil Pourkhorshid

Under supervision of Prof. X.-Grant Chen and co-supervision of Prof. Paul Rometsch

Thesis Presented to Université du Québec à Chicoutimi in Partial Fulfillment of the Requirements for the Degree of Doctor of Philosophy Ph.D.

BOARD OF EXAMINERS:

Professor Mousa Javidani, Department of Applied Sciences at UQAC, President of the board of Examiners
Professor Ehab Elsharkawi, Saint' Mary's University, Halifax, Nova Scotia, External Member of Examiners
Professor Dilip Sarkar, Department of Applied Sciences at UQAC, Internal Member of Examiners
Professor X.-Grant Chen, Department of Applied Sciences at UQAC, Internal Member of Examiners
Professor Paul Rometsch, Rio Tinto Aluminum, Saguenay, Quebec, Internal Member of Examiners

Québec, Canada

Alliages d'aluminium pour la fabrication additive vers des alliages à plus haute résistance

Résumé

La demande croissante de matériaux légers dans les industries de haute technologie a accéléré l'adoption des alliages d'aluminium dans les procédés de fusion sélective par laser (SLM), notamment pour les applications nécessitant des géométries complexes. Les alliages couramment utilisés, tels que l'AlSi10Mg et l'AlSi12, offrent une bonne aptitude au procédé, mais présentent des limitations quant à l'amélioration des propriétés mécaniques après la SLM et les traitements thermiques. En revanche, les alliages d'aluminium à haute résistance présentent une faible aptitude au procédé SLM, ce qui constitue un obstacle à leur large adoption industrielle. Cette étude explore la production d'alliages d'aluminium par le procédé SLM, avec pour objectif de dépasser les propriétés mécaniques des alliages conventionnels comme l'AlSi10Mg. La recherche s'est concentrée sur la conception des matériaux, l'optimisation des paramètres SLM, la caractérisation de la microstructure et l'évolution des propriétés mécaniques. Elle est présentée en trois parties, comme décrit ci-dessous.

Dans la première partie, les effets de divers traitements thermiques sur les propriétés mécaniques et l'évolution microstructurale d'un alliage AlSi10MgMn contenant 0,5 % en poids de Mn, produit par SLM, ont été étudiés. La microstructure a été analysée par microscopie optique, microscopie électronique à balayage (SEM), diffraction des électrons rétrodiffusés (EBSD) et microscopie électronique en transmission (TEM). À l'état brut de fabrication (F), l'alliage présentait une résistance ultime à la traction (UTS) de 486 MPa, une limite d'élasticité (YS) de 299 MPa et un allongement de 10,3 %. Après un traitement T5, l'UTS et le YS ont augmenté à 532 MPa et 386 MPa, respectivement, soit une amélioration remarquable de 30 % du YS par rapport à l'état F. Ces propriétés dépassaient largement celles des alliages AlSi10Mg conventionnels dans les conditions F, T5 et T6. Le traitement T5 a favorisé la précipitation de nanoparticules riches en Si et de précipités à base de MgSi sans perturber le réseau riche en Si. Après un traitement T6, ce réseau a complètement disparu, et la phase de renforcement principale était constituée de précipités à base de MgSi et de dispersoïdes α-Al(Mn,Fe)Si induits par l'ajout de Mn. À l'aide de modèles constitutifs basés sur la microstructure, les contributions des différents composants microstructuraux à la résistance mécanique ont été analysées.

Dans la deuxième partie, l'effet de la modification par le Mn sur les alliages AlSi10Mg produits par SLM a été évalué. Les microstructures dans différentes conditions de traitement thermique ont été analysées par SEM, EBSD, TEM et tomographie par sonde atomique (APT). L'ajout de 0,5 % en poids de Mn a permis d'augmenter la limite d'élasticité (YS) de 17 %, 30 % et 29 % dans les conditions F, T5 et T6, respectivement, par rapport à l'alliage AlSi10Mg standard. Ces améliorations ont été principalement attribuées à une densité accrue de nanoparticules dans les états F et T5, ainsi qu'à l'introduction de la phase

α-Al(Mn,Fe)Si, qui modifie la composition chimique du réseau eutectique riche en Si, améliorant ainsi les propriétés mécaniques globales.

Dans la troisième partie, l'impact des additions de raffineurs de grains TiB sur l'évolution microstructurale, la susceptibilité à la fissuration à chaud et les propriétés mécaniques des alliages Al-Cu 224 a été examiné afin d'améliorer leurs performances en SLM. Une méthode de refusion laser de surface (LSR) a simulé la solidification rapide par laser. Les résultats ont révélé que l'addition de particules TiB2 a éliminé les fissures de solidification, réduisant les tailles de grains de 13-15 µm à 5,5 µm et 3,2 µm avec 0,34 % et 0,65 % en poids de Ti, respectivement. La dureté des alliages modifiés a atteint 117 et 130 HV après un traitement T6, surpassant celle des alliages AlSi10Mg de 15 à 30 %. Cette amélioration est attribuée à la formation de grains fins et de précipités nanométriques θ′/θ″. Cette recherche met en évidence le potentiel des modifications par Mn et TiB pour optimiser les propriétés mécaniques et la processabilité des alliages d'aluminium dans les applications SLM, offrant des solutions prometteuses aux défis associés aux alliages à haute résistance.

Aluminum Alloys for Additive Manufacturing Towards Higher Strength Alloys

Abstract

The increasing demand for lightweight materials in high-tech industries has accelerated the adoption of aluminum alloys in Selective Laser Melting (SLM) processes, particularly for applications requiring complex geometries. Commonly used alloys, such as AlSi10Mg and AlSi12, offer good processability but face limitations in achieving higher mechanical properties after SLM and heat treatments. In contrast, high-strength aluminum alloys exhibit low processability in SLM, presenting a challenge for their widespread industrial applications. This study explores the production of aluminum alloys via the SLM process, aiming to surpass the mechanical properties of conventional AlSi10Mg alloys. The research focused on material design, SLM parameter optimization, microstructure characterization, and the evolution of mechanical properties. It is presented in three parts as outlined below.

In the first part, the effects of various post-heat treatments on the mechanical properties and microstructure evolution of an AlSi10MgMn alloy containing 0.5 wt.% Mn produced by the SLM process were investigated. The microstructure of the samples was analyzed using optical microscopy, scanning electron microscopy, electron backscatter diffraction, and transmission electron microscopy. In the as-manufactured (F) condition, the alloy exhibited an ultimate tensile strength (UTS) of 486 MPa, a yield strength (YS) of 299 MPa, and an elongation of 10.3%. After a T5 treatment, the UTS and YS increased to 532 MPa and 386 MPa, respectively, resulting in a remarkable 30% improvement in YS compared to the F state. These properties were considerably higher than those reported for conventional AlSi10Mg alloys in the F, T5, and T6 conditions. The T5 treatment promoted the precipitation of a large fraction of Si-rich nanoparticles and MgSi-based precipitates without disrupting the Si-rich network. After a T6 treatment, the Si-rich network completely disappeared, and the main strengthening phase was MgSi-based precipitates accompanied by α-Al(Mn,Fe)Si dispersoids induced by the Mn addition. Using microstructure-based constitutive models, the strengthening contributions of various microstructural components to mechanical strength in different processing conditions were analyzed.

In the second part, the effect of Mn modification on AlSi10Mg alloys produced by the SLM process was assessed. The microstructures in different heat treatment conditions were analyzed using optical microscopy, scanning electron microscopy, electron backscatter diffraction, transmission electron microscopy, and atom probe tomography. The investigation revealed that compared to a standard AlSi10Mg alloy, an alloy with a 0.5 wt% Mn addition exhibited yield strength (YS) increases of 17%, 30%, and 29% in the as-manufactured (F), T5, and T6 heat treatment conditions, respectively. The study attributed these enhancements mostly to the increased number density of nanoprecipitates in the F and T5 conditions. Moreover, the improvement in YS under the F and T5 conditions was attributed to the introduction of the α-Al(Mn,Fe)Si phase, which alters the Si-rich eutectic

network by modifying its chemical composition, thereby enhancing the overall mechanical properties. After a T6 heat treatment, the Si-rich eutectic network completely disappeared in both alloys, but α-Al(Mn, Fe)Si dispersoids provided an extra strengthening contribution in the Mn-modified alloy. This research highlights the potential of Mn modification to optimize the mechanical properties of AlSi10Mg alloys fabricated via SLM, offering significant benefits for the design and application of high-strength, lightweight aluminum alloys.

In the third part, the impact of TiB grain refiner additions on the microstructural evolution, hot tearing susceptibility, and mechanical properties of Al-Cu 224 alloys was examined to enhance their processing performance in the SLM process. A simple laser surface remelting method (LSR) was utilized to simulate the laser-based rapid solidification. The results revealed that the addition of appropriate amounts of TiB grain refiner could completely eliminate the solidification cracks during the LSR. The introduction of TiB_2 particles in the melt pools through the TiB grain refiner changed the grain morphology from a coarse columnar to a fine equiaxed structure, and the grain sizes were reduced from 13-15 μm in the base alloys to 5.5 μm and 3.2 μm in the alloys with 0.34 wt% Ti (B-3TiB) and 0.65 wt% Ti (ZV-6TiB) additions, respectively. The hardness values of the modified B-3TiB and ZV-6TiB alloys reached 117 and 130 HV after a T6 heat treatment, which surpassed the hardness of conventional AlSi10Mg alloys by at least 15-30%. This improvement was attributed to the finer grains and to nanoscale θ′/θ″precipitation. The results demonstrate that the TiB grain refiner addition can significantly improve the processability and mechanical properties of Al-Cu 224 alloys for SLM applications, offering a promising solution to the challenge of high hot tearing susceptibility in high-strength aluminum alloys.

Table of Contents

List of Tables

List of Figures

List of Abbreviations

AM	Additive Manufacturing
APT	Atom Probe Tomography
BF	Bright Field
CAD	Computer-Aided Design
EBSD	Electron Back-Scatter Diffraction
EDS	Energy Dispersive Spectrometry
EDv	Volumetric Energy Density
FCC	Face Cubic Center
GND	Geometrically Necessary Dislocation
GRF	Growth Restriction Factor
HAZ	Heat Affected Zone
HTIE	Easton's Hot Tearing Index Criteria
ICP	Inductively Coupled Plasma
IPF	Inverse Pole Figure
LAM	Laser Additive Manufacturing
LEAP	Local Electrode Atom Probe
LPBF	Laser Powder Bed Fusion
MPB	Melt Pool Boundary
MPC	Melt Pool Center

OM	Optical Microscopy
SADP	Selected Area Diffraction Pattern
SEM	Scanning Electron Microscopy
SLM	Selective Laser Melting
SR	Stress Relief
TEM	Transmission Electron Microscopy
UTS	Ultimate Tensile Strength
XRD	X-Ray Diffraction
YS	Yield Strength

List of Symbols

Al	Aluminum
b	Burgers vector
Cu	Copper
d_{pre}	Diameter of Equivalent Spherical Particles
ED_l	Linear energy density
Er	Erbium
F	Mean interaction force
f_{Al}	Volume Fractions of the aluminum matrix
Fe	Iron
f_{si}	Volume Fractions of the Si-Rich Network
f_v	Volume fraction
G	Shear modulus
h	Hatch distance
M	Taylor factor
Mg	Magnesium
Mn	Manganese
MPa	Megapascal
Ni	Nickel
N_v	Number density

P	Laser power
Sc	Scandium
Si	Silicon
t	Powder layer thickness
Ti	Titanium
v	Scan speed
V	Vanadium
Zr	Zirconium
α	Coefficient of thermal contraction
γ	Surface tension
ε	Thermal contraction
θ	Strain hardening rate

Dedication

To my parents (Pari and Javad),

For your unconditional love, unwavering support, and endless sacrifices that have shaped who I am today. Your belief in me has been my guiding light.

Acknowledgment

First and foremost, I am deeply grateful to God, whose blessings and guidance have been my source of strength and perseverance throughout this journey.

I would like to express my heartfelt gratitude to my supervisor, Professor X.-Grant Chen, for providing me with the rare opportunity to be part of his research group. His invaluable guidance, support, scientific insights, and encouragement have been instrumental in shaping my research skills and character. His dedication and confidence in me have been a constant source of motivation during this challenging journey.

I am profoundly thankful to my co-supervisor, Prof. Paul Rometsch, for his invaluable support, technical expertise, and insightful guidance during my collaboration with Rio Tinto. His mentorship has been pivotal in my growth as a researcher, and I greatly appreciate his patience and constructive feedback.

I would also like to thank the Centre de Métallurgie du Québec (CMQ) for providing the resources and opportunities to work with their SLM machine and for supplying the samples necessary for this research.

I would like to take this opportunity to sincerely thank the members of my jury for their time, insightful feedback, and valuable contributions to my thesis. I am deeply grateful to Prof. Dilip Sarkar and Prof. Mousa Javidani for their guidance and encouragement throughout this journey. Your thoughtful input and constructive advice have greatly enhanced the quality of my work. I also wish to extend my heartfelt thanks to Prof. Ehab Elsharkawi, who graciously served as the external jury member. Your valuable insights and detailed review have provided an external perspective that has significantly strengthened my research.

A special word of thanks to Prof. Mousa Javidani for your support and encouragement, and for introducing me to this university. Your belief in my potential has been instrumental in my academic progress.

I am deeply grateful to my colleagues and friends for their collaboration, insightful discussions, and unwavering support. I would also like to extend my special thanks to the experts at CURAL, Dr. Zhan Zhang and Mr. Zhixing Chen, for their invaluable assistance with characterization analyses in SEM and TEM.

To my beloved family—my father, mother, sister, brother-in-law, and cherished nephew—thank you for your endless sacrifices, love, and support, which have been my cornerstone throughout this journey. To my love, your unwavering encouragement and belief in me have been my anchor, and I am forever grateful for your presence in my life.

I would like to sincerely thank my dear friends for their unwavering support, kindness, and encouragement. Your presence, thoughtful words, and belief in me have made

all the difference during both challenging and joyful times. I am deeply grateful for the shared moments of laughter and comfort, and for reminding me that I was never alone on this path.

Finally, I extend my deepest gratitude to everyone who has contributed in various ways to the successful completion of this thesis. Your support, whether big or small, has made a significant difference. I apologize if I have, by mistake, omitted anyone, but please know that your contributions are deeply appreciated.

Chapter 1

Introduction

1.1 Background

The increasing demands for improved fuel economy and reduced greenhouse gas emissions have become key motivators for industries to produce lightweight products. Additionally, weight reduction can enhance recyclability performance. A promising strategy is to develop and utilize lightweight, high-performance materials as alternatives to traditional industrial materials like cast iron and steel [1-4]. Aluminum (Al) is one of the lightest metals, and its alloys are recognized for their exceptional corrosion resistance, high specific strength, excellent low-temperature performance, low density, good machinability and formability, low cost, good maintainability, and ease of extrusion molding. These attributes make aluminum alloys preferred materials in various industrial applications, including vehicle, marine, bridge construction, large-span roofing, aerospace, energy systems, and curtain wall systems [5-7].

Eco-friendly manufacturing, also known as eco-manufacturing, is crucial for the sustainable growth and development of global industries. Presently, industrial manufacturing processes account for 15% of global energy consumption and 35–40% of global material consumption [8]. Reducing energy and resource consumption in this sector is essential for advancing global sustainability. The growing concerns about climate change, the scarcity of natural resources, and the resulting ecological impacts have increased the popularity of eco-manufacturing, paving the way for future industrial development [9]. Over the past two

decades, additive manufacturing (AM) technologies have been increasingly utilized to produce end-use parts by fabricating components from selected materials layer by layer, which can be considered as eco-manufacturing compared to traditional manufacturing processes like casting, forging, extrusion, and powder metallurgy [10]. AM enables the production of parts with complex geometries that are challenging to achieve with conventional manufacturing processes. Additionally, AM offers numerous sustainable advantages, as it does not require dies, cutting tools, or lubricants. Recent studies have shown that AM has significant potential to reduce energy consumption and material waste during the manufacturing process [11, 12].

Recently, aluminum alloys have attracted tremendous attention in additive manufacturing fields for their outstanding properties [13-15]. The relatively mature available system for AM of aluminum is mainly Al-Si cast alloys, including AlSi10Mg and AlSi12 [16]. Al-Si alloys can achieve good performance in AM due to their good fluidity and weak tendency to shrinkage, hot cracking, and cold cracking. Combining the additive manufacturing process with the development of high-strength Al alloys can be a novel approach for improving the mechanical properties of Al alloys, while also increasing the efficiency and reducing greenhouse gas emissions in both aspects of materials and manufacturing.

1.1.1 Additive Manufacturing

Additive manufacturing (AM) refers to a materials fabrication process that creates objects from 3D model data, typically layer by layer, unlike subtractive manufacturing

methodologies, which primarily involve material removal, such as machining. This innovative procedure is also known by several other terms in the industry, including additive fabrication, additive processes, additive techniques, additive layer manufacturing, layer manufacturing, and freeform fabrication. While the term '3D printing' is increasingly used as a synonym for additive manufacturing, the latter is more accurate as it describes a professional production technique that differs significantly from conventional subtractive methods like machining. While machining is a top-down process where the material starts with a bulk workpiece and is removed to create the final part, additive manufacturing is inherently a bottom-up process. This method allows for building materials into freeform geometries layer by layer. By adding materials from the bottom up, the need for tooling in other manufacturing processes can be eliminated. Over the past few decades, the cost and complexity of products have changed drastically due to the advantages of this new manufacturing method. Figure 1-1 [17] illustrates schematically the conventional bulk forming processes of injection molding, subtractive manufacturing, and additive manufacturing. AM system can be classified in terms of the material feedstock, energy source, build volume, etc. Currently, various AM technologies have been developed, including the key laser additive manufacturing (LAM) method of laser powder bed fusion (LPBF), which is also known as selective laser melting (SLM) [18].

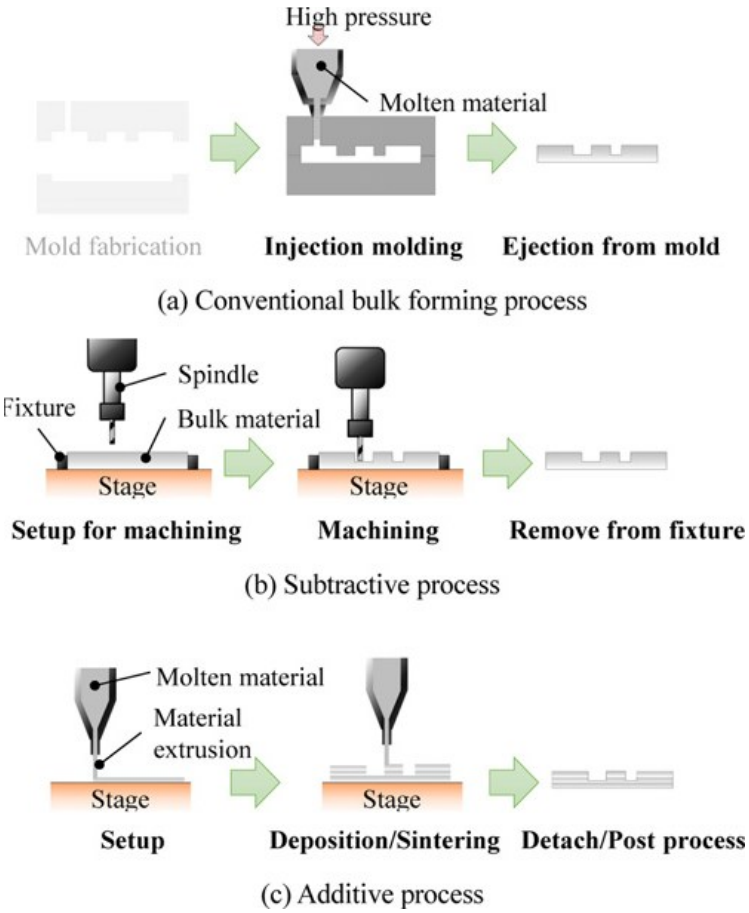

Figure 1-1: Schematic diagram of the three manufacturing processes a) Conventional bulk forming process, b) Subtractive manufacturing, c) Additive manufacturing [17].

1.1.2 Laser Powder Bed Fusion (LPBF)

Laser powder bed fusion (LPBF), also known as selective laser melting (SLM), is an AM technology that uses a laser as an energy source to melt metal powder. In this process, the powder material is evenly spread on the forming platform, and a laser beam is used as the heat source. The powder is irradiated and melted along a predetermined path. As the melted powder cools, it solidifies, and new powder layers are spread, melted, and solidified, layer by layer, until the entire part is completed [19, 20]. The schematic diagram of the SLM process is shown in Figure 1-2 [21]. This process was first developed for high-strength metals

like superalloys and titanium (Ti). In the past decade, the adoption of this process for aluminum alloys has significantly increased. This trend is illustrated in Figure 1-3, which shows the number of published papers on the topic of SLM. The graph clearly indicates that while papers on SLM for other metals began to be published two decades ago, the use of SLM for aluminum alloys has increased in recent years.

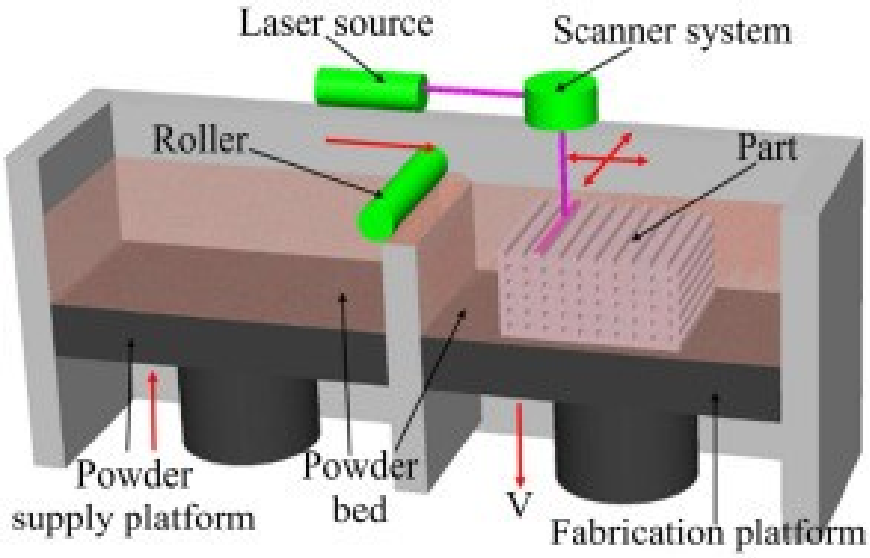

Figure 1-2: A schematic showing the Selective Laser Melting process [21].

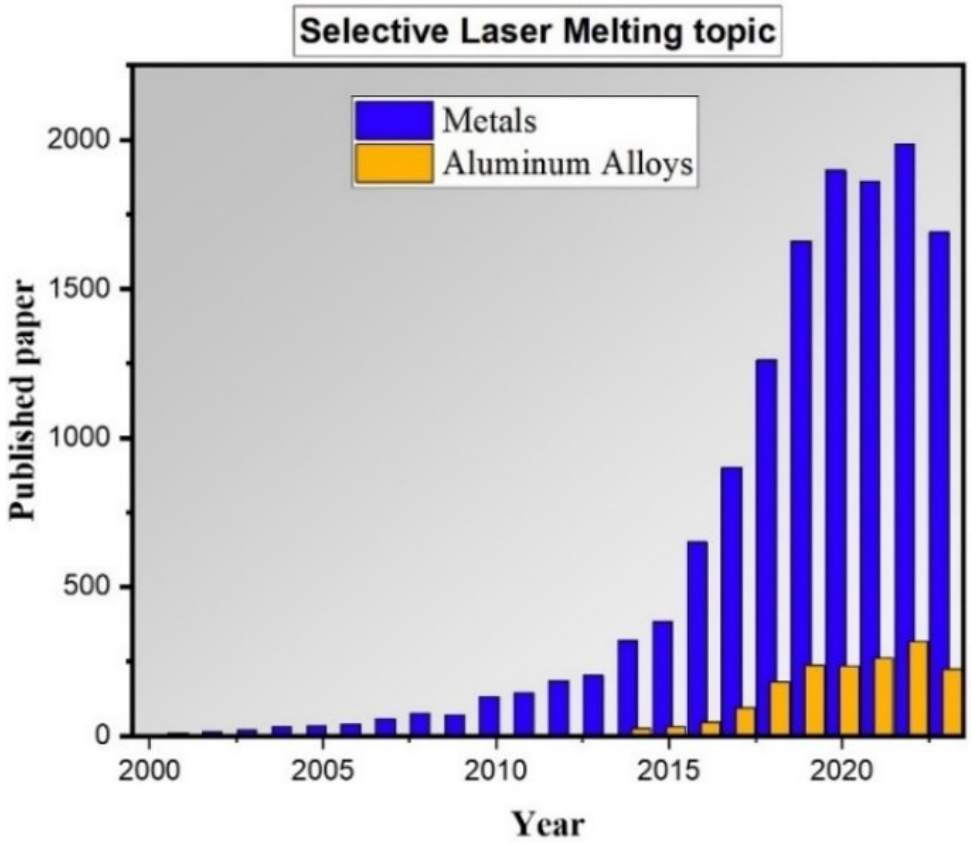

Figure 1-3: Number of published papers on the topic of SLM in recent years.

The parameters for SLM are typically divided into four main categories: laser-related, scan-related, powder-related, and temperature-related [22]. Optimal parameters are required to achieve a fully dense product, and they can vary depending on the specific machine and material used. Among all of the parameters, energy density is often considered the most significant factor for optimizing the process and achieving a fully dense final product.

The most commonly used form of energy density in the literature is the volumetric energy density (EDv, J/mm^3), which is calculated as follows [16]:

$$ED_v = \frac{P}{v\,h\,t} \qquad (1)$$

where P is the laser power, v is the scan speed, h is the hatch distance (the distance between consecutive laser scans), and t is the powder layer thickness during each spreading.

1.1.3 Overview of SLM manufactured aluminum alloys

The application of Al alloys in SLM remains relatively limited despite their widespread availability. The primary reason is that, unlike Ti and other high-strength metals, aluminum is easier to machine, and the production costs of Al parts are relatively low. As a result, manufacturing Al parts through SLM often offers little commercial advantage. However, recent developments highlight the growing demand for aluminum alloys in specialized high-tech applications, particularly in the aerospace industry. The capability of SLM to produce complex geometries from aluminum alloys makes it a viable choice for these applications.

Although SLM provides substantial advantages for aluminum alloy manufacturing, it also poses challenges that may impede the production process. These challenges include the presence of natural oxide films, residual stresses, high reflectivity, high thermal conductivity, low laser absorptivity, porosity, and hot tearing caused by the rapid solidification inherent to the SLM process [16, 23]. Addressing these challenges is critical to expand the range of aluminum alloys that can be effectively used in SLM.

Currently, the most commonly used aluminum alloys in SLM are high-Si alloys, particularly AlSi10Mg. These alloys are favored due to their good weldability and excellent castability, which result from the presence of a significant proportion of low-melting-point

Al-Si eutectic [18, 24]. During SLM, the solidification mechanism of these alloys is cellular-dendritic. A high-velocity solidification front and constitutional undercooling, both characteristic of SLM, promote the formation of a cellular structure, in which α-Al solidifies first, leaving residual Si to segregate at the cellular boundaries [25, 26]. However, the mechanical properties of high-Si aluminum alloys are considerably lower than those of high-strength aluminum alloys, such as the 2xxx and 7xxx series [27, 28]. This gap is illustrated in Figure 1-4 emphasizing the importance of utilizing high-strength alloys to enhance material efficiency after SLM.

Most high-strength aluminum alloys from the traditional 2xxx and 7xxx wrought alloys face significant challenges during SLM due to extensive cracking issues. These challenges arise from their large solidification range, columnar dendritic growth, and directional grain structure, all of which contribute to the formation of hot cracks or hot tears that impede full material consolidation [29-32]. This underscores the need for innovative solutions to address these limitations. For instance, the AA-7075 alloy is highly prone to hot cracking during rapid solidification, resulting in poor weldability and limited compatibility with SLM [33].

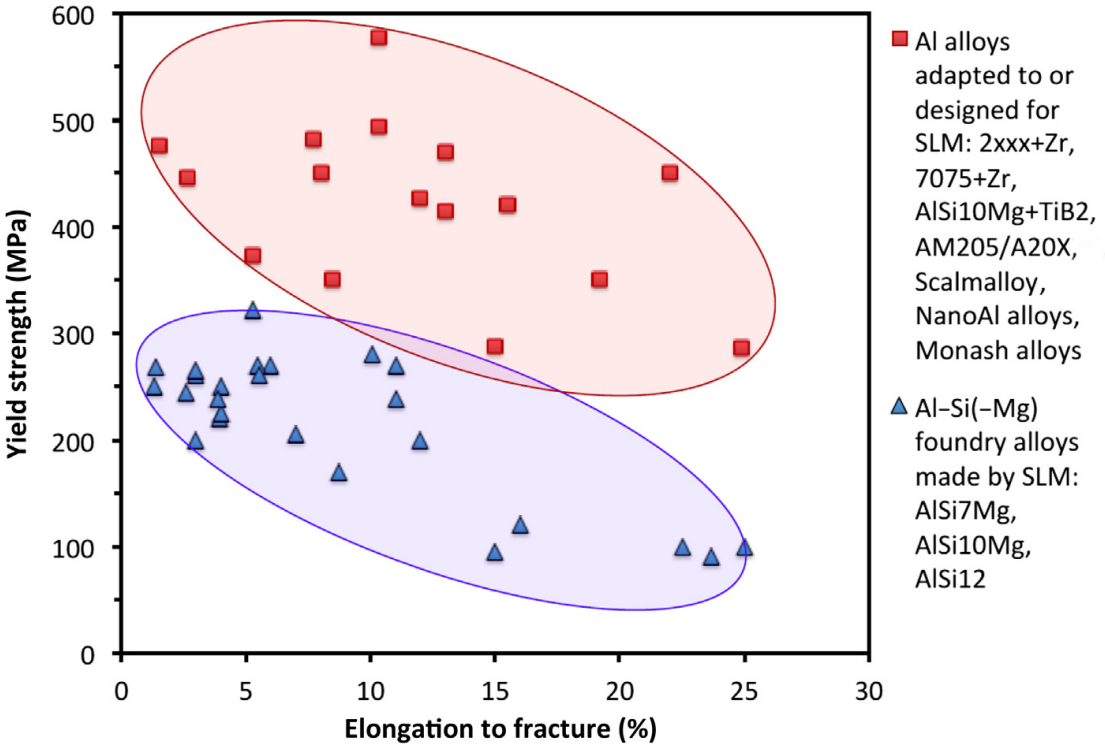

Figure 1-4: Tensile properties of a wide range of aluminum alloys fabricated by SLM, showing alloys borrowed from among AlSi(Mg) foundry alloys (blue) and other alloys for SLM (red) [27].

1.1.4 Typical SLM defects in aluminum alloys

Defect formation in components produced by SLM presents a major challenge, especially for applications that demand high structural integrity and resistance to cyclic loading. A comprehensive understanding of defect formation mechanisms is essential to optimize process parameters specific to the alloy system and processing conditions. This understanding is critical to ensure the reliability and performance of SLM-fabricated Al alloys in demanding engineering applications. The literature identifies four categories of defects and their associated consequences in aluminum alloy components produced using SLM: porosity, defects related to hot cracking, material anisotropy, and surface quality

imperfections. Among these, the porosity and hot cracking are the most critical and have the greatest attention [16, 34, 35].

- **Porosity**

Porosity is one of the most frequent defects in SLM parts, regardless of the materials. Most material qualification studies usually begin with the objective of minimizing porosity in fabricated components. In the case of aluminum alloys, SLM samples often exhibit significant porosity due to the material's low laser absorptivity, which reduces melt efficiency during processing [16, 36, 37]. Porosity in SLM-produced components can be classified into two types: small spherical metallurgical pores and larger irregular pores. The former is attributed to the presence of moisture on the surface of the starting aluminum powder. The latter, often disc-shaped, is associated with a lack of fusion during the process and typically contains unmelted powder particles. Insufficient or excessive energy density can result in porosity formation. Low energy density causes incomplete melting of the metal powder, while excessive energy density leads to overburning and droplet splashing. These issues disrupt powder spreading and the melting of subsequent layers, ultimately leading to pore formation. Porosity defects can be effectively mitigated through the optimization of the SLM process [35, 38].

- **Hot cracking**

High-strength aluminum alloys are prone to extensive cracking when processed by SLM due to the rapid cooling rates associated with the melting and solidification dynamics of the process. These alloys are highly susceptible to hot cracking during fast solidification, resulting in poor processability. Additionally, the presence of pores can worsen cracking through the notch effect [29, 30]. It has been reported that in 2024 aluminum samples, higher

cracking intensity occurs when high laser power (P) and laser speed (v) are used. In contrast, reducing the values of P and v significantly minimizes cracking [29]. An effective approach to mitigating defects in 6xxx aluminum alloys during SLM is the use of an interlayer pause (IP) [39]. This study has shown that an IP time of 8 seconds can release thermal stress and disrupt the continuous growth of intergranular liquid films, resulting in the elimination of hot cracks and a significant reduction in porosity. However, excessively prolonged IP times can lead to the formation of long horizontal lath-like cracks, identified as lack-of-fusion defects between layers, due to insufficient heat accumulation. These studies highlight the importance of optimizing SLM parameters to balance thermal management and defect and hot tearing prevention.

1.1.5 Possible avenues for SLMed aluminum alloys with improved processability and mechanical properties

As mentioned in Section 1.1.3, the most commonly used aluminum alloys in the SLM process offer moderate mechanical properties. Recent research has primarily focused on enhancing the mechanical properties of aluminum alloys produced using SLM and mitigating hot tearing. The majority of these studies can be classified into two main approaches: (1) producing composite materials with reinforcements [40, 41], and (2) modifying the chemical composition by alloying with different elements [42-45].

- **Composite Materials**

Composite materials have been reported to have impressive mechanical properties. However, the laser energy input during SLM significantly affected the densification behavior

of composite parts, and hence increased the difficulty of producing defect-free SLM parts [40]. Zhou et al. studied how the joint incorporation of Si and TiB_2 enhances the hot cracking resistance of the 7xxx alloy [46]. Si enhanced the alloy's fluidity to minimize solidification shrinkage, while TiB_2 proved stable during SLM, acting as a nucleating agent. These effects can help manage the cracking in the modified 7xxx alloy. The study of ZrO_2/AlSi10Mg composites formed by SLM showed that ZrO_2 can effectively improve the strength and toughness of AlSi10Mg [47]. It is reported that the combined action of fine grain strengthening and dispersion strengthening increases the hardness of the composite to 139 HV, showing a 10.3% improvement, while the elongation increases by 41%. The effect of the addition of TiB_2 microparticles to Al-12Si during SLM was studied by Xi et al [48]. It is reported that the additional strengthening observed in the Al-12Si/TiB_2 SLM samples is mainly due to the elimination of the crystallographic texture and the small grain size. The relationship between TiC nanoparticle inoculation and grain refinement of AA2024 Al alloy during the SLM was investigated by Fan et al [49]. This study has shown that incorporating TiC nanoparticles can facilitate the transition from columnar to equiaxed grains in SLMed AA2024 aluminum alloy and increase the processability of modified alloys.

- **Chemical Composition Modifications**

Modifying the chemical composition has been extensively employed to enhance mechanical properties and minimize hot tearing in aluminum alloys. For example, the scandium (Sc) addition improved the tensile strength of AlSi10Mg, primarily due to grain refinement and the refining of eutectic Si [43]. Martin et al. [42] reported that the remarkable hardness improvement in an AlSi10MgCu alloy compared to its AlSi10Mg counterpart was attributed to reduced cell size, a high concentration of nanosized precipitates, and the

presence of shearable Cu-based GP zones. According to Zhang's results [45], the incorporation of Er into the molten pool of AlSi10Mg led to the formation of Al_3Er precipitates, which impeded the epitaxial growth of columnar crystals, and thus refined the grains along the boundaries of the molten pool. Benoit et al. [50] studied the effect of minor Fe additions on the solidification crack susceptibility of the Al-6060 alloy. The results showed that increasing Fe content to 0.5 wt% effectively reduced crack susceptibility, with no cracks observed in any processing conditions for the 6060 + 0.5Fe alloy. This improvement was attributed to the formation of a network of interconnected and branched α-AlFeSi intermetallic particles, which promoted the transition from columnar to equiaxed grains. Furthermore, a 2 wt% Zr addition to the base Al-Cu-Mg alloy was found to significantly reduce cracks during SLM [51]. Zr acted as a grain refiner, effectively preventing crack formation and propagation.

1.2 Problem statement

To date, research on aluminum-based alloys produced via SLM has predominantly focused on castable and weldable alloys, particularly AlSi10Mg. Despite extensive studies on AlSi10Mg during SLM, its mechanical properties remain limited compared to high-strength alloys (Figure 1-4), making it less suitable for high-performance applications. This limitation highlights the need for alloy modifications to improve its mechanical performance. Additionally, the relationship between microstructure and mechanical properties, both in existing and modified alloys, is still not fully understood, necessitating further investigation.

Although several strategies have been investigated to improve the mechanical properties of AlSi10Mg, the use of Mn modification to enhance its mechanical properties has not yet been reported. The potential impact of Mn-dispersoids on mechanical performance in both the as-manufactured condition and under different heat treatment conditions remains unexplored. Previous studies involving Cu, Ni, and Sc modifications have demonstrated the feasibility of enhancing the alloy's mechanical properties post-SLM, suggesting a promising direction for future research on alloy modification.

To date, although numerous high-strength aluminum alloys have been modified to enhance their processability during SLM, there is no available literature on the hot tearing susceptibility of Al-Cu 224 cast aluminum alloy during SLM. Previous studies have demonstrated that controlling the grain structure during SLM is an effective approach to controlling the hot tearing susceptibility of high-strength aluminum alloys. This highlights a promising opportunity to investigate the optimization of modified 224 aluminum alloy to improve its compatibility with the SLM process.

1.3 Objectives

The primary objective of this study is to develop high-strength aluminum alloys suitable for SLM applications. The research focuses on enhancing the mechanical properties of SLM-produced AlSi10Mg and improving the processability of 224 alloy through chemical composition modification and heat treatment. Additionally, it aims to explore the microstructural factors that influence these properties. This research is divided into three topics with the following specific sub-objectives:

1. Evolution of Mechanical Properties and Microstructure of Selective Laser Melted AlSi10MgMn Alloy with Different Post Heat Treatments

I. Study the effect of heat treatment on mechanical properties of SLM-produced AlSi10MgMn alloy.

II. Study the effect of different heat treatments on the microstructural evolution of AlSi10MgMn alloy after SLM.

III. Study the strengthening mechanisms using a classical constitutive model.

2. Effect of Mn on Microstructural Characteristics and Mechanical Behavior of AlSi10Mg Alloys Produced by Selective Laser Melting

I. Study the effect of Mn on the evolution of microstructure and mechanical properties by heat treatments.

II. Investigate the effect of Mn-modification on mechanical properties and fracture behavior.

III. Compare the microstructure and mechanical properties between the conventional AlSi10Mg and Mn-modified alloys.

IV. Study the strengthening contribution of various microstructural components in the F, T5, and T6 conditions.

3. Laser-based additive manufacturing processability and mechanical properties of Al-Cu 224 alloys with TiB grain refiner additions

I. Study the effect of TiB grain refiner modification in as-cast conditions.

II. Use a surface laser remelting process to investigate the hot tearing susceptibility with different chemical compositions and TiB grain refiner additions.

III. Study the relationship between microstructure modification and hot tearing susceptibility.

IV. Study the effect of T6 heat treatment on mechanical properties and precipitation microstructure.

1.4 Originality statement

This project focuses on the high-strength aluminum alloy development for the SLM process in comparison to conventional high-Si aluminum alloys. The strategy involves optimizing heat treatment parameters, modifying the chemical composition through Mn microalloying, and incorporating TiB grain refiners.

The first part focuses on the microstructure evolution of Selective laser-melted AlSi10MgMn alloy during heat treatments and their impact on mechanical properties. This alloy was produced using SLM for the first time. The study provides a comprehensive analysis of the effects of various heat treatment conditions on the alloy's microstructure. Furthermore, the yield strength (YS) was modeled using constitutive equations to reveal promising strengthening mechanisms under different heat treatment conditions. This model offers valuable insights into the strengthening mechanisms under various heat treatment conditions, addressing a gap currently unfilled in the existing literature.

In the second part, the effect of Mn modification on the mechanical properties of AlSi10Mg alloy was examined. Results demonstrated that Mn additions significantly improve the mechanical properties of AlSi10Mg. The influence of Mn was analyzed under different heat treatment conditions, including T5 and T6. The findings revealed how Mn modification accelerates Si precipitation and the formation of Mn-dispersoids, resulting in substantial enhancements in mechanical performance, which has not been reported in the literature. Additionally, atom probe tomography was employed to study various microstructural components in detail under the T5 condition, providing insights into how Mn can improve mechanical properties in AlSi10Mg.

The third part targeted the Al-Cu 224 alloys. For the first time, the behavior of this alloy during the SLM process was simulated using a laser surface remelting process. The investigation focused on the impact of TiB grain refiner additions to illustrate how microstructural evolution enhances the alloy's hot tearing resistance during production SLM. Higher levels of TiB grain refiner produced fine equiaxed grains, significantly reducing hot tearing susceptibility. The aging response of the modified 224 alloy to conventional T6 heat treatment was also studied, revealing superior mechanical properties compared to the commonly used AlSi10Mg alloy after SLM.

1.5 Thesis outline

The current PhD thesis comprises five chapters:

The first chapter provides a brief introduction to the current project, beginning with an overview of additive manufacturing and SLM. It then discusses the SLM of aluminum alloys, common defects associated with the process, and potential solutions to address these issues. The chapter concludes with the definition of the problem statement, research objectives, and the originality of this study.

In Chapter 2, the published paper "Evolution of Mechanical Properties and Microstructure of Selective Laser Melted AlSi10MgMn Alloy with Different Post Heat Treatments" in *Material Science and Engineering A* is presented. This chapter is based on the findings of the first stage of this project, showing the effect of heat treatment on the microstructure and mechanical properties of AlSi10MgMn alloy. In addition, the microstructure contributions toward the YS at each heat treatment condition were analyzed with the aid of constitutive strengthening equations and compared with experimentally measured values.

Chapter 3 presents the manuscript titled "Effect of Mn on Microstructural Characteristics and Mechanical Behavior of AlSi10Mg Alloys Produced by Selective Laser Melting." This manuscript is based on the second part of my Ph.D. project and is under internal review for publication in a scientific journal. The study investigates the microstructure and precipitation behavior of the alloy under different conditions including, as-manufactured, T5, and T6 heat treatments, using scanning electron microscopy (SEM), transmission electron microscopy (TEM), and atom probe tomography (APT). The improved

mechanical properties of the AlSi10Mg alloy after Mn modification are attributed to these microstructural changes.

In Chapter 4, the published paper "Laser-based additive manufacturing processability and mechanical properties of Al-Cu 224 alloys with TiB grain refiner additions" in the journal of *Materials* is presented. This chapter examines the behavior of the 224 alloy during the SLM process, simulated through a laser surface remelting technique. The study focuses on the microstructural evolution as the TiB grain refiner content increases, demonstrating its potential to enhance the processability of this alloy during SLM. Additionally, the impact of conventional T6 heat treatment on the mechanical properties of the 224 alloy is compared to those of the AlSi10Mg alloy. This chapter focuses on developing alloys with good hot tearing resistance that can be adopted in the SLM process.

Finally, Chapter 5 presents the conclusions of this research, summarizing the key findings and their implications for developing high-strength aluminum alloys for the SLM process. It also includes recommendations for future work, highlighting potential areas for further optimization and exploration.

References

[1] W. Zhang, J. Xu, Advanced lightweight materials for Automobiles: A review, Materials & Design 221 (2022) 110994.https://doi.org/10.1016/j.matdes.2022.110994

[2] S. Siengchin, A review on lightweight materials for defence applications: Present and future developments, Defence Technology 24 (2023) 1-17.https://doi.org/10.1016/j.dt.2023.02.025

[3] S.B. Nagaraju, H.C. Priya, Y.G.T. Girijappa, M. Puttegowda, 9 - Lightweight and sustainable materials for aerospace applications, in: S.M. Rangappa, S.M. Doddamani, S. Siengchin, M. Doddamani (Eds.), Lightweight and Sustainable Composite Materials, Woodhead Publishing2023, pp. 157-178.https://doi.org/10.1016/B978-0-323-95189-0.00007-X

[4] A.I. Taub, A.A. Luo, Advanced lightweight materials and manufacturing processes for automotive applications, MRS Bulletin 40(12) (2015) 1045-1054.https://doi.org/10.1557/mrs.2015.268

[5] X. You, Z. Xing, S. Jiang, Y. Zhu, Y. Lin, H. Qiu, R. Nie, J. Yang, D. Hui, W. Chen, Y. Chen, A review of research on aluminum alloy materials in structural engineering, Developments in the Built Environment 17 (2024) 100319.https://doi.org/10.1016/j.dibe.2023.100319

[6] S.S. Li, X. Yue, Q.Y. Li, H.L. Peng, B.X. Dong, T.S. Liu, H.Y. Yang, J. Fan, S.L. Shu, F. Qiu, Q.C. Jiang, Development and applications of aluminum alloys for aerospace industry, Journal of Materials Research and Technology 27 (2023) 944-983.https://doi.org/10.1016/j.jmrt.2023.09.274

[7] M. Manikkoth, S. Kunhi Kannan, J. Mary Gladis, T.P.D. Rajan, Aluminium alloys and composites for electrochemical energy systems, Progress in Materials Science 146 (2024) 101322.https://doi.org/10.1016/j.pmatsci.2024.101322

[8] H. Hegab, N. Khanna, N. Monib, A. Salem, Design for sustainable additive manufacturing: A review, Sustainable Materials and Technologies 35 (2023) e00576.https://doi.org/10.1016/j.susmat.2023.e00576

[9] C. Gao, S. Wolff, S. Wang, Eco-friendly additive manufacturing of metals: Energy efficiency and life cycle analysis, Journal of Manufacturing Systems 60 (2021) 459-472.https://doi.org/10.1016/j.jmsy.2021.06.011

[10] K. Wang, Y. Song, H. Sheng, J. Xu, S. Zhang, J. Qin, Energy efficiency design for eco-friendly additive manufacturing based on multimodal attention fusion, Journal of Manufacturing Processes 79 (2022) 720-730.https://doi.org/10.1016/j.jmapro.2022.05.010

[11] J. Jiang, Y. Ma, Path Planning Strategies to Optimize Accuracy, Quality, Build Time and Material Use in Additive Manufacturing: A Review, Micromachines 11(7) (2020) 633.https://doi.org/10.3390/mi11070633

[12] K. Wang, J. Xu, S. Zhang, J. Tan, Antivibration and energy efficiency design for large stroke additive manufacturing based on dynamic trajectory adaption, The International Journal of Advanced Manufacturing Technology 118(9) (2022) 3015-3034.https://doi.org/10.1007/s00170-021-08072-5

[13] H. Fan, J. Hu, Y. Wang, H. Zhang, W. Guo, J. Li, S. Xu, H. Li, P. Liu, A review of laser additive manufacturing (LAM) aluminum alloys: Methods, microstructures and mechanical properties, Optics & Laser Technology 175 (2024) 110722.https://doi.org/10.1016/j.optlastec.2024.110722

[14] H. Yang, J. Sha, D. Zhao, F. He, Z. Ma, C. He, C. Shi, N. Zhao, Defects control of aluminum alloys and their composites fabricated via laser powder bed fusion: A review, Journal of Materials Processing Technology 319 (2023) 118064.https://doi.org/10.1016/j.jmatprotec.2023.118064

[15] Z. Zhu, Z. Hu, H.L. Seet, T. Liu, W. Liao, U. Ramamurty, S.M. Ling Nai, Recent progress on the additive manufacturing of aluminum alloys and aluminum matrix composites: Microstructure, properties, and applications, International Journal of Machine Tools and Manufacture 190 (2023) 104047.https://doi.org/10.1016/j.ijmachtools.2023.104047

[16] N.T. Aboulkhair, M. Simonelli, L. Parry, I. Ashcroft, C. Tuck, R. Hague, 3D printing of Aluminium alloys: Additive Manufacturing of Aluminium alloys using selective laser melting, Progress in Materials Science 106 (2019).https://doi.org/10.1016/j.pmatsci.2019.100578

[17] H.-S. Yoon, J.-Y. Lee, H.-S. Kim, M.-S. Kim, E.-S. Kim, Y.-J. Shin, W.-S. Chu, S.-H. Ahn, A comparison of energy consumption in bulk forming, subtractive, and additive processes: Review and case study, International Journal of Precision Engineering and Manufacturing-Green Technology 1(3) (2014) 261-279.https://doi.org/10.1007/s40684-014-0033-0

[18] E.O. Olakanmi, R.F. Cochrane, K.W. Dalgarno, A review on selective laser sintering/melting (SLS/SLM) of aluminium alloy powders: Processing, microstructure, and properties, Progress in Materials Science 74 (2015) 401-477.https://doi.org/10.1016/j.pmatsci.2015.03.002

[19] M. Wang, H. Yan, P. Zhang, Q. Lu, H. Shi, B. Zhang, Particulate-reinforced Al-based metal matrix composites fabricated by selective laser melting: A comprehension review, Optics & Laser Technology 176 (2024) 110918.https://doi.org/10.1016/j.optlastec.2024.110918

[20] R. Nandhakumar, K. Venkatesan, A process parameters review on selective laser melting-based additive manufacturing of single and multi-material: Microstructure, physical properties, tribological, and surface roughness, Materials Today Communications 35 (2023) 105538.https://doi.org/10.1016/j.mtcomm.2023.105538

[21] X. Wang, M. Jiang, Z. Zhou, J. Gou, D. Hui, 3D printing of polymer matrix composites: A review and prospective, Composites Part B: Engineering 110 (2017) 442-458.https://doi.org/10.1016/j.compositesb.2016.11.034

[22] N.T. Aboulkhair, N.M. Everitt, I. Ashcroft, C. Tuck, Reducing porosity in AlSi10Mg parts processed by selective laser melting, Additive Manufacturing 1-4 (2014) 77-86.https://doi.org/10.1016/j.addma.2014.08.001

[23] J. Zhang, B. Song, Q. Wei, D. Bourell, Y. Shi, A review of selective laser melting of aluminum alloys: Processing, microstructure, property and developing trends, Journal of Materials Science & Technology 35(2) (2019) 270-284.https://doi.org/10.1016/j.jmst.2018.09.004

[24] R. Khajeh, M. Javidani, M. Mofarrehi, X.G. Chen, M. Ahmed, A. Farzaneh, A. Heidarzadeh, Enhancing microstructure and mechanical properties of laser powder bed fusion-fabricated AlSi10Mg alloy through tailored friction stir processing and post-heat treatment, Materials Science and Engineering: A 889 (2024) 145855.https://doi.org/10.1016/j.msea.2023.145855

[25] K.G. Prashanth, S. Scudino, H.J. Klauss, K.B. Surreddi, L. Löber, Z. Wang, A.K. Chaubey, U. Kühn, J. Eckert, Microstructure and mechanical properties of Al–12Si produced by selective laser melting: Effect of heat treatment, Materials Science and Engineering: A 590 (2014) 153-160.https://doi.org/10.1016/j.msea.2013.10.023

[26] N.T. Aboulkhair, I. Maskery, C. Tuck, I. Ashcroft, N.M. Everitt, The microstructure and mechanical properties of selectively laser melted AlSi10Mg: The effect of a conventional T6-like heat treatment, Materials Science and Engineering: A 667 (2016) 139-146.https://doi.org/10.1016/j.msea.2016.04.092

[27] P. Rometsch, Q. Jia, K. V. Yang, X. Wu, 14 - Aluminum alloys for selective laser melting – towards improved performance, in: F. Froes, R. Boyer (Eds.), Additive Manufacturing for the Aerospace Industry, Elsevier2019, pp. 301-325.https://doi.org/10.1016/B978-0-12-814062-8.00016-9

[28] P.A. Rometsch, Y. Zhu, X. Wu, A. Huang, Review of high-strength aluminium alloys for additive manufacturing by laser powder bed fusion, Materials & Design 219 (2022) 110779.https://doi.org/10.1016/j.matdes.2022.110779

[29] G. Del Guercio, D.G. McCartney, N.T. Aboulkhair, S. Robertson, R. Maclachlan, C. Tuck, M. Simonelli, Cracking behaviour of high-strength AA2024 aluminium alloy produced by Laser Powder Bed Fusion, Additive Manufacturing 54 (2022) 102776.https://doi.org/10.1016/j.addma.2022.102776

[30] J.H. Martin, B.D. Yahata, J.M. Hundley, J.A. Mayer, T.A. Schaedler, T.M. Pollock, 3D printing of high-strength aluminium alloys, Nature 549(7672) (2017) 365-369.https://doi.org/10.1038/nature23894

[31] H. Zhang, H. Zhu, T. Qi, Z. Hu, X. Zeng, Selective laser melting of high strength Al–Cu–Mg alloys: Processing, microstructure and mechanical properties, Materials Science and Engineering: A 656 (2016) 47-54.https://doi.org/10.1016/j.msea.2015.12.101

[32] A. Mehta, L. Zhou, T. Huynh, S. Park, H. Hyer, S. Song, Y. Bai, D.D. Imholte, N.E. Woolstenhulme, D.M. Wachs, Y. Sohn, Additive manufacturing and mechanical properties of the dense and crack free Zr-modified aluminum alloy 6061 fabricated by the laser-powder

bed fusion, Additive Manufacturing 41 (2021) 101966.https://doi.org/10.1016/j.addma.2021.101966

[33] N. Kaufmann, M. Imran, T.M. Wischeropp, C. Emmelmann, S. Siddique, F. Walther, Influence of Process Parameters on the Quality of Aluminium Alloy EN AW 7075 Using Selective Laser Melting (SLM), Physics Procedia 83 (2016) 918-926.https://doi.org/10.1016/j.phpro.2016.08.096

[34] C. Galy, E. Le Guen, E. Lacoste, C. Arvieu, Main defects observed in aluminum alloy parts produced by SLM: From causes to consequences, Additive Manufacturing 22 (2018) 165-175.https://doi.org/10.1016/j.addma.2018.05.005

[35] J. Zhang, W. Yuan, B. Song, S. Yin, X. Wang, Q. Wei, Y. Shi, Towards understanding metallurgical defect formation of selective laser melted wrought aluminum alloys, Advanced Powder Materials 1(4) (2022) 100035.https://doi.org/10.1016/j.apmate.2022.100035

[36] D. Buchbinder, H. Schleifenbaum, S. Heidrich, W. Meiners, J. Bültmann, High Power Selective Laser Melting (HP SLM) of Aluminum Parts, Physics Procedia 12 (2011) 271-278.https://doi.org/10.1016/j.phpro.2011.03.035

[37] C. Weingarten, D. Buchbinder, N. Pirch, W. Meiners, K. Wissenbach, R. Poprawe, Formation and reduction of hydrogen porosity during selective laser melting of AlSi10Mg, Journal of Materials Processing Technology 221 (2015) 112-120.https://doi.org/10.1016/j.jmatprotec.2015.02.013

[38] K.V. Yang, P. Rometsch, T. Jarvis, J. Rao, S. Cao, C. Davies, X. Wu, Porosity formation mechanisms and fatigue response in Al-Si-Mg alloys made by selective laser melting, Materials Science and Engineering: A 712 (2018) 166-174.https://doi.org/10.1016/j.msea.2017.11.078

[39] W. Li, F. Qian, J. Li, Y. Zhu, Y. Liang, S. Xu, Y. Li, X. Cheng, Design strategy for eliminating cracking and improving mechanical properties of Al-Mg-Si alloys fabricated by laser melting deposition, Additive Manufacturing 68 (2023) 103513.https://doi.org/10.1016/j.addma.2023.103513

[40] Z. Wang, L. Zhuo, E. Yin, Z. Zhao, Microstructure evolution and properties of nanoparticulate SiC modified AlSi10Mg alloys, Materials Science and Engineering: A 808 (2021).https://doi.org/10.1016/j.msea.2021.140864

[41] D. Gu, H. Wang, D. Dai, Laser Additive Manufacturing of Novel Aluminum Based Nanocomposite Parts: Tailored Forming of Multiple Materials, Journal of Manufacturing Science and Engineering 138(2) (2015).https://doi.org/10.1115/1.4030376

[42] A. Martin, M. San Sebastian, E. Gil, C.Y. Wang, S. Milenkovic, M.T. Pérez-Prado, C.M. Cepeda-Jiménez, Effect of the heat treatment on the microstructure and hardness evolution of a AlSi10MgCu alloy designed for laser powder bed fusion, Materials Science and Engineering: A 819 (2021).https://doi.org/10.1016/j.msea.2021.141487

[43] Y. Chen, L. Wang, Z. Feng, W. Zhang, Effects of heat treatment on microstructure and mechanical properties of SLMed Sc-modified AlSi10Mg alloy, Progress in Natural Science: Materials International 31(5) (2021) 714-721.https://doi.org/10.1016/j.pnsc.2021.08.003

[44] J. Fiocchi, C.A. Biffi, A. Tuissi, Selective laser melting of high-strength primary AlSi9Cu3 alloy: Processability, microstructure, and mechanical properties, Materials & Design 191 (2020) 108581.https://doi.org/10.1016/j.matdes.2020.108581

[45] B. Zhang, W. Wei, W. Shi, Y. Guo, S. Wen, X. Wu, K. Gao, L. Rong, H. Huang, Z. Nie, Effect of heat treatment on the microstructure and mechanical properties of Er-containing Al–7Si–0.6 Mg alloy by laser powder bed fusion, Journal of Materials Research and Technology 18 (2022) 3073-3084.https://doi.org/10.1016/j.jmrt.2022.04.023

[46] S.Y. Zhou, Y. Su, H. Wang, J. Enz, T. Ebel, M. Yan, Selective laser melting additive manufacturing of 7xxx series Al-Zn-Mg-Cu alloy: Cracking elimination by co-incorporation of Si and TiB2, Additive Manufacturing 36 (2020) 101458.https://doi.org/10.1016/j.addma.2020.101458

[47] S. Zhang, Z. Chen, P. Wei, K. Huang, Y. Zou, S. Yao, M. Li, B. Lu, J. Xing, Microstructure and properties of a nano-ZrO2-reinforced AlSi10Mg matrix composite prepared by selective laser melting, Materials Science and Engineering: A 838 (2022) 142792.https://doi.org/10.1016/j.msea.2022.142792

[48] L. Xi, P. Wang, K.G. Prashanth, H. Li, H.V. Prykhodko, S. Scudino, I. Kaban, Effect of TiB2 particles on microstructure and crystallographic texture of Al-12Si fabricated by selective laser melting, Journal of Alloys and Compounds 786 (2019) 551-556.https://doi.org/10.1016/j.jallcom.2019.01.327

[49] Z. Fan, C. Li, H. Yang, Z. Liu, Effects of TiC nanoparticle inoculation on the hot-tearing cracks and grain refinement of additively-manufactured AA2024 Al alloys, Journal of Materials Research and Technology 19 (2022) 194-207.https://doi.org/10.1016/j.jmrt.2022.05.039

[50] M.J. Benoit, M.A. Whitney, S.M. Zhu, D. Zhang, M.R. Field, M.A. Easton, The beneficial effect of minor iron additions on the crack susceptibility of rapidly solidified aluminum alloy 6060 toward additive manufacturing applications, Materials Characterization 205 (2023).https://doi.org/10.1016/j.matchar.2023.113287

[51] H. Zhang, H. Zhu, X. Nie, J. Yin, Z. Hu, X. Zeng, Effect of Zirconium addition on crack, microstructure and mechanical behavior of selective laser melted Al-Cu-Mg alloy, Scripta Materialia 134 (2017) 6-10.https://doi.org/10.1016/j.scriptamat.2017.02.036

Chapter 2

Evolution of Mechanical Properties and Microstructure of Selective Laser Melted AlSi10MgMn Alloy with Different Post Heat Treatments

(This article is published in: Materials Science and Engineering: A 915 (2024) 147249)

Abstract

This study investigated the effects of various post heat treatments on the mechanical properties and microstructure evolution of an AlSi10MgMn alloy containing 0.5 wt.% Mn produced by the selective laser melting process for the first time. The microstructure of the samples was analyzed using optical microscopy, scanning electron microscopy, electron backscatter diffraction, and transmission electron microscopy. In the as-manufactured (F) condition, the alloy exhibited an ultimate tensile strength (UTS) of 486 MPa, a yield strength (YS) of 299 MPa, and an elongation of 10.3%. After a T5 treatment, the UTS and YS increased to 532 MPa and 386 MPa, respectively, resulting in a remarkable 30% improvement in YS compared to the F state. The tensile properties achieved by the new alloy were considerably higher than those reported for conventional AlSi10Mg alloys in the F, T5, and T6 conditions. The T5 treatment promoted the precipitation of a large fraction of Si-rich nanoparticles and MgSi-based precipitates without disrupting the Si-rich network. After a T6 treatment, the Si-rich network completely disappeared, and the main

strengthening phase was MgSi-based precipitates accompanied by α-Al(Mn,Fe)Si dispersoids induced by the Mn addition. Using microstructure-based constitutive models, the strengthening contributions of various microstructural components to mechanical strength in different processing conditions were analyzed.

Keywords: AlSi10MgMn alloy, Selective laser melting, Post heat treatments, Mechanical properties, Microstructure, Strengthening mechanisms.

2.1 Introduction

Selective laser melting (SLM) is an emerging additive manufacturing process that offers the advantage of creating complex near-net-shape structures. This process provides rapid cooling rates (10^4-10^7 K/s), which are much faster than conventional casting (1-10^2 K/s), and hence significantly changes the solidified microstructure and the mechanical properties of final products. The SLM process is increasingly attractive in various industrial sectors due to its design flexibility and exceptional mechanical properties for advanced materials [1, 2]. However, the production of high-integrity aluminum SLM products is primarily limited to highly castable or weldable aluminum alloys due to the challenges associated with the characteristics of the aluminum alloy itself, including a high risk of cracking, as well as a high laser reflectivity and propensity for oxidation [3-5]. To date, the most commonly used aluminum alloys that can easily be processed by SLM are high-Si alloys, particularly AlSi10Mg, because of their good weldability and excellent castability resulting from the presence of a large portion of low-melting point Al-Si eutectic [6, 7].

Various research efforts have been devoted to this group of alloys to optimize the process parameters and post-SLM heat treatments for improving the mechanical properties [8, 9].

Owing to their distinct rapid solidification microstructure, the post-SLM heat treatments can be divided into three categories over a wide temperature range, which constitute low-temperature treatments of direct aging (T5), medium-temperature annealing for stress relieving, and high-temperature solution treatment followed by artificial aging (T6) [10, 11]. Michaela et al. [12] reported that the direct aging of AlSi10Mg after SLM at 160°C improved the yield strength (YS) due to the formation of hardening precipitates but with a significant reduction in elongation. Cauwenbergh et al. [11] observed that printed AlSi10Mg samples exhibited a YS of 250 MPa, which could be improved to nearly 300 MPa with direct aging. Fite et al. [13] reported that the hardness of AlSi10Mg alloy after SLM can increase from 130 HV to 147 HV with direct aging at 170 °C. When the post-SLM heat treatment temperature of AlSi10Mg alloys increased from 200°C to 520°C, the Si-rich network in the melt pools progressively changed, leading to a substantial reduction in stress concentrations in the microstructure [14]. It is reported that when the aging temperature reached 400°C, the cellular structure and Si-rich network were broken and the Si particles became coarse, which resulted in softening [15]. It was also observed that the Si-rich network of an AlSi12 alloy became coarse and fragmented during direct post-SLM isothermal annealing at 200-500°C, and that the YS decreased from 260 MPa in the as-SLM condition to 95 MPa with the coarsest microstructure, while the fracture strain increased from 3% to 15% [16]. On the other hand, the T6 treatment strongly promoted precipitation, resulting in the presence of GP zones, β", and Mg_2Si in the T6 condition [17].

Despite the optimization of heat treatments, the mechanical properties of conventional AlSi10Mg alloys remain relatively low (YS is typically below 250 MPa) compared to those of high-strength wrought aluminum alloys (such as 2xxx, 6xxx, and 7xxx series). Therefore, the development of new aluminum materials with high mechanical performance for additive manufacturing is of primary importance [5]. Most of the explorations to date can be classified into two different routes: 1) producing composite materials with reinforcements [18, 19], and 2) modifying the chemical composition with alloying of different elements [20-23]. Composite materials have been reported to have impressive mechanical properties. However, the laser energy input during SLM significantly affected the densification behavior of composite parts, and hence increased the process difficulty to produce defect-free SLM parts [18]. Modification of the chemical composition, however, has been widely utilized to enhance the mechanical properties of AlSi10Mg alloys. It is reported that the addition of Sc improved the tensile strength of the AlSi10Mg, which was mainly attributed to grain refinement and refining of eutectic Si [21]. Martin et al. [20] observed that the remarkable hardness improvement in an AlSi10MgCu alloy compared to its AlSi10Mg counterpart was attributed to a reduced cell size, high concentration of nanosized precipitates, and the presence of shearable Cu-based GP zones. According to Zhang's results [23], the incorporation of Er into the molten pool of AlSi10Mg led to the formation of Al_3Er precipitates, which impeded the epitaxial growth of columnar crystals, and thus refined the grains along the boundaries of the molten pool.

AlSi10Mg alloys with Mn additions were originally designed for high pressure die casting to prevent die soldering in die-castings by inhibiting the formation of the plate-like β-Al_5FeSi intermetallic [24]. Additionally, the presence of Mn could enhance the alloy

strength by promoting the formation of α-$Al_{15}(Fe,Mn)_3Si_2$ dispersoids during solution treatment [24-26]. Alloying with Sr was also considered for the purpose of modifying Al-Si eutectics with just a small amount of Sr (~0.01 wt%) [27, 28]. In light of these earlier works on high pressure die cast AlSi10Mg alloys, it is reasonable to expect that the addition of Mn could also improve the properties of SLM-processed parts. However, no published information about the effect of Mn on SLMed AlSi10Mg in terms of microstructure and mechanical properties can be found in the literature.

In the present work, an AlSi10MgMn alloy containing 0.5 wt.% Mn was evaluated in the SLM process for the first time. The effects of various post-SLM heat treatments on the microstructure and mechanical properties of the AlSi10MgMn alloy were systematically studied. Microstructure-based constitutive models were applied to better understand the strengthening mechanisms and the relationship between microstructure and mechanical strength of SLM-produced parts.

2.2 Experimental procedure

Horizontally-oriented tensile samples were printed using an SLM Solutions 125 unit equipped with a 400 W IPG fiber laser. This printing direction was chosen to enable a meaningful comparison with existing literature on most AlSi10Mg alloys produced using SLM in the same orientation. Gas-atomized powder with a particle size range of 15-35 μm was employed, and its morphology and size distribution are shown in Figure 2-1. The chemical composition of the powder for the new AlSi10MgMn alloy is listed in Table 2-1. The main difference of the alloy composition compared to a conventional AlSi10Mg alloy is the 0.5 wt.% Mn addition and the higher amount of Mg.

The SLM process parameters including the scan speed, laser power, powder layer thickness, etc., as well as the dimension of the printed tensile samples are illustrated in Figure 2-2. In our preliminary trial, the two main parameters – the scan speed and laser power – were varied to evaluate the printing quality. Based on the minimum porosity of the printed parts, the scan speed of 1650 mm/s and the laser power of 350 W with the corresponding energy density of 54.4 J/mm^3 were found to be the optimized process parameters. Therefore, such optimized parameters were adopted in all following SLM tests (Figure 2-2).

After SLM and following approximately two weeks of natural aging (shipping time), various post-heat treatments were applied to the as-manufactured samples, including direct aging (T5), a stress relief (SR), and several T6 treatments, as shown in Table 2-2. The optimal temperatures and times of the T5 treatments were determined by hardness measurements of the aging responses at 165°C and 180°C for various durations. Figure 2-3 depicts these aging curves, revealing the peak aging for both temperatures. At 165°C, the maximum hardness exceeded 150 HV at 8 hours, while at 180°C, the maximum hardness surpassed 150 HV in 30 mins. These two conditions, along with standard stress relieving and T6 conditions, were used for the tensile tests. The T6-1 and T6-3 treatments in Table 2 were modified from the standard T6 treatment (T6-2) to reduce possible risks associated with porosity and residual stresses, respectively. In all T6 heat treatments, after solution treatment and water quenching, the samples were held at ambient temperature for 24 h (natural aging) before the artificial aging to control any possible effect of the natural aging on the precipitation during artificial aging.

Table 2-1: Chemical composition of raw powder feedstock determined by ICP (wt.%).

AlSi10MgMn	Si	Mg	Mn	Fe	Ti	Sr	Al
	10.7	0.55	0.51	0.19	0.05	0.01	Bal.

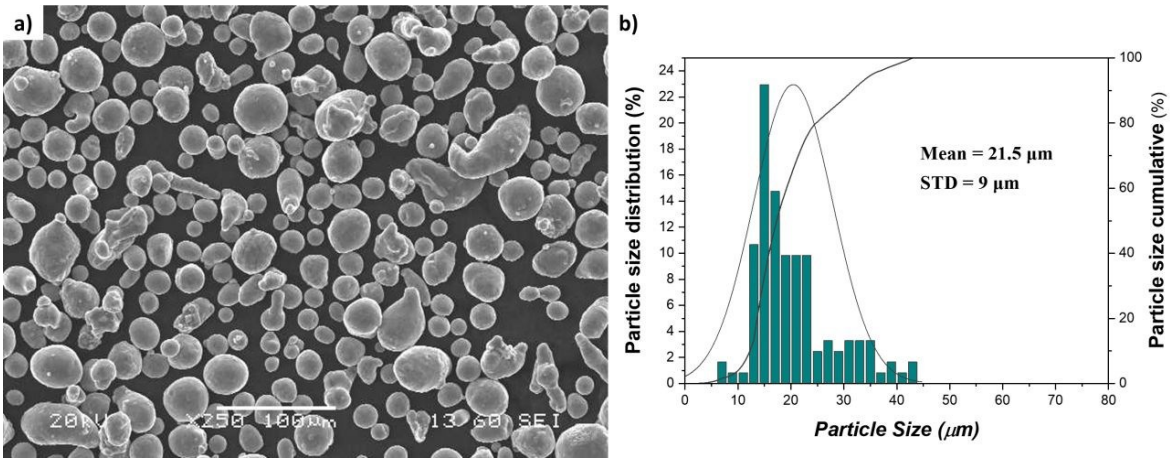

Figure 2-1: (a) SEM image showing the morphology of the AlSi10MgMn powder, (b) Particle size distribution of the AlSi10MgMn powder.

Scan speed (mm/s)	Laser power (W)	Powder layer thickness (µm)	Hatch distance (µm)	Laser spot size (µm)	Energy Density (J/mm³)	Adjacent layer rotation	Porosity (%)
2000	350	30	130	62	44.8	67°	0.21
1650	350	30	130	62	54.4	67°	0.13
1350	350	30	130	62	69.0	67°	0.41
700	370	30	130	62	135.5	67°	1.6

Optimized process parameter →

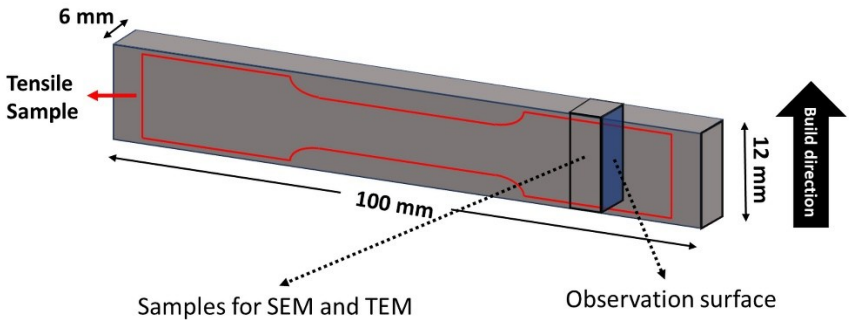

Figure 2-2: All SLM process parameters and the dimension of the printed tensile samples. The optimized process parameters adopted in SLM tests are indicated by the arrow.

Table 2-2: Heat treatment parameters

ID	Conditions	Parameters
F	As-manufactured	N/A
T5-1	Direct aging I	165 °C for 8 h
T5-2	Direct aging II	180 °C for 30 min
SR	Stress relief	300 °C for 2 h
T6-1	T6	500 °C for 0.5 h, water quench, natural aging for 24 h, aging at 165 °C for 6 h
T6-2	T6	530 °C for 0.5 h, water quench, natural aging for 24 h, aging at 165°C for 6 h
T6-3	SR + T6	SR + 530 °C for 0.5h, water quench, natural aging for 24 h, aging at 165 °C for 6 h

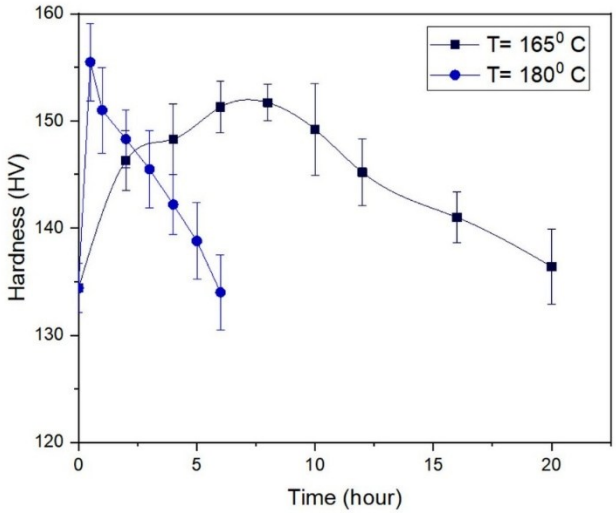

Figure 2-3**:** Effect of T5 direct aging on hardness as a function of aging time and temperature.

Mechanical properties were evaluated through microhardness and tensile tests. Vickers microhardness was measured with a load of 25 g and a dwell time of 20 s. At least ten indentations were made to obtain the average values. The subsized tensile samples were printed and machined perpendicular to the building direction (Figure 2-2). The tensile tests were conducted at room temperature using an Instron 8801 servo-hydraulic unit with a

strain rate of 3.3 x 10^{-4} s^{-1}, according to the ASTM-E8 standard. At least three tensile samples were tested for each condition to obtain the average value.

After SLM, phase identifications in the microstructure were determined by X-ray diffraction using a Bruker D8 Discover system with Cu Kα radiation (λ = 1.54 Å). The XRD data were collected in the 2θ range of 10–80°, with a step size of 0.02°. The microstructure was observed using an optical microscope (OM), a scanning electron microscope (SEM, JSM-6480LV) equipped with an electron backscatter diffraction unit (EBSD), and a transmission electron microscope (TEM, JEM-2100) equipped with energy dispersive X-ray spectrometers (EDS). The grain structures after SLM and the various heat treatments were characterized using EBSD. The average grain size was measured according to the ASTM-E112 and by using the intercept method. The precipitates formed during the heat treatments were observed by TEM on the building surface, highlighted in blue in Figure 2-2. The TEM samples were prepared with a precision ion polishing system (PIPS, Gatan). The thicknesses of the final TEM samples were measured using convergent-beam electron diffraction patterns [29] to quantify the precipitates. The size and volume fraction of all precipitates (Si nanoparticles, MgSi precipitates, and α-dispersoids) were quantified using the ImageJ analysis software on several recorded TEM images. The details of the quantification method can be found in [30, 31].

2.3 Results

2.3.1 Mechanical properties in various heat treatment conditions

Figure 2-4 shows the tensile properties for all the evaluated heat treatment conditions, which can be classified into four groups based on their similarity and corresponding

mechanical properties, namely the F, T5, SR, and T6 conditions. It is obvious that both T5-1 and T5-2 exhibited very similar tensile properties. Also, the mechanical properties of the T6-1, T6-2, and T6-3 treatments were in the same range. Typical engineering stress-strain curves of four selected conditions are shown in Figure 2-5. The SR and T6-3 samples exhibited a distinct necking point, whereas the F and T5-1 samples did not show a necking point.

Generally, owing to the high solidification rate and fine microstructure, the mechanical properties of SLM products are significantly higher than those obtained by conventional casting processes [2]. The F samples exhibited a UTS of 486 MPa, a YS of 299 MPa, and an elongation to fracture of 10.3%. After the direct aging (T5-1 and T5-2 samples), the YS increased to 386 and 361 MPa, respectively, while the elongation remained in a similar range. After the SR, the YS dropped remarkably to 211 MPa, and the elongation increased to 17.4%. In the T6 group, although the heat treatment conditions varied, the tensile properties of the T6-1, T6-2, and T6-3 samples were at a similar level. The T6 treatments can compensate for the lost tensile strength after stress relieving. For instance, the YS after the T6-3 treatment increased significantly to 321 MPa. However, the elongation decreased to 11.7%.

Most conventional AlSi10Mg alloys made by SLM have an average YS of around 250 MPa with an average elongation of 6% in the F condition [11, 12, 14, 32, 33], a 295 MPa YS with an elongation of 8% in the T5 condition [11], and a 239 MPa YS with an elongation of 9% in the T6 condition [34]. It is apparent that the tensile properties of the current AlSi10MgMn alloy are considerably higher than those reported for conventional AlSi10Mg alloys in the F, T5, and T6 conditions. Due to the distinct mechanical properties of

AlSi10MgMn, the following four conditions were selected for further study: F, T5-1, SR, and T6-3.

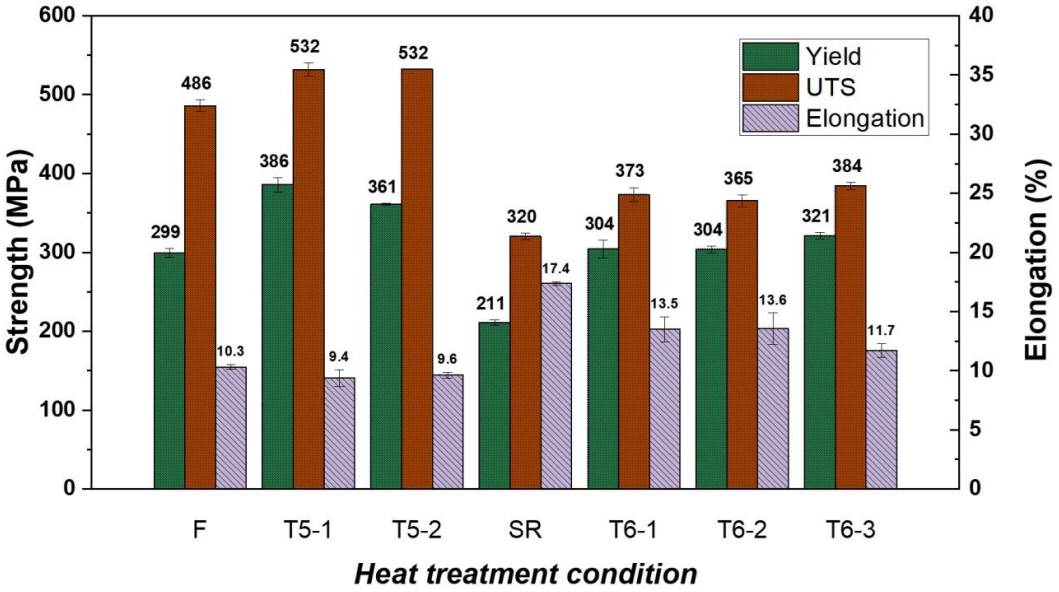

Figure 2-4: Tensile properties of F, T5-1, T5-2, SR, T6-1, T6-2, and T6-3 samples.

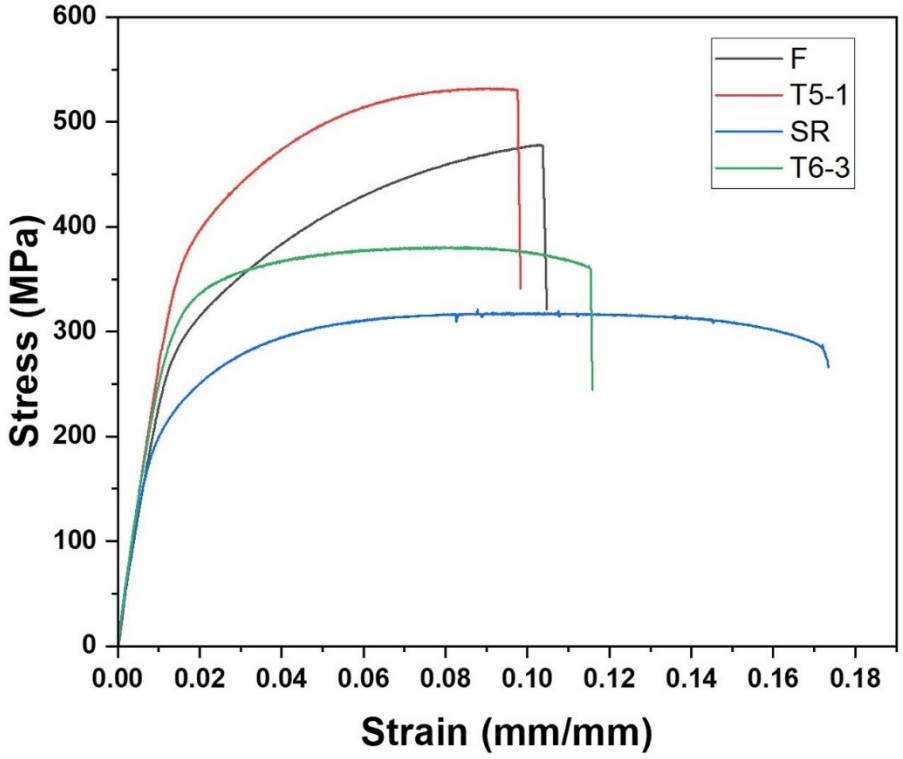

Figure 2-5: Typical engineering stress-strain curves for F, T5-1, SR, and T6-3 samples.

2.3.2 Microstructure after SLM

The macrostructure of the AlSi10MgMn samples in the F condition is shown in Figure 2-6. A fish-scale morphology of the overlapping melt pools can be seen from the side view (Figure 2-6a). The average melt pool width and depth were 132 ± 44 and 66 ± 16 μm, respectively. A top view of the track segments is shown in Figure 2-6b. The image clearly shows the 67° rotation between adjacent layers during SLM. The average width of the track segment was 130 ± 26 μm. In addition, some porosities were observed (red arrows). The final samples produced had a density greater than 99.8%.

Figure 2-7 illustrates three distinct microstructure regions in a melt pool in the F condition. Melt pool center (MPC) regions exhibited a fine cellular microstructure (Figure 2-7a) while melt pool boundaries (MPB) had a coarser microstructure (Figure 2-7a, b). By

contrast, heat-affected zones (HAZ) had a broken Si-rich network, in which Si began to spheroidize (Figure 2-7a, c). The MPC consisted of primary α-Al with a fine cellular morphology and a Si-rich network in the intercellular regions. On the other hand, the MPB consisted of coarser α-Al cells and Si-rich networks. The average α-Al cell sizes in the MPC and MPB regions were 0.49 ± 0.06 and 0.93 ± 0.04 μm, respectively. The reasons for such differences have been reported in recent literature [11, 35, 36]. Briefly, the MPC exhibited a higher thermal gradient and growth rate relative to the MPB. In every melt pool, new layers overlaid the solidified material. Although some of the previously solidified material might not have fully melted, it underwent a very short high-temperature heat treatment, resulting in the HAZ. The widths of the MPB and HAZ regions were 5.6 ± 0.5 and 3.5 ± 0.4 μm, respectively. The area fractions of MPC regions from the side and top surfaces were 89.9 ± 1.5 % and 88.2 ± 2.0 %, respectively. The area fraction of the Si-rich network was considered to be 12 %, which is close to the amount calculated for the AlSi10Mg alloy by thermodynamic equilibrium calculations [36, 37].

The optimized SLM process parameters used in this study align with the commonly used parameters for AlSi10Mg alloys [38]. This confirms that the new AlSi10MgMn alloy, with elevated levels of Mg and Mn, exhibited similar printability to conventional AlSi10Mg alloys. This is attributed to the high Si content of the new alloy, which is the main factor contributing to excellent printability. As mentioned in the introduction, AlSi10Mg alloys with Mn additions were originally designed for high pressure die casting to prevent die soldering in die castings, which could be a secondary alloy [24]. Although the current AlSi10MgMn alloy was not fabricated by the secondary alloy, the results suggest that secondary (recycled) AlSi10MgMn alloys with elevated levels of Fe, Mn and Mg could

achieve similar printability as standard primary AlSi10Mg alloys. The rapid solidification in the SLM process ensures that the extra Fe and Mn do not cause the usual concerns about large Fe/Mn-containing intermetallics that can decrease the ductility of castings. In fact, the SLM microstructure is so fine that such Fe/Mn-containing intermetallics rarely appear in the as-manufactured (F) condition.

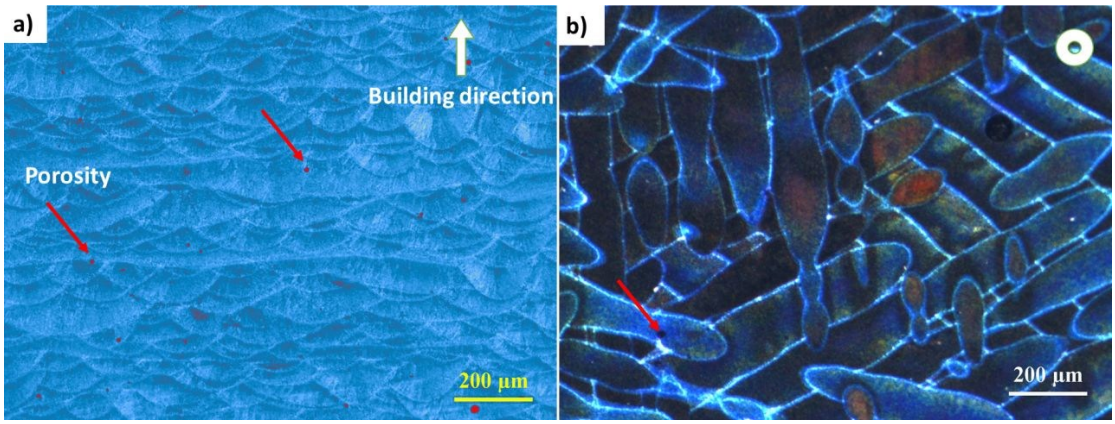

Figure 2-6: Macrostructure of the SLM AlSi10MgMn alloy, a) side view, b) top view, (OM images after etching with 0.5% HF solution).

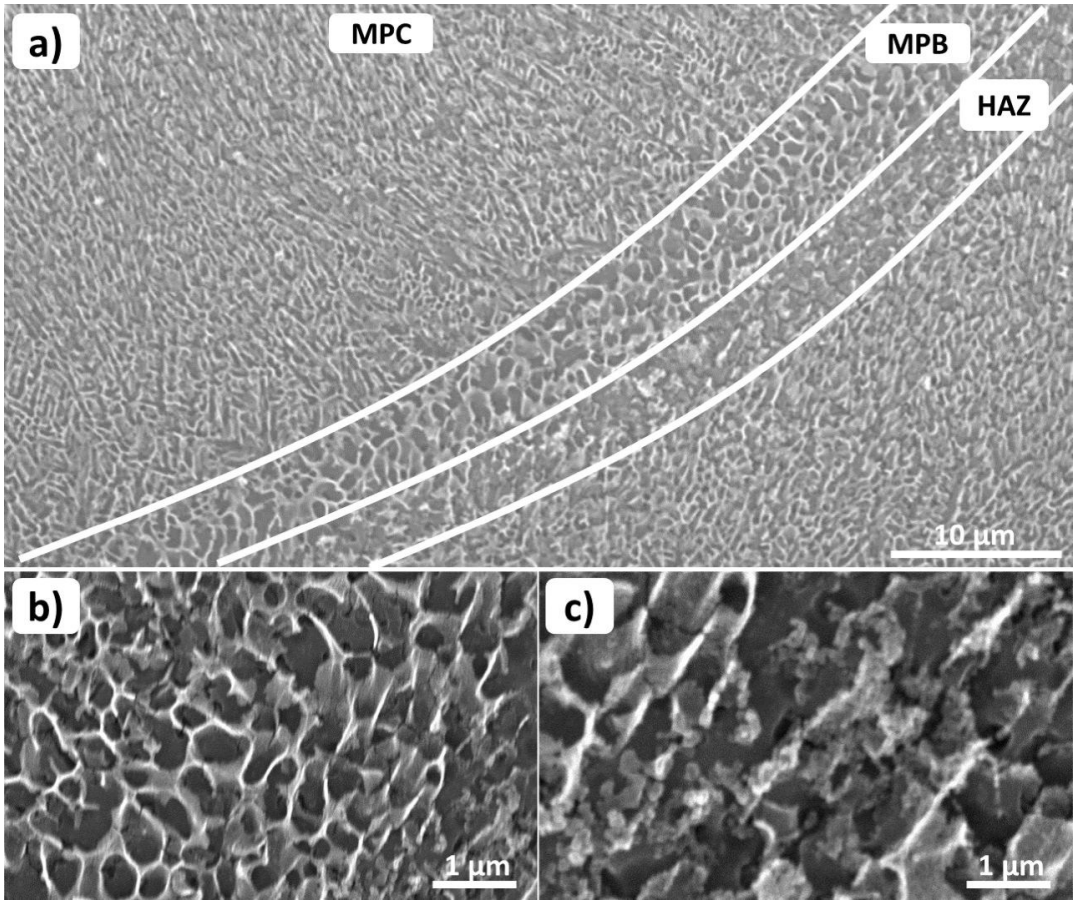

Figure 2-7: SEM images of SLMed AlSi10MgMn alloy in F condition showing a) melt pool center (MPC), melt pool boundary (MPB), and heat affected zone (HAZ) regions; b) higher magnification image of MPB region; and c) higher magnification image of HAZ region.

2.3.3 Grain structure and microstructure after heat treatment

The grain structures resulting from SLM are significantly different from those of conventional casting processes due to the unique characteristics of the SLM process [36, 39-41]. Figure 2-8a, b show EBSD orientation maps for the F and T6-3 samples. Both EBSD maps illustrate two distinct grain structures: 1) elongated columnar grains within melt pools aligned along the thermal gradient, and 2) fine equiaxed grains situated along the melt pool boundaries. The grain structure remained almost unchanged after the T6-3

treatment, and the overall average grain size of both the columnar and equiaxed grains was 10 μm for both the F and T6-3 conditions. The same behavior was observed for a solution heat-treated A357 alloy [42]. The corresponding geometrically necessary dislocation (GND) maps for the F and T6-3 samples are presented in Figure 2-8c, d. Notably, the dislocation number density fell within a similar range for both conditions with an average value of approximately 3×10^{13} m^{-2}. Similar grain structures are anticipated for the T5-1 and SR conditions due to their lower heat treatment temperatures compared to T6-3. In the F state of a conventional AlSi10Mg alloy made by SLM, the rapid cooling led to the concentration of dislocations at cell boundaries. In the T5 condition, these dislocations were dispersed throughout the matrix, while in the T6 condition, they were localized around larger Si particles [43]. It was also reported that the average dislocation density of the Al phase remained relatively constant in an SLMed AlSi10Mg alloy after T5, SR, and T6 heat treatments, as assessed through XRD patterns [44].

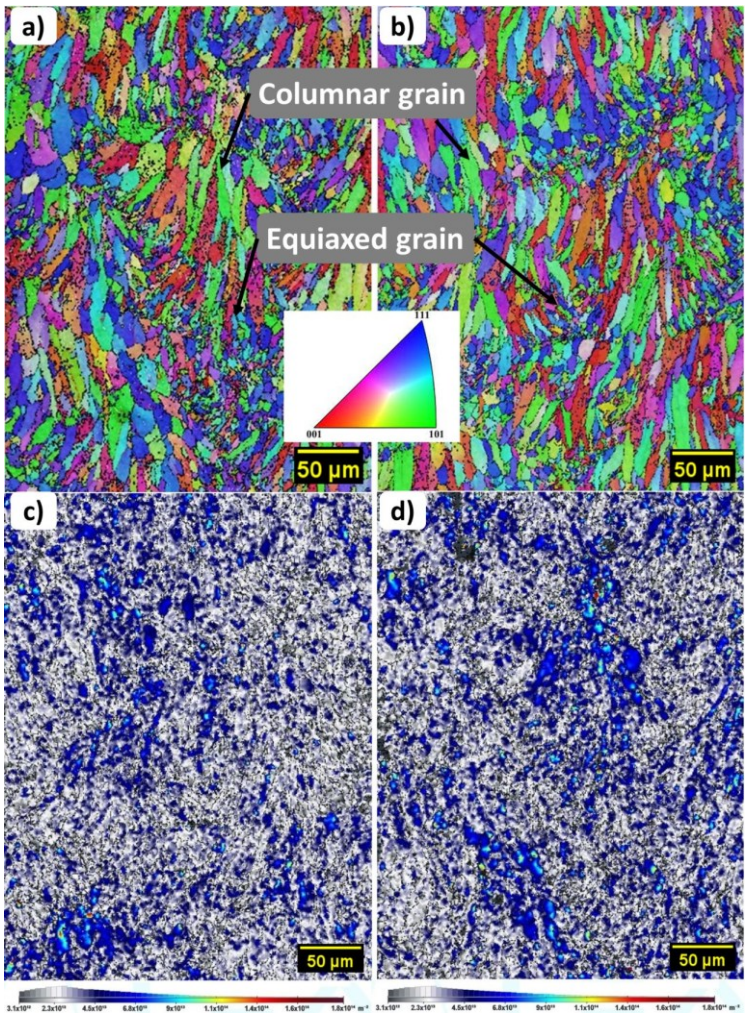

Figure 2-8: EBSD orientation maps for SLMed AlSi10MgMn in, a) F and b) T6-3 conditions; corresponding geometrically necessary dislocation (GND) maps in, c) F and d) T6-3 conditions.

Significant microstructural changes were observed after the different heat treatments. Figure 2-9 presents a comparison of the microstructure evolution for the F, T5-1, SR, and T6-3 conditions. The Si-rich network remained intact after the T5-1 treatment relative to the F condition, as shown in Figure 2-9a, b. By contrast, after the SR treatment, the Si-rich network began to break apart, followed by the spheroidization of Si particles (Figure 2-9c). The same behavior has been reported for conventional AlSi10Mg, resulting in a decrease in mechanical properties [45]. The fine Si-rich network in SLMed samples can serve as a

barrier to dislocation movement [46, 47], but the broken and disrupted Si-rich network in the SR condition can be expected to reduce the strengthening effectiveness of the Si-rich network. This is one of the main reasons why the tensile strength experienced a notable decrease compared to the F and T5-1 conditions. After the T6-3 treatment, the Si-rich network completely disappeared due to the high-temperature solution treatment at 530 °C, and the microstructure became more homogeneous without separate MPC, MPB, and HAZ regions. Two types of individual particles were observed in the microstructure (Figure 2-9d). Most particles were irregularly shaped Si particles with an average size of 0.9±0.3 μm (Figure 2-9d, e). The second type of particles were much finer with an average diameter of 97 nm. They contained Si, Mn, and Fe as measured by SEM-EDS analysis (Figure 2-9f). According to their chemical composition and information in the literature [24], those particles were identified as α-$Al_{15}(Mn,Fe)_3Si_2$ dispersoids, which could provide a supplementary strengthening effect.

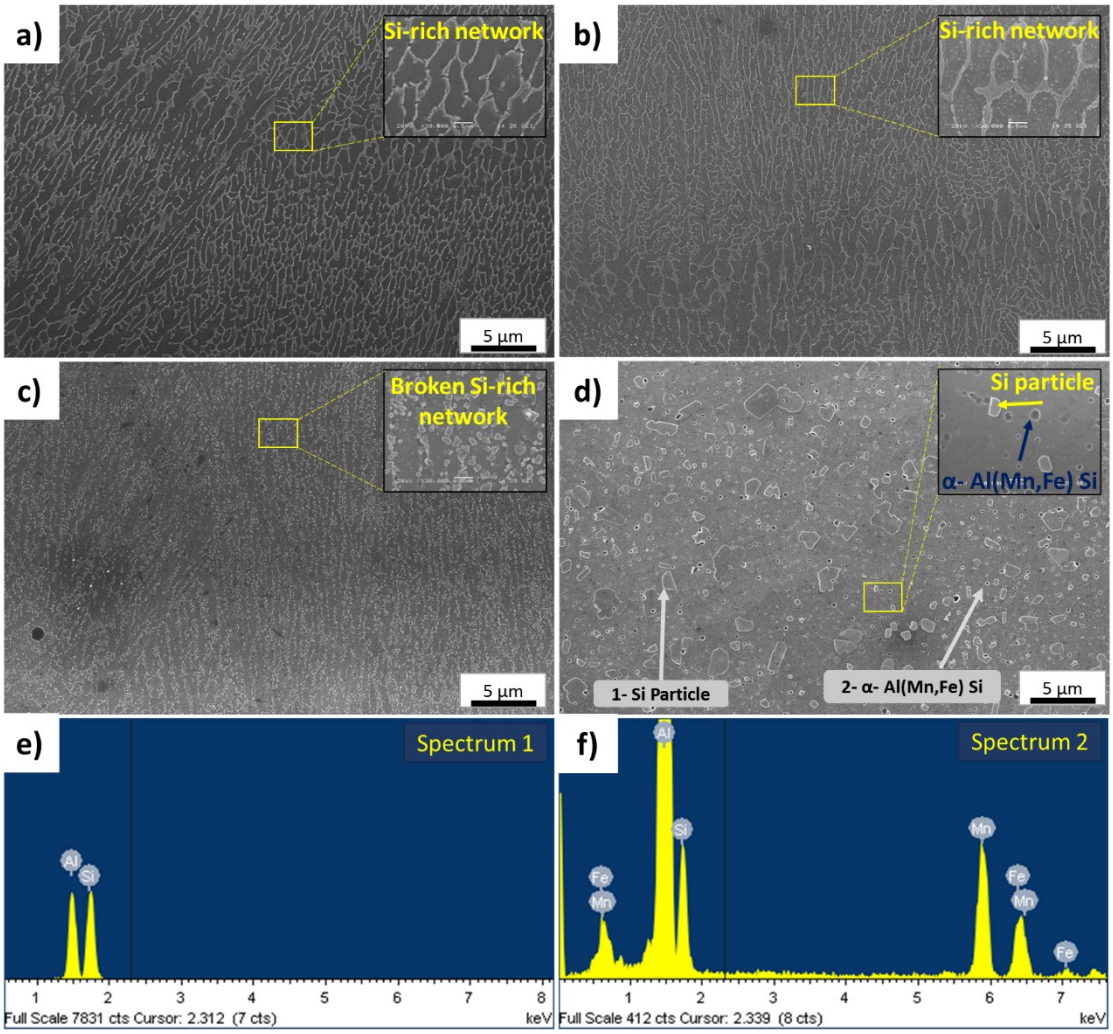

Figure 2-9: SEM images showing the microstructures of the SLMed AlSi10MgMn alloy in a) F, b) T5-1, c) SR, and d) T6-3 conditions; e) SEM-EDS spectrum 1 for a Si particle and (f) spectrum 2 for α-Al(Mn,Fe)Si dispersoid in d).

3.3.4 Phase identification by XRD

The XRD patterns of the F and the other three heat treatment conditions are shown in Figure 2-10a, and the enlarged Al peaks (111) of all conditions are depicted in Figure 2-10b. The Al and Si phases were the major phases observed in the F condition. The Si peaks in the F condition were relatively wide and low in intensity, indicating that the crystal size was smaller and the amount of Si was lower compared to the other conditions [42], which

corresponds to the higher expected degree of supersaturated Si in the Al matrix [48]. Furthermore, the Al peak (111) is expected to appear at 38.44°, but the peak in the F condition was shifted toward a higher angle as shown by the dotted line in Fig. 10b. This discrepancy indicates that the supersaturated Si atoms in the Al matrix altered the Al lattice parameter.

After heat treatment, Figure 2-10a reveals a gradual increase in Si peak intensity as the heat treatment temperature increased, which signifies an increase of Si particles in the Al matrix. On the other hand, Figure 2-10b shows that the Al peak (111) moves to lower angle positions after the heat treatments, indicating a reduction of Si in supersaturated solid solution. Another notable distinction following the T6-3 treatment is the presence of equilibrium Mg_2Si and α-Al(Mn,Fe)Si phases. Mg_2Si is identified at an angle (2θ) of approximately 40°, which was also reported in previous work for conventional AlSi10Mg alloy [49, 50].

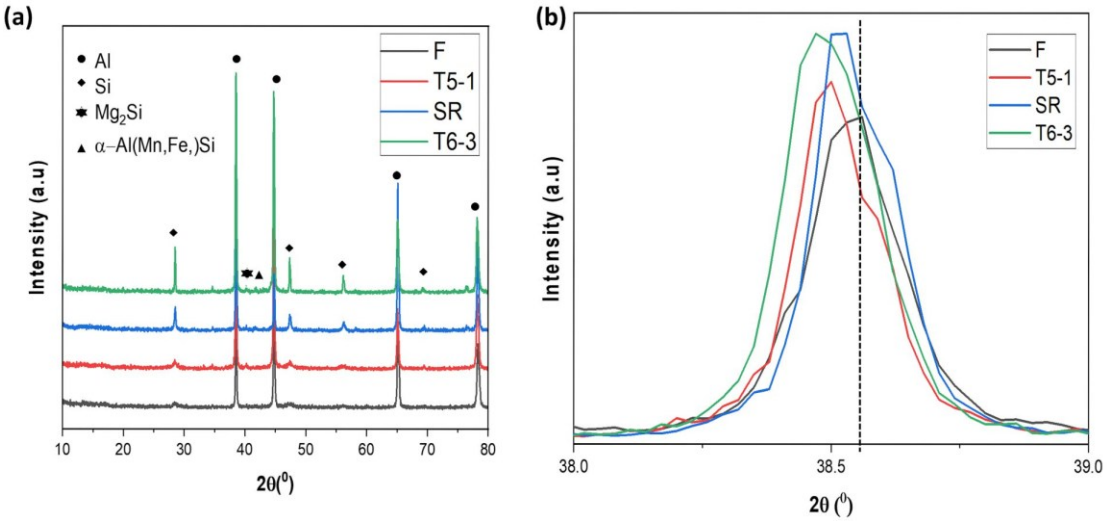

Figure 2-10: a) XRD patterns and b) enlarged Al peaks (111) of four tested conditions.

3.3.5 Evolution of precipitation with heat treatment

Figure 2-11 presents the typical precipitation microstructures for the F and T5-1 conditions. Figure 2-11a shows the precipitates between the Si-rich network in the F condition. In the enlarged image (Figure 2-11b), a number of nanosized particles could be clearly observed in the Al cells. These precipitates had an average size of 4.76 nm and a volume fraction of 0.14%. The results of the TEM-EDS analysis show that the particles contained only Si (Figure 2-11c). Those Si-rich nanoparticles are confirmed by the selected area diffraction ring pattern (Figure 2-11d). The presence of nanosized Si-rich particles has been recently confirmed in AlSi10Mg alloys, and their formation is related to the thermal history [13, 51-53]. Additionally, the chemical composition of the Al matrix was determined with at least five measurements at cell center locations devoid of precipitated particles. In the F condition, the amount of Si in the solid solution was approximately 2.8 wt.%, which is higher than the maximum Si solubility in the Al matrix at the eutectic temperature (1.65 wt.%). This is because of the rapid solidification during SLM. The average concentrations of other alloying elements in the matrix were 0.11 wt.% for Mg and 0.13 wt.% for Mn, which provided a good solid solution strengthening in this condition. In some locations of the Si-rich network, the TEM and TEM-EDS also detected some particles containing a high amount of Mn and Fe. This suggests that α-Al(Mn, Fe)Si intermetallic particles formed within the Si-rich network, which could provide a complementary strengthening contribution to the Si-rich network.

In the direct aging T5-1 condition, two groups of precipitates were observed in the Al cells (Figure 2-11e). The first group is the granular particles, which contained only Si (Figure 2-11f), and had an average diameter of 15.8 nm and a volume fraction of 0.4%.

Figure 2-11g shows the corresponding selected-area diffraction ring pattern, which suggests these precipitates are randomly oriented Si-rich nanoparticles. These precipitates were previously reported in the literature in the T5 condition [54, 55]. Compared to the F condition, the Si-rich nanoparticles have grown in size and their volume fraction has increased in the T5-1 condition. The second group of precipitates is needle-like particles, which were identified as MgSi-based precipitates according to TEM-EDS results (Figure 2-11h), their morphology, and their size [56, 57]. The average length of those precipitates was 78.38 nm with a volume fraction of 1%. The amount of Si in the Al matrix decreased to 1.5 wt.% relative to the F condition due to the precipitation of Si-rich and MgSi nanoparticles. While the presence of α-Al(Mn, Fe)Si intermetallic particles inside the Si-rich network can provide a complementary strengthening, the precipitation of a large fraction of nanosized Si-rich and MgSi-based precipitates in the T5 condition plays a major role in its superior mechanical strength.

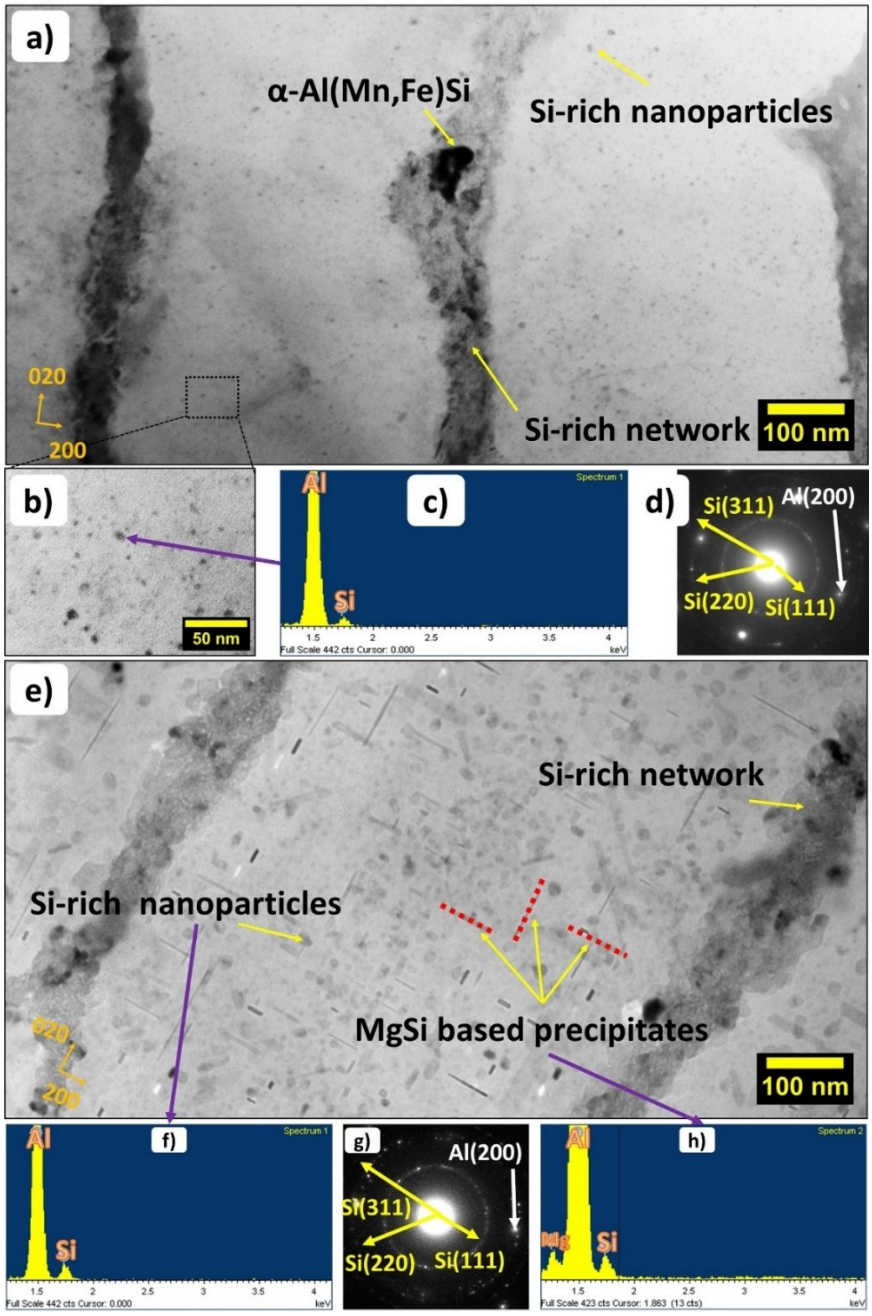

Figure 2-11: a) Bright-field TEM image of the precipitation microstructures of SLMed AlSi10MgMn in F condition, b) an enlarged image showing Si-rich nanoparticles, c) TEM-EDS of a Si-rich nanoparticle in b, d) selected area diffraction ring pattern from b; e) bright-field TEM image of precipitation microstructure of SLMed AlSi10MgMn in T5-1 condition, f) TEM-EDS of a Si-rich nanoparticle in e, g) selected area diffraction ring pattern of Si-rich nanoparticles in the middle of e, h) TEM-EDS of MgSi-based precipitates indicated in e.

The TEM result in Figure 2-12a reveals that the SR treatment has broken the continuous Si-rich network. Only one type of precipitate, granular Si-rich nanoparticles, was observed in the Al cells (see the inset of Figure 2-12a). The average size of these particles was 5.58 nm, and the volume fraction was 0.19%, which was slightly higher than in the F condition but much lower than in the T5-1 condition. The Si concentration in the Al matrix was approximately 1.7 wt.% according to TEM-EDS analysis. No metastable MgSi-based precipitates were observed in the SR condition. A few equilibrium β-Mg_2Si particles were occasionally observed, but these particles had a negligible strengthening effect.

After the T6-3 treatment, the Si-rich network was completely broken up (Figure 2-12b). In the Al matrix, a large number of needle-like precipitates were observed (see the enlarged image in the inset of Figure 2-12b). The average length of these precipitates was 45 nm and their volume fraction was 2%. These precipitates were MgSi-based precipitates based on the TEM-EDS results, their morphology, and their size [56, 57]. Due to Mn alloying, a number of large and spherical α-Al(Mn,Fe)Si dispersoids were also precipitated in the matrix. The average diameter of these dispersoids was 97 nm, and their volume fraction was 2.3%. It is evident that in the T6-3 condition, the MgSi-based precipitates provided the main strengthening contribution, while α-Al(Mn,Fe)Si dispersoids provided a supplementary strengthening effect, resulting in higher mechanical strength relative to conventional AlSi10Mg alloy (see further analysis in section 4.3). The quantitative results of all the precipitates in the four heat treatment conditions are summarized in Table 2-3 (Section 4.2).

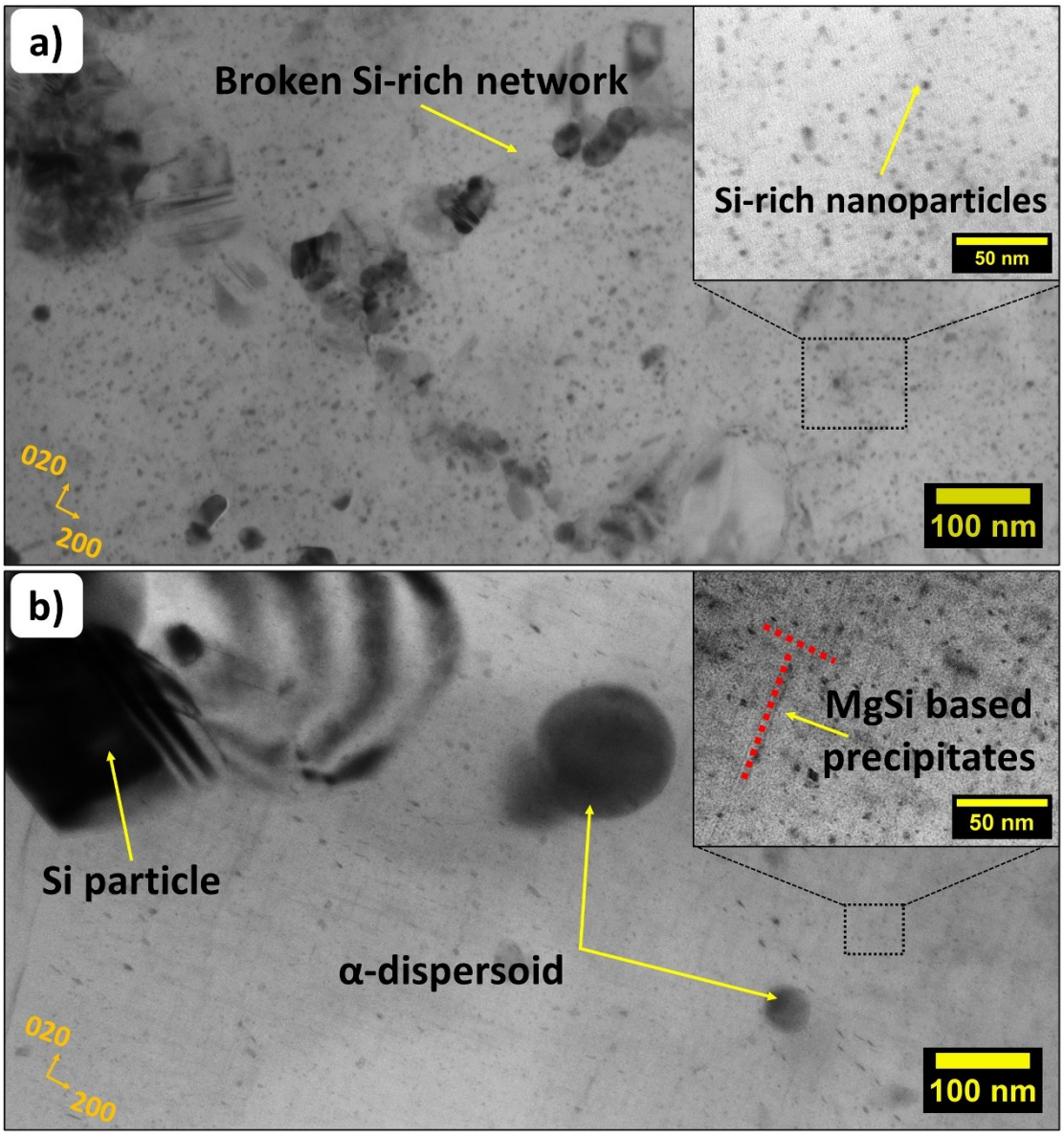

Figure 2-12: Bright-field TEM images of the precipitation microstructures of SLMed AlSi10MgMn in a) SR, and b) T6-3 conditions.

2.4 Discussion

2.4.1 Effect of heat treatment on strain hardening rate

The AlSi10MgMn alloy exhibits a remarkably high tensile strength following the SLM process, and its microstructure plays a crucial role in determining the superior mechanical

properties. After various post-SLM heat treatments, this alloy provided a wide range of combinations between strength and ductility. To understand the mechanisms involved, the strain hardening rate ($\Theta = \frac{d\sigma}{d\varepsilon}$) during the deformation can be regarded as an important characteristic of the alloy [41, 58, 59]. It is reported that significant strain hardening can result from the interaction between dislocations and the load-bearing Si network [51, 59]. Kim et al. [60] reported a much higher stress of the Si-rich network compared to that of the α-Al in SLMed AlSi10Mg, indicating the strong load-bearing effect of the Si-rich network and its significant contribution to macroscopic hardening.

Figure 2-13 depicts the strain hardening rate versus the true strain curves in the stable region of deformation for the F, T5-1, SR, and T6-3 conditions. The rate of strain hardening in the F and T5-1 samples was more than double that in the SR and T6-3 samples. In the F and T5-1 conditions, the saturation in strain hardening (the drop in the hardening value) happened at higher values of plastic strain, which indicates that the Si-rich network in both conditions effectively participated in strain hardening. A similar result has been reported previously [59]. By contrast, the low strain hardening rate of the SR and T6-3 heat treatments correlates with their improved ductility (Figure 2-5). In the SR condition, the Si-rich network underwent fragmentation (Figure 2-9), resulting in reduced effectiveness as a barrier for dislocation movement and a reduced load-bearing effect when compared to the F and T5-1 conditions. In the T6-3 condition, the Si-rich network was completely eliminated, and the Si phase remained in the matrix as individual particles. As a result, T6-3 samples exhibited the lowest strain hardening rate during plastic deformation in comparison to the other conditions, which is consistent with the literature for AlSi10Mg alloys [58, 59].

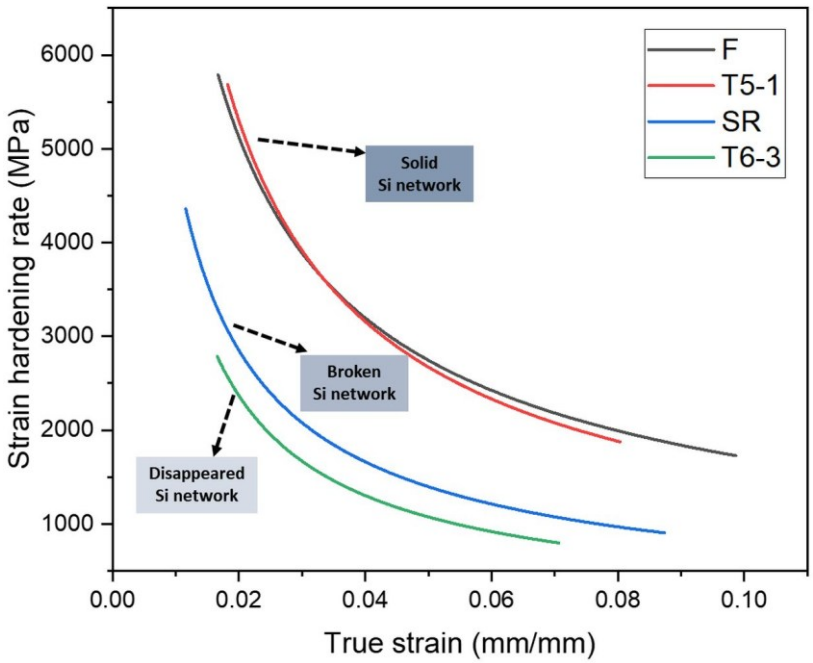

Figure 2-13: The strain hardening rate (θ) vs true strain (ε) curves for four different conditions.

2.4.2 Strengthening mechanisms

Figure 2-4 clearly shows that various tensile strengths could be achieved by different post heat treatments. The strengthening mechanisms in the SLMed AlSi10MgMn alloy are analyzed based on the microstructural characteristics using classical constitutive models to explain and predict the material YS [36, 51]. The YS is the result of a combined contribution from the interconnected eutectic Si network and the Al matrix. The Si network is treated like a reinforcement in a composite material. It is assumed that the overall theoretical YS (σ_y) of the alloy can be estimated by the linear summation of these two contributions (rule of mixture) using the following Eq. 1:

$$\sigma_y = f_{Si} * \sigma_{load} + f_m * \Delta\sigma_m \quad (1)$$

where f_{Si} and f_m are the volume fractions of the Si-rich network and the Al matrix, respectively. The summation of both fractions is equal to 1. The average volume fraction of the eutectic Si-rich network was considered to be 0.12 [36], and hence the remaining fraction is for the Al matrix. σ_{load} is the load-bearing capacity of the Si-rich network, which was calculated to be 380 MPa [7, 36]. $\Delta\sigma_m$ is considered as the mixed strengthening contributions from various microstructural components in the Al matrix, which can be expressed by Eq. 2.

$$\Delta\sigma_m = \sigma_0 + \Delta\sigma_d + \Delta\sigma_{ss} + \Delta\sigma_b + \Delta\sigma_p \quad (2)$$

where σ_0 is the friction stress for pure aluminum (10 MPa) [61]. $\Delta\sigma_d$, $\Delta\sigma_{ss}$, $\Delta\sigma_b$, and $\Delta\sigma_p$ are the YS increments from the dislocation forest, solid solution, grain boundaries, and precipitates, respectively.

$\Delta\sigma_d$ is the strengthening effect from the initial dislocation forest, which can be calculated by Eq. 3.

$$\Delta\sigma_d = 0.24MGb\sqrt{\rho_{dislocation}} \quad (3)$$

where M is the Taylor factor (=3.02), G is the shear modulus (=27.2 GPa), and b is the Burger's vector for dislocations (=0.286 nm). $\rho_{dislocation}$ is the dislocation density and is considered to be 10^{14} m^{-2} as an initial dislocation density in the Al matrix [36, 62]. The GND maps in Figure 2-8 indicated that there was only minimal variation among the different heat treatment conditions. Assuming a constant value of the dislocation density across all heat treatment conditions simplifies the calculation.

$\Delta\sigma_{ss}$ represents the strengthening effect from the solid solution mainly due to the presence of solutes [30, 63].

$$\Delta\sigma_{ss}=39.7\ (C_{Si})^{2/3}+ 39.7\ (C_{Mg})^{2/3}+18.35\ (C_{Mn})^{0.9} \quad (4)$$

where C_{Si}, C_{Mg}, and C_{Mn} are the weight percentages of Si, Mg, and Mn in solid solution. It should be noted that the concentrations and strengthening effects of Mg in the T5-1, SR, and T6-3 conditions were minimal and hence neglected during the calculation due to the precipitation of stable and meta-stable Mg_2Si. The concentration and strengthening effect of Mn in the T6-3 condition were neglected due to the precipitation of α-dispersoids.

$\Delta\sigma_b$ is the contribution of the boundary effect impeding dislocation motion, which is expressed by using the Hall-Petch equation. In the current study, the Si-rich network in the F and T5-1 conditions was considered as a reinforcing structure similar to a grain boundary [46, 47, 64].

$$\Delta\sigma_b= \frac{0.04}{\sqrt{d_b}} \quad (5)$$

where d_b denotes the cell size width (Figure 2-7) in the F and T5-1 conditions, and the average grain size for the SR and T6-3 conditions (Figure 2-8).

$\Delta\sigma_p$ represents the precipitation strengthening mechanism. There are two methods associated with this mechanism, depending on the size and type of the precipitates. Shearing is prevalent for small or weak particles, whereas the Orowan bypass mechanism dominates for large and hard particles [65].

For large Si particles, large MgSi-based precipitates and α-dispersoids, the Orowan bypass mechanism is applied using [36]:

$$\Delta\sigma_{Orowan} = \frac{MGb}{l} \quad (6)$$

$$l = \frac{d_{pre}}{2}\sqrt{\frac{2\pi}{3 f_v}} \quad (7)$$

where l is the precipitate spacing, d_{pre} is the diameter of equivalent spherical particles, and fv is the volume fraction of the precipitates or dispersoids.

For small Si-rich particles in the F and SR conditions as well as the shearable small MgSi-based precipitates, the shearing mechanism is applied to estimate the YS increment [66].

$$\Delta\sigma_{Shearing} = \frac{M}{b^2\sqrt{0.5G}}\sqrt{N_v \frac{d_{pre}}{2}}\, F^{3}/_{2} \quad (8)$$

$$N_v = \frac{6f_v}{\pi {d_{pre}}^3} \quad (9)$$

$$F = Gb^2\left(\frac{d_{pre}}{15}\right) \quad (10)$$

where N_v is the number density of the precipitates, and F is the mean interaction force between particles and dislocations.

The Orowan bypassing and shearing mechanisms are alternative methods for predicting the strengthening effect of MgSi-based precipitates. A critical diameter between particle bypassing and shearing of 15 nm was used, according to Ref. [66]. Peak aging conditions such as T5-1 and T6-3 can include the simultaneous operation of both mechanisms due to the presence of a certain particle size distribution. Their combined effect can be quantified by calculating their harmonic mean, which defines the overall strengthening contribution of MgSi precipitation using the following equation [67, 68]:

$$\sigma_{MgSi\text{-based Precipitate}} = \left[\frac{1}{\sigma_{Orowan}} + \frac{1}{\sigma_{Shearing}}\right]^{-1} \quad (11)$$

The values of the above-mentioned microstructural parameters in the F, T5-1, SR, and T6-3 conditions are given in Table 2-3. A plot of the predicted YS contributions from the different microstructural components and a comparison with the experimental YS is shown in Figure 2-14. In general, the predicted YS agrees well with the experimental data.

This modeling approach clearly demonstrates that the solid solution and cell size strengthening are most pronounced in the F condition. If the fine α-Al(Mn,Fe)Si intermetallic particles that were observed in the Si-rich network had been included in the model, then the predicted strength would have been slightly higher. All heat treatments led to a reduction in the solid solution strengthening. In the T5-1 condition, the cell size strengthening remained the same as in the F condition due to the low-temperature treatment. Precipitation strengthening from Si-rich nanoparticles and MgSi-based precipitates became the main strengthening mechanisms, and the strengthening from Si-rich nanoparticles played a major role. Therefore, the T5 condition exhibited a significant increase in the overall YS relative to the F condition and achieved the highest YS among all the studied heat treatment conditions.

In the SR condition, the Si-rich network started to break up and hence the cell size strengthening was weakened. Furthermore, the precipitation strengthening from nanosized Si-rich particles was lower due to their lower volume fraction. Those two factors plus the lack of MgSi-based precipitates resulted in the lowest overall YS among all conditions studied.

In the T6-3 condition, a large number of MgSi-based precipitates provided the main strengthening contribution. In addition, a number of α-dispersoids precipitated in the Al matrix during the T6 solution treatment, and this provided supplementary strengthening.

The strengthening from both MgSi-based precipitates and α-dispersoids helped offset the strength loss from the SR condition. The overall YS of the T6-3 condition became higher than that of the F condition but was still lower than that of the T5-1 condition.

It has already been noted that for die castings, the main reason for adding Mn to AlSi10Mg alloys is to prevent die soldering, and in addition, the formation of α-Al(Fe,Mn)Si dispersoids during solution treatment can also enhance the T6 strength in some extent [24-26]. By contrast, the faster solidification rate in the SLM process (where die soldering is not an issue) allows more Mn to be placed in solution and then to precipitate out more finely, which can significantly improve the mechanical performance compared to conventional castings.

Table 2-3: Microstructural parameters used in equations 4-11.

Parameter	Description	Unit		Values				Reference
				F	T5-1	SR	T6-3	
C_{ss}	Solute in solution	Wt.%	Si	2.8	1.5	1.7	1.2	TEM-EDS
			Mg	0.11	0	0	0	
			Mn	0.13	0.13	0.13	0	
d_b	Cell size/ Grain size	μm		0.49	0.49	10	10	SEM and EBSD (Figure 2-8, Figure 2-9)
d_p	Particle size	nm	Si-rich (diameter)	4.76	15.8	5.58	-	TEM (Figure 2-11, Figure 2-12)
			MgSi-based (length)	-	78.3	-	45.0	
			α-Al(Mn,Fe)Si (diameter)	-	-	-	97.0	
f_v	Volume fraction	%	Si-rich	0.14	0.4	0.19	-	TEM (Figure 2-11, Figure 2-12)
			MgSi-based	-	1	-	2	
			α-Al(Mn,Fe)Si	-	-	-	2.3	

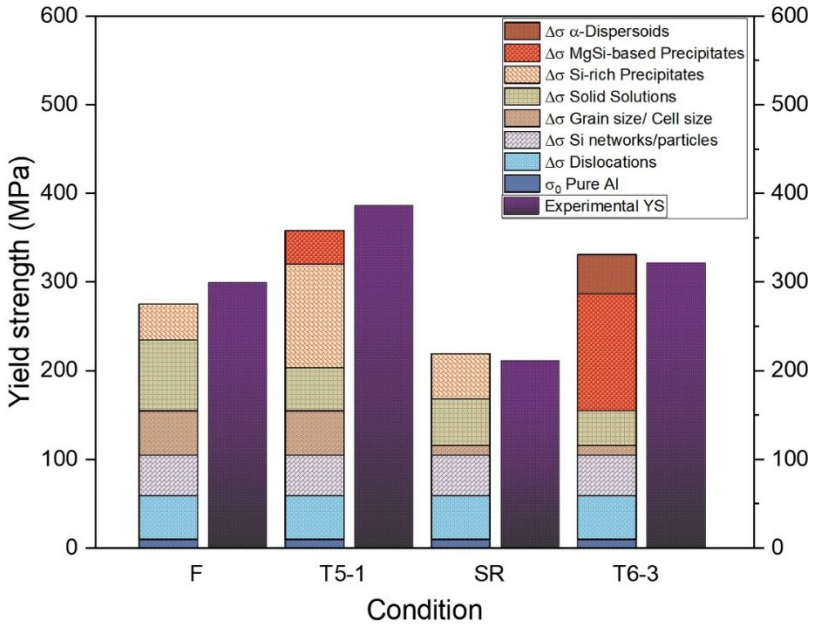

Figure 2-14: Comparison of the predicted and experimental YS for the four conditions studied.

2.4.3 Comparison of mechanical properties for various Al-Si based alloys made by SLM

Various studies have been carried out on different SLMed aluminum alloys, mostly focusing on high Si alloys because of their excellent printability. Table 2-4 shows a comparison of the mechanical properties of the current AlSi10MgMn alloy with previously reported Al-Si based SLM alloys in as-fabricated and differently heat-treated conditions. The comparative analysis was performed for three separate groups of various Al-Si-based alloys produced via SLM.

The first group is for the most commonly used AlSi10Mg alloy in the F condition. The YS of this group was less than 265 MPa and the elongation was less than 10%. The current AlSi10MgMn alloy exhibited a YS of 299 MPa with an elongation of 10.3%, which surpassed those of the conventional AlSi10Mg alloys reported in the literature by a margin

of at least 10%. This is likely due to the higher levels of Mg and Mn in the AlSi10MgMn alloy in comparison with conventional AlSi10Mg, which enhance the solid solution strengthening and reinforce the Si-rich network through the precipitation of α-Al(Mn,Fe)Si particles (Figure 2-11a).

The impact of different heat treatments on the tensile properties of AlSi10Mg alloys has been shown in the second group. The conventional AlSi10Mg alloys are reported to have a YS of up to about 310 MPa with an elongation range of 3-8% in the T5 condition. By contrast, the current AlSi10MgMn alloy achieved a YS of 386 MPa and an elongation of 9.4%, which was attributed to the precipitation of a large amount of Si nanoparticles and MgSi-based precipitates (Figure 2-11e and Figure 2-14). In the T6 condition, the conventional AlSi10Mg alloys presented a YS range of 174-239 MPa with an elongation of less than 10%, whereas the current AlSi10MgMn alloy exhibited a YS of 321 MPa with an elongation of 12%. From the results of Figure 2-12b and Figure 2-14, the formation of submicron α-Al(Mn,Fe)Si dispersoids induced by Mn-alloying provided a supplementary strengthening contribution, resulting in a superior strength relative to the AlSi10Mg counterparts in the T6 condition. For the stress-relieved condition (SR), the current alloy does not show any obvious benefits with respect to its AlSi10Mg counterparts.

Another interesting group in Table 2-4 relates to the development of modified high-Si alloys for SLM applications. In the pursuit of enhancing the mechanical performance of Al-Si-based alloys, researchers have often added alloying elements, such as Sc, Er, and Zr, or have created composite materials by integrating particulates like TiB_2 or Al_2O_3. In most cases, such approaches resulted in a substantial enhancement of the strength in the F condition relative to conventional AlSi10Mg. However, there is little information about the

effects of heat treatments on such modified alloys in the literature. In addition, these modification processes often require additional processing steps that come at an extra cost.

Table 2-4: Comparison of the mechanical properties of the current AlSi10MgMn alloy with various Al-Si based alloys made by SLM.

Group	Alloy	Yield Strength (MPa)	Elongation (%)	Heat treatment condition	References
I (F)	AlSi10MgMn	299	10.3	F	Present study
	AlSi10Mg	227	7.4	F	[32]
	AlSi10Mg	250	9	F	[11]
	AlSi10Mg	260	6.5	F	[14]
	AlSi10Mg	263	9.8	F	[46]
II (Heat treated)	AlSi10MgMn	386	9.4	T5	Present study
	AlSi10Mg	295	~8%	T5	[11]
	AlSi10Mg	310	6.2	T5	[46]
	AlSi10MgMn	321	11.7	T6	Present study
	AlSi10Mg	239	3.9	T6	[34]
	AlSi10Mg	180	9.6	T6	[46]
	AlSi10Mg	174	9.2	T6	[69]
	AlSi10MgMn	211	17.4	Stress relief	Present study
	AlSi10Mg	210	~15%	Stress relief	[11]
	AlSi10Mg	182	17.9	Stress relief	[70]
III (Modified alloys)	Sc modified AlSi10Mg	~300*	6	F	[21]
	Er-Zr modified Al–7Si-0.6 Mg	333	12.5	F	[71]
	SiC-AlSi10Mg	360	~1	F	[72]
	2%wt TiB_2-AlSi10Mg	283	4.2	F	[73]
	In situ Al_2O_3-AlSi10Mg	~250	4.3	F	[74]

* Converted from HV results, assuming that the yield stress is three times the hardness **[75]**.

2.5 Conclusions

1- An AlSi10MgMn alloy containing 0.5 wt% Mn was manufactured by the SLM process for the first time. This alloy achieved yield strength (YS) values of 299, 386, and 321 MPa in the as-fabricated (F), directly-aged (T5), and solution treated plus aged (T6) conditions, respectively. The tensile properties of the AlSi10MgMn alloy were

considerably higher than those reported for conventional AlSi10Mg alloys in the F, T5, and T6 conditions.

2- In the F condition, a high number density of fine Si-rich nanoparticles was observed in the Al cells, along with some fine α-Al(Mn,Fe)Si intermetallic particles in the Si-rich network. Together with a high amount of solid solution strengthening, this resulted in a YS improvement by a margin of 10% compared to conventional AlSi10Mg alloys.

3- In the T5 condition, a large number of Si-rich nanoparticles and MgSi-based precipitates were present in the Al cells, and the continuous Si-rich network was still intact. Precipitation strengthening from these nanosized Si-rich and MgSi-based precipitates became the main strengthening mechanism, with strengthening from the Si-rich nanoparticles playing a major role.

4- In the T6 condition, a large number of MgSi-based precipitates was identified as the main strengthening component. In addition, α-Al(Mn,Fe)Si dispersoids induced by the Mn addition precipitated in the aluminum matrix and provided supplementary strengthening.

5- Constitutive models based on microstructural characteristics were applied to explain strengthening mechanisms and to predict the YS contributions in different process conditions. The predicted YS values were in good agreement with the experimentally measured data.

References

[1] E.M. Sefene, State-of-the-art of selective laser melting process: A comprehensive review, Journal of Manufacturing Systems 63 (2022) 250-274.https://doi.org/10.1016/j.jmsy.2022.04.002

[2] Z. Liu, D. Zhao, P. Wang, M. Yan, C. Yang, Z. Chen, J. Lu, Z. Lu, Additive manufacturing of metals: Microstructure evolution and multistage control, Journal of Materials Science & Technology 100 (2022) 224-236.https://doi.org/10.1016/j.jmst.2021.06.011

[3] N.T. Aboulkhair, M. Simonelli, L. Parry, I. Ashcroft, C. Tuck, R. Hague, 3D printing of Aluminium alloys: Additive Manufacturing of Aluminium alloys using selective laser melting, Progress in Materials Science 106 (2019).https://doi.org/10.1016/j.pmatsci.2019.100578

[4] P.A. Rometsch, Y. Zhu, X. Wu, A. Huang, Review of high-strength aluminium alloys for additive manufacturing by laser powder bed fusion, Materials & Design 219 (2022) 110779.https://doi.org/10.1016/j.matdes.2022.110779

[5] Q. Jia, P. Rometsch, S. Cao, K. Zhang, X. Wu, Towards a high strength aluminium alloy development methodology for selective laser melting, Materials & Design 174 (2019) 107775.https://doi.org/10.1016/j.matdes.2019.107775

[6] E.O. Olakanmi, R.F. Cochrane, K.W. Dalgarno, A review on selective laser sintering/melting (SLS/SLM) of aluminium alloy powders: Processing, microstructure, and properties, Progress in Materials Science 74 (2015) 401-477.https://doi.org/10.1016/j.pmatsci.2015.03.002

[7] R. Khajeh, M. Javidani, M. Mofarrehi, X.G. Chen, M. Ahmed, A. Farzaneh, A. Heidarzadeh, Enhancing microstructure and mechanical properties of laser powder bed fusion-fabricated AlSi10Mg alloy through tailored friction stir processing and post-heat treatment, Materials Science and Engineering: A 889 (2024) 145855.https://doi.org/10.1016/j.msea.2023.145855

[8] J. Měsíček, T. Čegan, Q.-P. Ma, R. Halama, K. Skotnicová, J. Hajnyš, J. Juřica, P. Krpec, M. Pagáč, Effect of artificial aging on the strength, hardness, and residual stress of SLM AlSi10Mg parts prepared from the recycled powder, Materials Science and Engineering: A 855 (2022) 143900.https://doi.org/10.1016/j.msea.2022.143900

[9] N. Limbasiya, A. Jain, H. Soni, V. Wankhede, G. Krolczyk, P. Sahlot, A comprehensive review on the effect of process parameters and post-process treatments on microstructure and mechanical properties of selective laser melting of AlSi10Mg, Journal of Materials Research and Technology 21 (2022) 1141-1176.https://doi.org/10.1016/j.jmrt.2022.09.092

[10] A.H. Maamoun, M. Elbestawi, G.K. Dosbaeva, S.C. Veldhuis, Thermal post-processing of AlSi10Mg parts produced by Selective Laser Melting using recycled powder, Additive Manufacturing 21 (2018) 234-247.https://doi.org/10.1016/j.addma.2018.03.014

[11] P. Van Cauwenbergh, V. Samaee, L. Thijs, J. Nejezchlebova, P. Sedlak, A. Ivekovic, D. Schryvers, B. Van Hooreweder, K. Vanmeensel, Unravelling the multi-scale structure-property relationship of laser powder bed fusion processed and heat-treated AlSi10Mg, Sci Rep 11(1) (2021) 6423.https://doi.org/10.1038/s41598-021-85047-2

[12] M. Fousová, D. Dvorský, A. Michalcová, D. Vojtěch, Changes in the microstructure and mechanical properties of additively manufactured AlSi10Mg alloy after exposure to elevated temperatures, Materials Characterization 137 (2018) 119-126.https://doi.org/10.1016/j.matchar.2018.01.028

[13] J. Fite, S. Eswarappa Prameela, J.A. Slotwinski, T.P. Weihs, Evolution of the microstructure and mechanical properties of additively manufactured AlSi10Mg during room temperature holds and low temperature aging, Additive Manufacturing 36 (2020).https://doi.org/10.1016/j.addma.2020.101429

[14] S. Chen, Q. Tan, W. Gao, G. Wu, J. Fan, Z. Feng, T. Huang, A.W. Godfrey, M. Zhang, X. Huang, Effect of heat treatment on the anisotropy in mechanical properties of selective laser melted AlSi10Mg, Materials Science and Engineering: A 858 (2022) 144130.https://doi.org/10.1016/j.msea.2022.144130

[15] S.Y. Ahn, J. Moon, Y.T. Choi, E.S. Kim, S.G. Jeong, J.M. Park, M. Kang, H. Joo, H.S. Kim, A precipitation-hardened AlSi10Mg alloy fabricated using selective laser melting, Materials Science and Engineering: A 844 (2022) 143164.https://doi.org/10.1016/j.msea.2022.143164

[16] K.G. Prashanth, S. Scudino, H.J. Klauss, K.B. Surreddi, L. Löber, Z. Wang, A.K. Chaubey, U. Kühn, J. Eckert, Microstructure and mechanical properties of Al–12Si produced by selective laser melting: Effect of heat treatment, Materials Science and Engineering: A 590 (2014) 153-160.https://doi.org/10.1016/j.msea.2013.10.023

[17] L. Zhou, A. Mehta, E. Schulz, B. McWilliams, K. Cho, Y. Sohn, Microstructure, precipitates and hardness of selectively laser melted AlSi10Mg alloy before and after heat treatment, Materials Characterization 143 (2018) 5-17.https://doi.org/10.1016/j.matchar.2018.04.022

[18] Z. Wang, L. Zhuo, E. Yin, Z. Zhao, Microstructure evolution and properties of nanoparticulate SiC modified AlSi10Mg alloys, Materials Science and Engineering: A 808 (2021).https://doi.org/10.1016/j.msea.2021.140864

[19] D. Gu, H. Wang, D. Dai, Laser Additive Manufacturing of Novel Aluminum Based Nanocomposite Parts: Tailored Forming of Multiple Materials, Journal of Manufacturing Science and Engineering 138(2) (2015).https://doi.org/10.1115/1.4030376

[20] A. Martin, M. San Sebastian, E. Gil, C.Y. Wang, S. Milenkovic, M.T. Pérez-Prado, C.M. Cepeda-Jiménez, Effect of the heat treatment on the microstructure and hardness evolution of a AlSi10MgCu alloy designed for laser powder bed fusion, Materials Science and Engineering: A 819 (2021).https://doi.org/10.1016/j.msea.2021.141487

[21] Y. Chen, L. Wang, Z. Feng, W. Zhang, Effects of heat treatment on microstructure and mechanical properties of SLMed Sc-modified AlSi10Mg alloy, Progress in Natural

Science: Materials International 31(5) (2021) 714-721.https://doi.org/10.1016/j.pnsc.2021.08.003

[22] J. Fiocchi, C.A. Biffi, A. Tuissi, Selective laser melting of high-strength primary AlSi9Cu3 alloy: Processability, microstructure, and mechanical properties, Materials & Design 191 (2020) 108581.https://doi.org/10.1016/j.matdes.2020.108581

[23] B. Zhang, W. Wei, W. Shi, Y. Guo, S. Wen, X. Wu, K. Gao, L. Rong, H. Huang, Z. Nie, Effect of heat treatment on the microstructure and mechanical properties of Er-containing Al–7Si–0.6 Mg alloy by laser powder bed fusion, Journal of Materials Research and Technology 18 (2022) 3073-3084.https://doi.org/10.1016/j.jmrt.2022.04.023

[24] Z. Chen, E.M. Elgallad, K. Liu, X.G. Chen, Precipitation Characteristics of HPVDC AlSi10Mg0.3Mn Alloy Under Different Temper Conditions, Metallography, Microstructure, and Analysis (2022).https://doi.org/10.1007/s13632-022-00858-7

[25] Q. Cai, C.L. Mendis, I.T.H. Chang, Z. Fan, Microstructure evolution and mechanical properties of new die-cast Al-Si-Mg-Mn alloys, Materials & Design 187 (2020) 108394.https://doi.org/10.1016/j.matdes.2019.108394

[26] H.J. Kang, J.Y. Park, Y.S. Choi, D.H. Cho, Influence of the solution and artificial aging treatments on the microstructure and mechanical properties of die-cast Al–Si–Mg alloys, Metals 12(1) (2022).https://doi.org/10.3390/met12010071

[27] W. Zhang, S. Ma, Z. Wei, P. Bai, The Relationship between Residual Amount of Sr and Morphology of Eutectic Si Phase in A356 Alloy, Materials 12(19) (2019) 3222.https://doi.org/10.3390/ma12193222

[28] L. Han, X. Wu, J. Zhu, M. Bai, X. Zheng, Z. Zhang, Study on Microstructures and Properties of the Al. Alloy Vacuum Die-Cast Parts of TL117 and C611, Journal of Physics: Conference Series, 2023.https://doi.org/10.1088/1742-6596/2468/1/012111

[29] S.M. Allen, Foil thickness measurements from convergent-beam diffraction patterns, Philosophical Magazine A 43(2) (1981) 325-335.https://doi.org/10.1080/01418618108239412

[30] A.Y. Algendy, K. Liu, P. Rometsch, N. Parson, X.G. Chen, Effects of AlMn dispersoids and Al3(Sc,Zr) precipitates on the microstructure and ambient/elevated-temperature mechanical properties of hot-rolled AA5083 alloys, Materials Science and Engineering: A 855 (2022) 143950.https://doi.org/10.1016/j.msea.2022.143950

[31] O. Engler, C.D. Marioara, Y. Aruga, M. Kozuka, O.R. Myhr, Effect of natural ageing or pre-ageing on the evolution of precipitate structure and strength during age hardening of Al–Mg–Si alloy AA 6016, Materials Science and Engineering: A 759 (2019) 520-529.https://doi.org/10.1016/j.msea.2019.05.073

[32] M.S. Bisht, V. Gaur, I.V. Singh, On mechanical properties of SLM Al–Si alloy: Role of heat treatment-induced evolution of silicon morphology, Materials Science and Engineering: A 858 (2022) 144157.https://doi.org/10.1016/j.msea.2022.144157

[33] I. Rosenthal, R. Shneck, A. Stern, Heat treatment effect on the mechanical properties and fracture mechanism in AlSi10Mg fabricated by additive manufacturing selective laser

melting process, Materials Science and Engineering: A 729 (2018) 310-322.https://doi.org/10.1016/j.msea.2018.05.074

[34] N.T. Aboulkhair, I. Maskery, C. Tuck, I. Ashcroft, N.M. Everitt, The microstructure and mechanical properties of selectively laser melted AlSi10Mg: The effect of a conventional T6-like heat treatment, Materials Science and Engineering: A 667 (2016) 139-146.https://doi.org/10.1016/j.msea.2016.04.092

[35] P. Mohammadpour, A. Plotkowski, A.B. Phillion, Revisiting solidification microstructure selection maps in the frame of additive manufacturing, Additive Manufacturing 31 (2020).https://doi.org/10.1016/j.addma.2019.100936

[36] J.G. Santos Macías, T. Douillard, L. Zhao, E. Maire, G. Pyka, A. Simar, Influence on microstructure, strength and ductility of build platform temperature during laser powder bed fusion of AlSi10Mg, Acta Mater 201 (2020) 231-243.https://doi.org/10.1016/j.actamat.2020.10.001

[37] N. Takata, H. Kodaira, K. Sekizawa, A. Suzuki, M. Kobashi, Change in microstructure of selectively laser melted AlSi10Mg alloy with heat treatments, Materials Science and Engineering: A 704 (2017) 218-228.https://doi.org/10.1016/j.msea.2017.08.029

[38] H. Hyer, L. Zhou, S. Park, G. Gottsfritz, G. Benson, B. Tolentino, B. McWilliams, K. Cho, Y. Sohn, Understanding the Laser Powder Bed Fusion of AlSi10Mg Alloy, Metallography, Microstructure, and Analysis 9(4) (2020) 484-502.https://doi.org/10.1007/s13632-020-00659-w

[39] D. Knoop, A. Lutz, B. Mais, A. von Hehl, A Tailored AlSiMg Alloy for Laser Powder Bed Fusion, Metals 10(4) (2020).https://doi.org/10.3390/met10040514

[40] M. Schuch, T. Hahn, M. Bleckmann, The mechanical behavior and microstructure of additively manufactured AlSi10Mg for different material states and loading conditions, Materials Science and Engineering: A 813 (2021).https://doi.org/10.1016/j.msea.2021.141134

[41] N. Takata, M. Liu, H. Kodaira, A. Suzuki, M. Kobashi, Anomalous strengthening by supersaturated solid solutions of selectively laser melted Al–Si-based alloys, Additive Manufacturing 33 (2020).https://doi.org/10.1016/j.addma.2020.101152

[42] K.V. Yang, P. Rometsch, C.H.J. Davies, A. Huang, X. Wu, Effect of heat treatment on the microstructure and anisotropy in mechanical properties of A357 alloy produced by selective laser melting, Materials & Design 154 (2018) 275-290.https://doi.org/10.1016/j.matdes.2018.05.026

[43] M.-S. Baek, R. Kreethi, T.-H. Park, Y. Sohn, K.-A. Lee, Influence of heat treatment on the high-cycle fatigue properties and fatigue damage mechanism of selective laser melted AlSi10Mg alloy, Materials Science and Engineering: A 819 (2021) 141486.https://doi.org/10.1016/j.msea.2021.141486

[44] N. Tabatabaei, A. Zarei-Hanzaki, A. Moshiri, H.R. Abedi, The effect of heat treatment on the room and high temperature mechanical properties of AlSi10Mg alloy fabricated by

selective laser melting, Journal of Materials Research and Technology 23 (2023) 6039-6053.https://doi.org/10.1016/j.jmrt.2023.02.086

[45] L. Růžičková, J. Sobotová, L. Beránek, L. Pelikán, J. Šimota, Influence of Stress Relief Annealing Parameters on Mechanical Properties and Decomposition of Eutectic Si Network of L-PBF Additive Manufactured Alloy AlSi10Mg, Metals 12(9) (2022).https://doi.org/10.3390/met12091497

[46] T.-H. Park, M.-S. Baek, H. Hyer, Y. Sohn, K.-A. Lee, Effect of direct aging on the microstructure and tensile properties of AlSi10Mg alloy manufactured by selective laser melting process, Materials Characterization 176 (2021).https://doi.org/10.1016/j.matchar.2021.111113

[47] A. Hadadzadeh, C. Baxter, B.S. Amirkhiz, M. Mohammadi, Strengthening mechanisms in direct metal laser sintered AlSi10Mg: Comparison between virgin and recycled powders, Additive Manufacturing 23 (2018) 108-120.https://doi.org/10.1016/j.addma.2018.07.014

[48] U. Gebhardt, T. Gustmann, L. Giebeler, F. Hirsch, J.K. Hufenbach, M. Kästner, Additively manufactured AlSi10Mg lattices – Potential and limits of modelling as-designed structures, Materials & Design 220 (2022) 110796.https://doi.org/10.1016/j.matdes.2022.110796

[49] D. Li, R. Qin, J. Xu, B. Chen, X. Niu, Effect of heat treatment on AlSi10Mg lattice structure manufactured by selective laser melting: Microstructure evolution and compression properties, Materials Characterization 187 (2022) 111882.https://doi.org/10.1016/j.matchar.2022.111882

[50] F. Bosio, C. Phutela, N. Ghisi, A. Alhammadi, N.T. Aboulkhair, Tuning the microstructure and mechanical properties of AlSi10Mg alloy via in-situ heat-treatments in laser powder bed fusion, Materials Science and Engineering: A 879 (2023) 145268.https://doi.org/10.1016/j.msea.2023.145268

[51] L. Zhao, L. Song, J.G. Santos Macías, Y. Zhu, M. Huang, A. Simar, Z. Li, Review on the correlation between microstructure and mechanical performance for laser powder bed fusion AlSi10Mg, Additive Manufacturing 56 (2022).https://doi.org/10.1016/j.addma.2022.102914

[52] H. Wu, Y. Ren, J. Ren, L. Liang, R. Li, Q. Fang, A. Cai, Q. Shan, Y. Tian, I. Baker, Selective laser melted AlSi10Mg alloy under melting mode transition: Microstructure evolution, nanomechanical behaviors and tensile properties, Journal of Alloys and Compounds 873 (2021) 159823.https://doi.org/10.1016/j.jallcom.2021.159823

[53] M. Albu, R. Krisper, J. Lammer, G. Kothleitner, J. Fiocchi, P. Bassani, Microstructure evolution during in-situ heating of AlSi10Mg alloy powders and additive manufactured parts, Additive Manufacturing 36 (2020).https://doi.org/10.1016/j.addma.2020.101605

[54] J. Fiocchi, A. Tuissi, C.A. Biffi, Heat treatment of aluminium alloys produced by laser powder bed fusion: A review, Materials & Design 204 (2021) 109651.https://doi.org/10.1016/j.matdes.2021.109651

[55] J.H. Rao, Y. Zhang, K. Zhang, A. Huang, C.H.J. Davies, X. Wu, Multiple precipitation pathways in an Al-7Si-0.6Mg alloy fabricated by selective laser melting, Scripta Materialia 160 (2019) 66-69.https://doi.org/10.1016/j.scriptamat.2018.09.045

[56] S.J. Andersen, H.W. Zandbergen, J. Jansen, C. TrÆholt, U. Tundal, O. Reiso, The crystal structure of the β″ phase in Al–Mg–Si alloys, Acta Mater 46(9) (1998) 3283-3298.https://doi.org/10.1016/S1359-6454(97)00493-X

[57] S.J. Andersen, Quantification of the Mg2Si β″ and β′ phases in AlMgSi alloys by transmission electron microscopy, Metallurgical and Materials Transactions A 26(8) (1995) 1931-1937.https://doi.org/10.1007/BF02670664

[58] M. Avateffazeli, S.I. Shakil, A. Hadadzadeh, B. Shalchi-Amirkhiz, H. Pirgazi, M. Mohammadi, M. Haghshenas, On microstructure and work hardening behavior of laser powder bed fused Al-Cu-Mg-Ag-TiB2 and AlSi10Mg alloys, Materials Today Communications 35 (2023).https://doi.org/10.1016/j.mtcomm.2023.105804

[59] E. Ghio, E. Cerri, Work Hardening of Heat-Treated AlSi10Mg Alloy Manufactured by Selective Laser Melting: Effects of Layer Thickness and Hatch Spacing, Materials (Basel) 14(17) (2021).https://doi.org/10.3390/ma14174901

[60] D.-K. Kim, W. Woo, J.-H. Hwang, K. An, S.-H. Choi, Stress partitioning behavior of an AlSi10Mg alloy produced by selective laser melting during tensile deformation using in situ neutron diffraction, Journal of Alloys and Compounds 686 (2016) 281-286.https://doi.org/10.1016/j.jallcom.2016.06.011

[61] O.R. Myhr, Ø. Grong, H.G. Fjær, C.D. Marioara, Modelling of the microstructure and strength evolution in Al–Mg–Si alloys during multistage thermal processing, Acta Mater 52(17) (2004) 4997-5008.https://doi.org/10.1016/j.actamat.2004.07.002

[62] A. Hadadzadeh, B.S. Amirkhiz, J. Li, M. Mohammadi, Columnar to equiaxed transition during direct metal laser sintering of AlSi10Mg alloy: Effect of building direction, Additive Manufacturing 23 (2018) 121-131.https://doi.org/10.1016/j.addma.2018.08.001

[63] A. Simar, Y. Bréchet, B. de Meester, A. Denquin, T. Pardoen, Sequential modeling of local precipitation, strength and strain hardening in friction stir welds of an aluminum alloy 6005A-T6, Acta Mater 55(18) (2007) 6133-6143.https://doi.org/10.1016/j.actamat.2007.07.012

[64] N. Hansen, Hall–Petch relation and boundary strengthening, Scripta Materialia 51(8) (2004) 801-806.https://doi.org/10.1016/j.scriptamat.2004.06.002

[65] A. Starke Edgar, Heat-Treatable Aluminum Alloys, Aluminum AlloysContemporary Research and Applications 31 (1989) 35

[66] X. Zhang, L.K. Huang, B. Zhang, Y.Z. Chen, F. Liu, Microstructural evolution and strengthening mechanism of an Al–Si–Mg alloy processed by high-pressure torsion with different heat treatments, Materials Science and Engineering: A 794 (2020).https://doi.org/10.1016/j.msea.2020.139932

[67] H.R. Shercliff, M.F. Ashby, A process model for age hardening of aluminium alloys—I. The model, Acta Metallurgica et Materialia 38(10) (1990) 1789-1802.https://doi.org/10.1016/0956-7151(90)90291-N

[68] P.A. Rometsch, G.B. Schaffer, An age hardening model for Al–7Si–Mg casting alloys, Materials Science and Engineering: A 325(1) (2002) 424-434.https://doi.org/10.1016/S0921-5093(01)01479-4

[69] L.F. Wang, J. Sun, X.L. Yu, Y. Shi, X.G. Zhu, L.Y. Cheng, H.H. Liang, B. Yan, L.J. Guo, Enhancement in mechanical properties of selectively laser-melted AlSi10Mg aluminum alloys by T6-like heat treatment, Materials Science and Engineering: A 734 (2018) 299-310.https://doi.org/10.1016/j.msea.2018.07.103

[70] M. Tang, P.C. Pistorius, Oxides, porosity and fatigue performance of AlSi10Mg parts produced by selective laser melting, International Journal of Fatigue 94 (2017) 192-201.https://doi.org/10.1016/j.ijfatigue.2016.06.002

[71] Y. Guo, W. Wei, H. Huang, S. Wen, W. Shi, X. Zhou, X. Wu, K. Gao, L. Rong, P. Qi, Z. Nie, Approaching an ultrafine microstructure and excellent tensile properties of a novel Er/Zr modified Al–7Si-0.6 Mg alloy fabricated by selective laser melting, Journal of Materials Research and Technology 22 (2023) 1625-1637.https://doi.org/10.1016/j.jmrt.2022.12.040

[72] D. Zhang, D. Yi, X. Wu, Z. Liu, W. Wang, R. Poprawe, J.H. Schleifenbaumc, S. Zieglerd, SiC reinforced AlSi10Mg composites fabricated by selective laser melting, Journal of Alloys and Compounds 894 (2022).https://doi.org/10.1016/j.jallcom.2021.162365

[73] L. Xi, D. Gu, S. Guo, R. Wang, K. Ding, K.G. Prashanth, Grain refinement in laser manufactured Al-based composites with TiB2 ceramic, Journal of Materials Research and Technology 9(3) (2020) 2611-2622.https://doi.org/10.1016/j.jmrt.2020.04.059

[74] S. Zhu, S. Song, Y. Chen, F. Zhao, W. Yang, Z. Li, Y. Shi, S. Yu, Effect of in-situ Al2O3 on tensile strength and ductility of AlSi10Mg alloy fabricated by selective laser melting, Materials Letters 308 (2022) 131108.https://doi.org/10.1016/j.matlet.2021.131108

[75] S.N. Khangholi, M. Javidani, A. Maltais, X.G. Chen, Effects of natural aging and pre-aging on the strength and electrical conductivity in Al-Mg-Si AA6201 conductor alloys, Materials Science and Engineering: A 820 (2021) 141538.https://doi.org/10.1016/j.msea.2021.141538

Chapter 3

Effect of Mn on Microstructural Characteristics and Mechanical Behavior of AlSi10Mg Alloys Produced by Selective Laser Melting

(This article is under internal review)

Abstract

This study investigated the effect of Mn modification on the microstructure and mechanical properties of AlSi10Mg alloys produced by selective laser melting (SLM). The results revealed that the addition of 0.5 wt.% Mn considerably improved the strength while maintaining a similar elongation level, exhibiting yield strength increases of 17%, 30% and 29% in the as-manufactured (F), directly aged (T5), and solution treated plus aged (T6) conditions, respectively. In the F and T5 conditions, the Mn-modification resulted in the formation of α-Al(Mn,Fe)Si intermetallic particles inside the Si-rich network, which reinforced the network and improved the strength. After the T6 heat treatment, the Si-rich network completely disappeared in both alloys, but the formation of α-Al(Mn,Fe)Si dispersoids provided an extra strengthening contribution in the Mn-modified alloy. Most importantly, transmission electron microscopy and atom probe tomography revealed that the addition of Mn (and some extra Mg) stimulated the precipitation of a large number of Si-rich nanoparticles and MgSi-based precipitates, especially in the T5 condition. Among all the heat treatment and alloy conditions investigated, the Mn-modified alloy in the T5 condition achieved the highest strengths (yield strength: 386 MPa, ultimate tensile strength: 532 MPa).

This research highlights the potential for improving the mechanical properties of AlSi10Mg alloys produced by SLM via a cost-effective modification of the chemical composition and provides a deeper understanding of the role of Mn in such alloys.

Keywords: Additive manufacturing, Laser powder bed fusion, AlSi10Mg alloys, Mn modification, Microstructure, Mechanical properties.

3.1 Introduction

Selective laser melting (SLM), also known as laser powder bed fusion (LPBF), is an emerging additive manufacturing (AM) technology that has gained attention in recent years owing to its capacity to fabricate materials with intricate and complex shapes in different industrial sectors such as the aerospace, automotive, and shipbuilding industries [1-5]. By overcoming the limitations of conventional casting, machining, and welding processes, SLM offers unparalleled capabilities for generating various structural components with intricate geometries that were previously unattainable. This process involves a layer-by-layer fabrication approach, in which a powdered material is spread across a platform and selectively solidified using a laser as the power source. Using computer-aided design, the process is able to create three-dimensional objects. During SLM, the molten pools have a rapid solidification rate (estimated to be up to 10^6 K/s), and therefore, the SLM samples develop exceptionally ultrafine microstructures. Furthermore, it can enhance the strength through various mechanisms, such as solid solution and precipitation hardening. Consequently, SLM enables the attainment of superior mechanical properties, thereby opening new opportunities for employing aluminum alloys to enhance the strength-to-weight ratio in different industrial applications [6-8].

Among various aluminum alloys, the AlSi10Mg alloy fabricated by SLM has gained considerable attention because of its low susceptibility to solidification cracking, good castability, excellent processability, and mostly adequate properties and widespread availability. The chemical composition of the alloy, being near the eutectic point, results in a narrower solidification temperature range, making it an ideal material for laser-based rapid solidification additive manufacturing like SLM [9-11]. Strengthening mechanisms, such as solid solution and precipitation hardening, play crucial roles in determining the mechanical properties of AlSi10Mg alloys under different heat treatment conditions [12, 13]. For instance, Fousova et al. [14] reported that T5 aging at 160 °C applied to an SLM-produced AlSi10Mg alloy enhanced the tensile yield strength while reducing the elongation. Ahn et al. [15] showed that direct annealing at 270 °C for 1.5 h led to the formation of nanoscale needle-like MgSi precipitates, which contributed to high mechanical properties. Hadadzadeh et al. [16] reported that the thermal cycling nature of SLM could result in the development of Si precipitates, Mg clusters, and MgSi precipitates. Lefebvre et al. [17] also reported the presence of Si and MgSi clusters in the as-manufactured condition. According to Li et al. [18], the presence of a fine fibrous Si phase in an AlSi10Mg alloy introduced a substantial interfacial energy structure. Under high-temperature heat treatment, the fibrous Si phase underwent a thermally activated growth process and transformed into Si particles. Kimura et al. [19] demonstrated that the Si-rich networks in an AlSi7Mg0.3 alloy were completely disrupted following an annealing treatment at 300 °C, resulting in a decrease in the tensile strength and an increase in the elongation.

Despite the notable characteristics that enhance the alloy processability during SLM, their mechanical properties are generally lower than those of high-strength wrought

aluminum alloys, such as 7xxx and 2xxx aluminum alloys [3, 20-22]. One method for enhancing the mechanical strength of AlSi10Mg alloys involves the introduction of reinforcing particles to fabricate composites with an AlSi10Mg matrix, which has been used recently for some ceramic particles, such as CNT [23], TiB_2 [24, 25], TiC [26], and SiC [27, 28]. It has been reported that a higher concentration can effectively improve the mechanical properties. However, incorporating these particles into the Al matrix can potentially create vulnerable regions for stress concentration and subsequent crack propagation at the particle interfaces. This can result in reduced ductility and diminished tensile strength.

Significant efforts have been made to enhance the mechanical properties of AlSi10Mg alloys by modifying their chemical composition. Chen et al. [29] revealed that with the introduction of 0.26 wt% Sc into the AlSi10Mg alloy, a refinement in the Si-rich network structure was achieved in addition to enhanced mechanical properties owing to the precipitation of finely dispersed Al_3Sc particles. Guo et al. [30] investigated the influence of the rare earth element Er along with Zr on the microstructure and mechanical properties of an AlSi7Mg alloy. The modification of Er and Zr facilitated the refinement of columnar grains, resulting in improved mechanical properties. Jandaghi et al. [31] evaluated the in-situ alloying of AlSi10Mg with Ni. The results showed that a reaction between Ni and the Al matrix in the melt pool resulted in the formation of Al_3Ni intermetallic. However, the Ni-rich intermetallic shells caused poor interfacial bonding to the Al matrix, leading to a reduction in the mechanical strength. A high Fe-content AlSi12 alloy was processed by SLM [32]. This led to an enhancement in mechanical properties in the as-fabricated condition, which was attributed to the combined effect of multiple strengthening mechanisms, including

solid solution strengthening, grain boundary strengthening, precipitation strengthening, and the presence of high-density stacking fault and Lomer Cottrell locks.

Fiocchi et al. [33] investigated the processability, microstructure, and mechanical properties of AlSi9Cu3 produced by SLM, resulting in enhanced mechanical properties owing to the high level of Cu and the presence of GP zones. Pozdniakov et al. [34] explored an AlSi11CuMn alloy produced via SLM, but found that the annealing and T6 heat treatment after SLM reduced the mechanical properties. Use of a Mn addition in Al-Si alloys was originally adopted in conventional casting to (a) reduce die soldering in high pressure die castings, and (b) to compensate for the harmful effect of Fe on mechanical properties by preventing the formation of the needle-like β-AlFeSi intermetallic phase [35]. However, systematic studies of Mn modification on the microstructure and mechanical properties of SLM-fabricated AlSi10Mg alloys have rarely been reported in the literature. It is also expected that increasing the Mn content can facilitate the use of recycled powder materials with high Fe contents, promoting energy efficiency and reducing the carbon footprint of the final SLM product.

In this study, two AlSi10Mg alloys, without and with Mn modification, were prepared and fabricated by the SLM process. The differences in microstructure and mechanical properties that resulted from the modification of Mn under different heat treatment conditions were systematically investigated. Microstructures of the two alloys were analyzed and compared using optical microscopy, scanning electron microscopy (SEM), electron backscatter diffraction (EBSD), transmission electron microscopy (TEM), and atom probe tomography (APT), and a correlation between microstructure and mechanical properties for SLM-fabricated AlSi10Mg(Mn) was established. This study

provides insights to enhance the mechanical properties of high-strength aluminum alloys produced by SLM, through cost-effective modification of the alloy chemical composition.

3.2 Experimental procedure

3.2.1 Materials preparation

Powder materials for the AlSi10Mg alloy (denoted as the 'Base alloy') and the Mn-modified AlSi10MgMn alloy (denoted as the 'Base+Mn alloy') were produced by standard atomization processes. The morphologies and sizes of both powder materials were similar. Representative SEM images showing the powder morphology of the Base+Mn alloy are presented in Figure 3-1a-b. The majority of the powder particles were relatively spherical, making them highly suitable for SLM, and most were within the size range of 10–30 μm, with an average particle size of approximately 21 μm (Figure 3-1c). The close-to-spherical shape of the particles is quantified in Figure 3-1d. The particle size distribution and sphericity were measured using ImageJ analysis software. The chemical compositions of both powders, analyzed by inductively coupled plasma spectroscopy, are listed in Table 3-1.

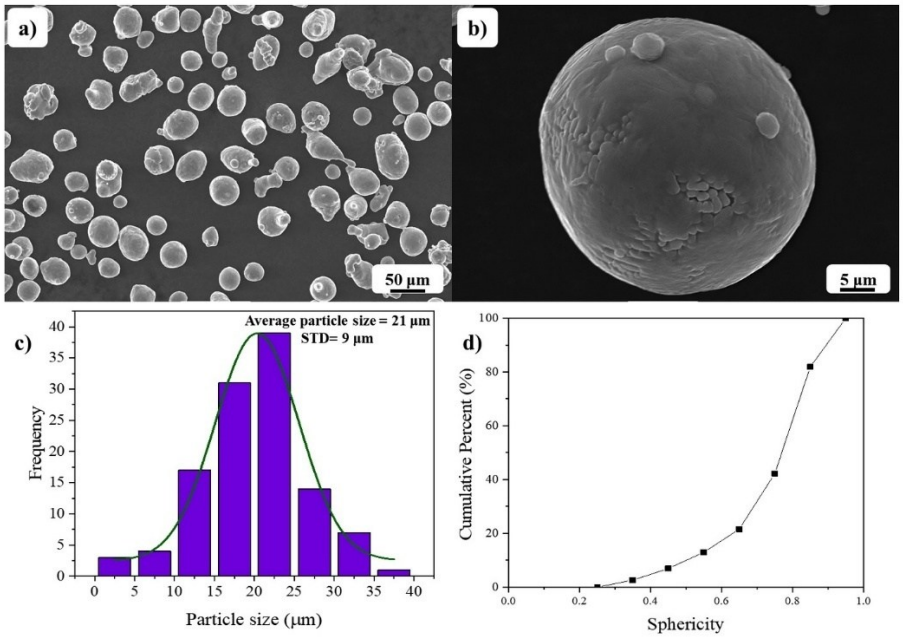

Figure 3-1: Characteristics of AlSi10MgMn powder: (a, b) morphology, (c) size distribution, (d) sphericity distribution (size and distribution were determined by using ImageJ).

Table 3-1: Chemical composition of raw powder feedstock determined by ICP (wt.%).

Alloy	Label	Chemical Composition (% wt)				
		Si	Fe	**Mn**	Mg	Ti
AlSi10Mg	**Base**	9.9	0.14	**0.005**	0.31	0.006
AlSi10MgMn	**Mn-B**	10.7	0.19	**0.51**	0.55	0.055

3.2.2 SLM process and heat treatment

The SLM specimens were fabricated at room temperature (i.e. without platform heating) using an SLM Solutions 125 machine equipped with a 400 W IPG fiber laser. The tensile specimens were printed with dimensions of 100 mm length, 6 mm thickness, and 12 mm height, oriented perpendicular to the build direction, as depicted in our previous publication [36]. The printing parameters for both alloys were configured as follows: a scan speed of 1650 mm/s, laser power of 350 W, powder layer thickness of 30 µm, hatch distance of 130 µm, laser spot size of 62 µm, and an adjacent layer rotation angle of 67°, resulting in an

energy density of 54.4 J mm^{-3}. Three heat treatment conditions (F, T5, and T6), detailed in Table 3-2, were chosen to compare the microstructure and mechanical properties of the two alloys.

Table 3-2: Labels used under different heat-treatment conditions.

Label	Heat treatment Condition	procedure
F	As manufactured	NA
T5	Direct aging	165°C, 8h
T6	Stress Relief + SHT + AA	300°C, 2h; 530°C, 0.5h; water quench; natural aging 24h; 165°C, 6h

3.2.3 Microstructure characterization

Microstructural analyses were conducted on polished samples using a SEM (JSM-6480LV) operated at 20 kV and equipped with an electron backscatter diffraction (EBSD) system. The grain structure and size were characterized using EBSD, acquired with a 0.5 μm step size, and the Kikuchi diffraction patterns were post-processed using the HKL Channel5 software (Oxford Instruments). To perform TEM analyses on the SLM samples, thin foils were first mechanically polished, followed by ion thinning using a Precision Ion Polishing System (Gatan Model 691). The precipitation microstructures were analyzed using a TEM (JEOL JEM-2100) operated at 200 kV and equipped with energy-dispersive spectroscopy (EDS). The size, number density, and volume fraction of all precipitates were quantified using the ImageJ analysis software from several recorded TEM images.

Specimens for APT analysis were prepared by site-specific lift-out from the polished SEM samples using a dual-column focused ion beam (FIB)/SEM instrument (FEI Quanta 3D), followed by annular milling to create sharp needle-like tips [37]. APT data were collected with a CAMECA Local Electrode Atom Probe (LEAP) 5000 XR instrument under

the following conditions: temperature set-point of 50 K, laser pulse energy of 150 pJ, laser pulse repetition rate of 200 kHz, and a detection rate of 1% (0.01 atoms per pulse). Data reconstruction and post-analysis were conducted using the AP Suite (version 6.3) software (CAMECA Instruments). In this study, iso-concentration surfaces and associated proximity histograms [38] were utilized for the identification and analysis of particles.

3.2.4 Mechanical properties

Vickers microhardness measurements were conducted on the polished samples using a Nextgen microhardness tester (NG-1000CCD). At least ten indents were tested to determine an average value for each sample. A load of 25 g and a dwell time of 20 s were applied during testing. Sub-sized tensile samples were machined from the printed plates, and tensile testing was conducted using an Instron 8801 servo-hydraulic machine with a strain rate of 3.3×10^{-4} s^{-1}, according to the ASTM-E8 standard. All tensile samples were tested with a gauge length of 25 mm in the horizontal orientation (perpendicular to the building direction) for all three heat treatment conditions (Table 3-2). At least three tensile samples were tested to obtain the average value for each condition.

3.3 Results

3.3.1 Mechanical properties

Figure 3-2 shows the tensile properties of the Base and Base+Mn alloys in the F, T5, and T6 conditions. Figure 3-2a displays typical engineering stress-strain curves, and the average tensile properties are graphed in Figure 3-2b. The Base+Mn alloy increased the yield strength (YS) in the F condition from 254 to 299 MPa (17.7% increment). Meanwhile, the

ultimate tensile strength (UTS) improved from 471 to 486 MPa (3.2% increment), and the elongation decreased from 12% to 10.3%, relative to the Base alloy. In the T5 condition, both alloys showed an increased yield strength compared to the F condition, while maintaining a similar elongation. The YS in the Base alloy increased to 296 MPa, and in the Base+Mn alloy, the YS increased more significantly from 299 to 386 MPa. In the T6 condition, the YS and UTS of both alloys decreased significantly in comparison with the T5 condition. However, the Base+Mn alloy exhibited better strength compared to the Base alloy (321 MPa vs. 249 MPa in YS, 384 MPa vs. 329 MPa in UTS). Among all alloy and heat treatment conditions, the T5 Base+Mn alloy achieved the highest tensile strength. The higher tensile properties of the Base+Mn samples in all conditions can be attributed to the microstructure changes induced by the chemical composition modification. This is described in detail in the following sections.

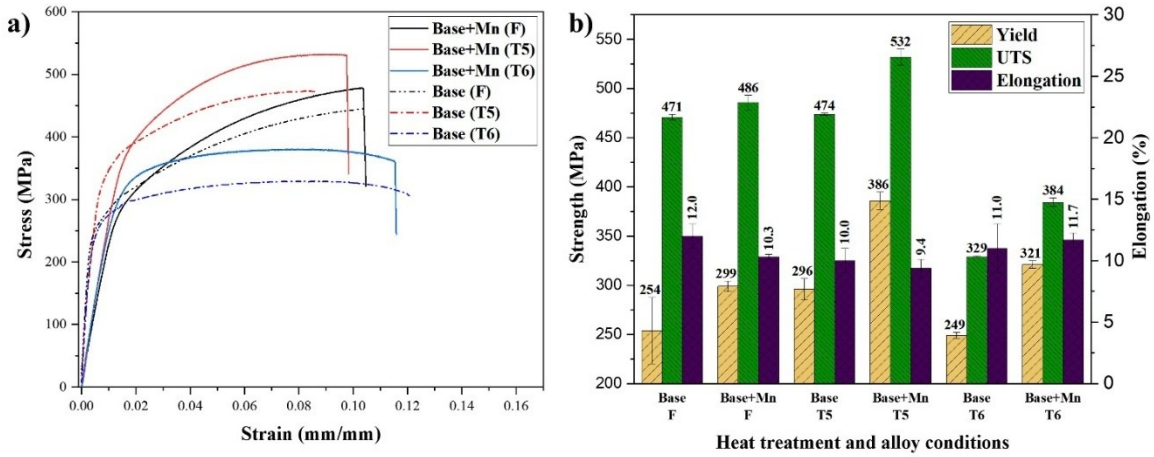

Figure 3-2: a) Typical engineering stress-strain curves and b) tensile properties of the Base and Base+Mn alloys under F, T5, and T6 conditions.

3.3.2 As-manufactured microstructures

As-manufactured microstructures parallel to the build direction in both alloys are shown in Figure 3-3. The EBSD inverse pole figure (IPF) maps in Figure 3-3a and 3-3b revealed a

predominance of columnar grains in both alloys, exhibiting epitaxial growth across most melt-pool boundaries. This phenomenon is indicative of directional solidification resulting from the high-temperature gradients inherent to the SLM process. It has been documented that most of the elongated grains are preferentially oriented in the <001> direction toward the center of the melt pool [39]. In addition, there are also some small equiaxed grains found at melt pool boundaries, which is consistent with most literature on SLM-produced AlSi10Mg alloys [40, 41]. For both alloys, the average grain size was 10 μm with a grain aspect ratio of 0.55, indicating a very similar grain structure.

SEM images in Figure 3-3c and 3-3d reveal a typical fish-scale structure for both the Base and Base+Mn alloys. The primary cause for the emergence of this structure can be attributed to variations in the cooling rate across the melt pools during solidification [42]. In the melt pool center (MPC), the material underwent rapid cooling, whereas a relatively lower cooling rate occurred at the melt pool boundary (MPB) [43]. The melt pools in both alloys show remarkable similarity, with average depths and widths of 66 μm and 132 μm, respectively. Typically, the energy density change during SLM can cause significant variations in these dimensions. However, owing to the consistent processing parameters applied during SLM for both alloys, the uniformity in melt pool shapes has been preserved in this study.

The microstructures at the MPC of the two alloys are shown in Figure 3-3e and 3-3f. Upon close examination of these images, similar microstructural characteristics were observed. Both alloys exhibited a cellular solidification composed of sub-micron primary α-Al cells surrounded by a fine Si-rich network. In these SEM images, the α-Al and Si-rich

networks were distinguishable by their distinct gray and light gray colors, respectively. For both samples, the average cell size in the MPC is 0.49±0.06 μm.

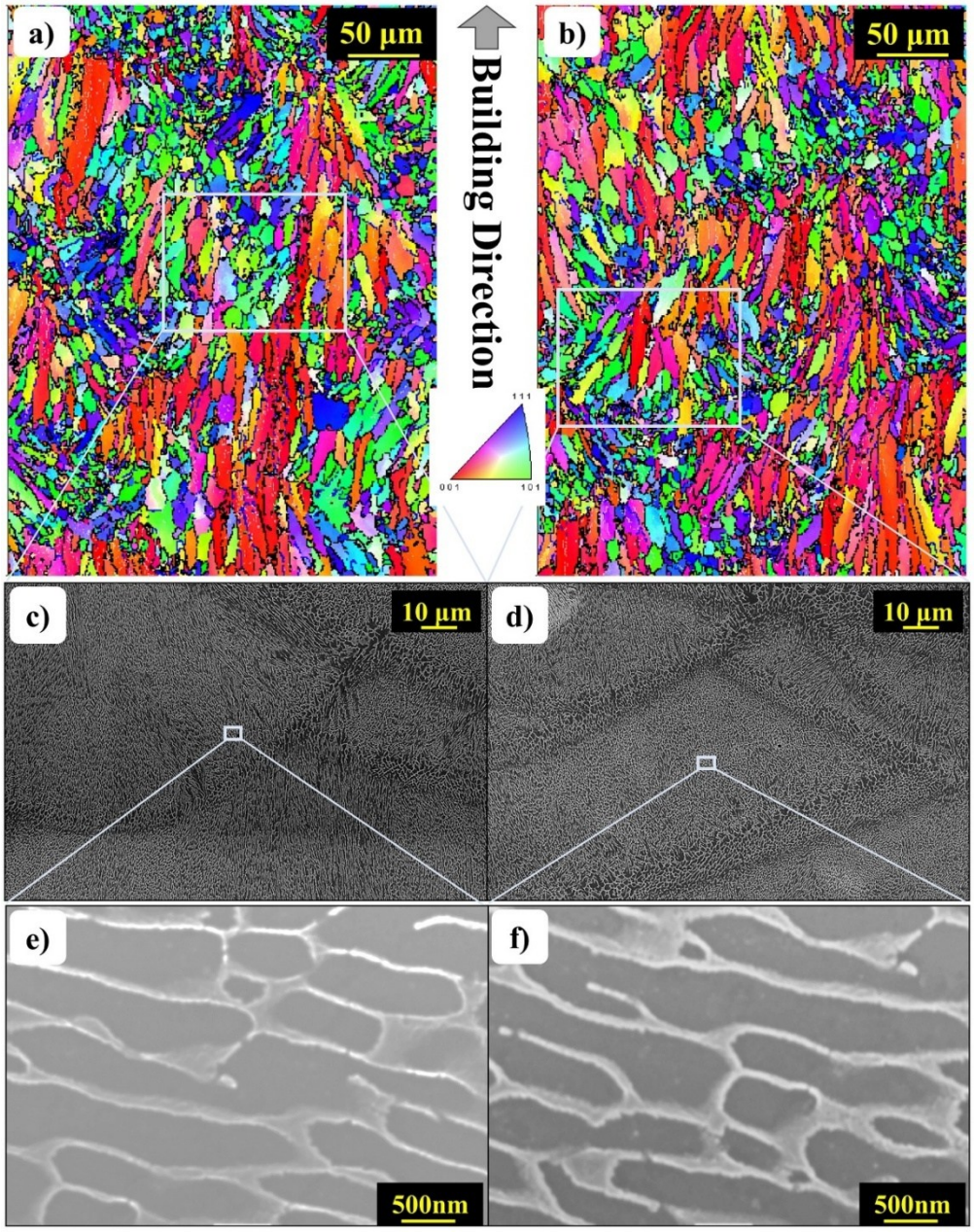

Figure 3-3: As-manufactured microstructures in the vertical section of the Base alloy (a, c, and e), and Base+Mn alloy (b, d, and f). (a, b) EBSD inverse pole figure (IPF) maps, (c, d) SEM images of the fish-scale structure of melt pools, (e, f) SEM images of enlarged melt pools showing fine Si-rich networks (bright) and α-Al cells (dark) in the melt pool center.

Figure 3-4a and 4b present bright-field TEM images showing the detailed microstructure of both alloys in the F condition. Figure 3-4a shows a bright aluminum matrix encircled by a dark Si-rich network in the Base alloy. In contrast, a number of Si-rich nanoparticles appeared in the aluminum matrix of the Base+Mn alloy (Figure 3-4b and 3-4c), also confirmed in our recent work [36]. A key distinction between the two alloys is the presence of a high number density of Si-rich nanoparticles in the Base+Mn alloy, which were rarely found in the Base alloy. The Si-rich nanoparticles in the Base+Mn alloy (Figure 3-4c) are nearly spherical, with an average size (diameter) of 4.76 ± 1.07 nm and a volume fraction of 0.19%.

Another distinction lies in the Si-rich networks where α-Al(Mn,Fe)Si intermetallic particles (black spots) are present within the network in the Base+Mn alloy (Figure 3-4b and 3-4e). In the Base alloy, the Si-rich network was composed predominantly of Si, as shown in the TEM-EDS spectrum (Figure 3-4d). In the Si-rich network of the Base+Mn alloy, however, TEM-EDS analysis (Figure 3-4f) revealed that the particles are composed of Si, Mn, and Fe, indicating they are α-Al(Mn,Fe)Si intermetallic particles according to their chemical composition. This suggests that during solidification in the SLM process, these alloying elements (Mn and Fe) co-solidified with Si and formed α-Al(Mn,Fe)Si intermetallics in the Si-rich network. The presence of a number of such particles can reinforce the Si-rich network and hence improve the alloy strength [44]. As a result, the microstructure of the Si-rich network transitions from a singular configuration in the Base alloy (almost pure eutectic Si) to a complex multimodal structure in the Base+Mn alloy.

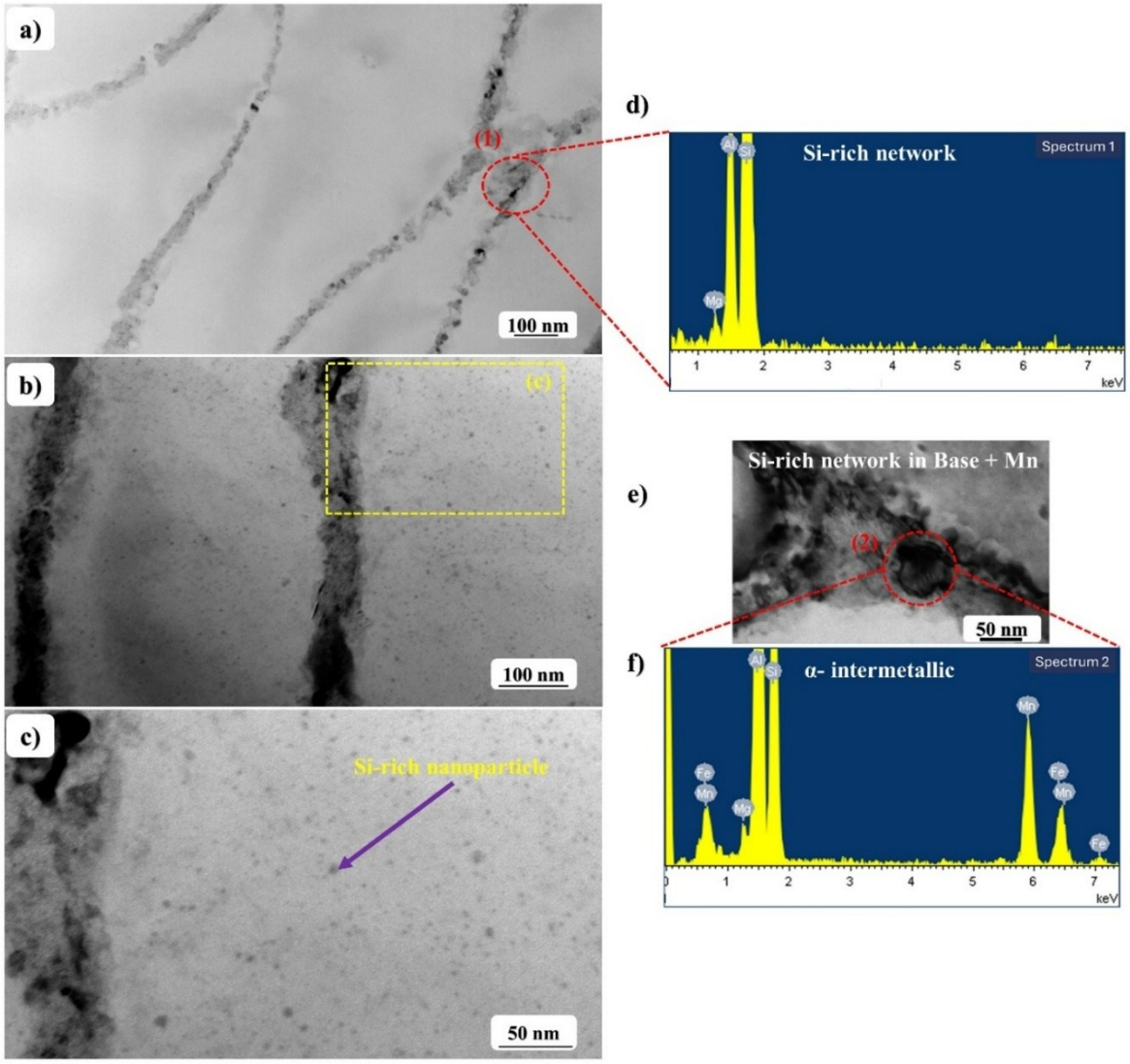

Figure 3-4: Bright-field TEM micrographs of the a) Base and b) Base+Mn alloys in the F condition, c) Si-rich nanoparticles in the Al matrix of the Base+Mn alloy, d) TEM-EDS spectrum of the Si-rich network in the Base alloy, e) enlarged TEM micrograph of α-Al(Mn,Fe)Si intermetallic particle inside the Si-rich network in the Base+Mn alloy, f) TEM-EDS spectrum of the α-Al(Mn,Fe)Si intermetallic particle in Fig. 3-4e.

3.3.3 Microstructure and microhardness evolution during T5 and T6 treatments

The microstructures after T5 and T6 treatments exhibited major changes compared to the F condition. Figure 3-5 presents a comparison of microstructural changes in the T5 and T6 conditions for both the Base and Base+Mn alloys. The SEM images in Figure 3-5a and 3-5b reveal that the Si-rich networks and aluminum cells of both alloys remained mostly unchanged after the direct aging (T5) when compared to the F condition (Figure 3-3e and 3-3f), except that some precipitates appeared inside the aluminum cells (see the insets of Figure 3-5a and 3-5b). These observations align with recent studies that have also reported the existence of nanoprecipitates in the AlSi10Mg alloy after T5 heat treatment [14, 36, 45]. As mentioned in Section 3.1, the mechanical properties after aging to T5 were significantly improved compared to the F condition. Therefore, the precipitation microstructures in the aluminum matrix were investigated in detail using TEM.

When the SLM samples of both alloys were subjected to the T6 treatment, their microstructures exhibited significant changes compared to the F and T5 conditions. Figure 3-5c and 3-5d show a breakdown of the Si-rich networks and substantial coarsening of the Si particles in both alloys. The SEM-EDS analyses confirmed that the broken and rounded particles were Si particles in both alloys (Figure 3-5e and 3-5f). The average size of those rounded particles was 0.9±0.3 μm. In addition, the high-temperature T6 solution treatment induced the formation of a needle/rod-shaped Fe-rich intermetallic phase in the Al matrix of the Base alloy (Figure 3-5c). SEM-EDS analysis (Figure 3-5g) indicated that these are β-AlFeSi intermetallic particles. Previous studies have also reported the appearance of this phase following SLM in AlSi10Mg alloys [39, 46]. In contrast, such β-AlFeSi intermetallic

particles were not observed in the Base+Mn alloy. Instead, many small and spherical particles were observed in the aluminum matrix in addition to coarse and rounded Si particles. According to the SEM-EDS result (Figure 3-5h) these particles were identified as α-Al(Mn,Fe)Si dispersoids. The dimensions, morphology, and elemental composition of these dispersoids are consistent with the results reported in the literature [35]. The presence of a large number of those dispersoids could be the main reason for the higher YS of the Base+Mn alloy compared to that of the Base alloy in the T6 condition, which is studied in further detail using TEM [47].

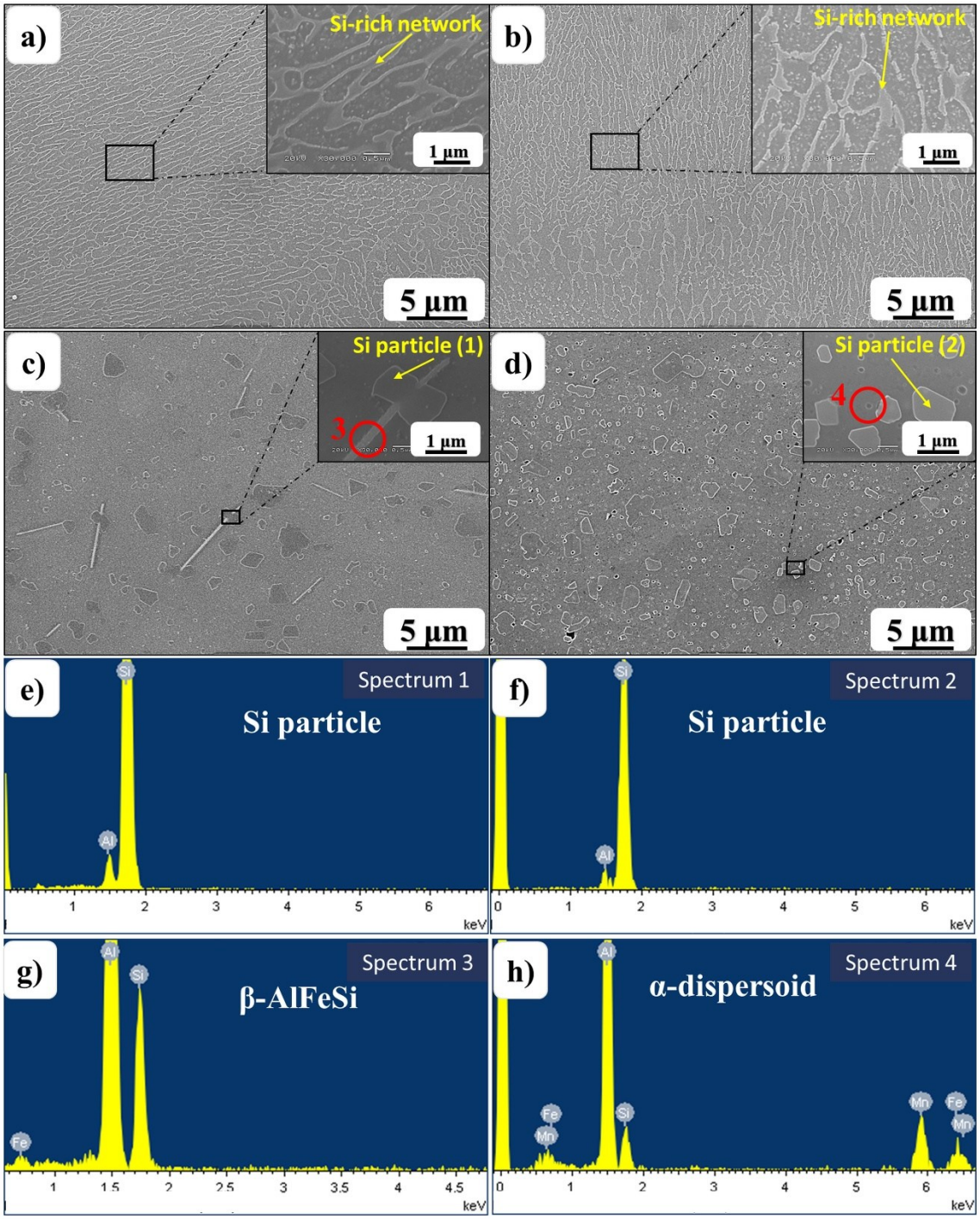

Figure 3-5: SEM images and SEM-EDS results taken from the samples parallel to the build direction: a) Base alloy in T5; b) Base+Mn in T5; c) Base in T6; d) Base+Mn in T6. EDS point results of particles taken from c and d: e) Spectrum 1 of Si particle taken from Fig. 3-5c; f) Spectrum 2 of Si particle taken from Fig. 3-5d; g) Spectrum 3 of β-AlFeSi intermetallic particle taken from Fig. 3-5c; h) Spectrum 4 of α-Al(Mn,Fe)Si dispersoid taken from Fig. 3-5d.

Figure 3-6a and 3-6b show the typical precipitation microstructures of both alloys in the T5 condition. The Si-rich network structure remained relatively unchanged compared to the F condition (Figure 3-4). Inside the aluminum cells, a number of nano-sized precipitate particles can be clearly observed. The rapid solidification during SLM resulted in a supersaturated solid solution. Subsequent direct aging (T5) therefore promoted the precipitation of nanoparticles in the aluminum matrix. In the Base alloy, the number density of nanoprecipitates was quite low (Figure 3-6a). The majority of the nanoprecipitates were granular Si nanoparticles as identified through TEM-EDS analysis (result not shown here). This type of nanoparticle had an average size of 22.5 nm and a number density of 773 μm^{-3}. In addition, a few needle-like particles were observed, and were identified as MgSi-based precipitates according to TEM-EDS results. In the Base+Mn alloy, two distinct types of nanoprecipitates can be more clearly observed, and the total number density of nanoprecipitates was greatly increased compared to that in the Base alloy (Figure 3-6b). The first type is the granular Si-rich nanoparticles that had an average size of 15.8 nm, a number density of 1900 μm^{-3}, and a volume fraction of 0.4%. Compared to the F condition, both the size and the volume fraction of the Si-rich nanoparticles were remarkably increased. The second type is the needle-like MgSi-based precipitates with a clear orientation in the aluminum matrix, averaging 78.38 nm in length with a number density of 2850 μm^{-3}. Based on their size, shape, and composition, it is suggested that these are most likely β′/β″-MgSi precipitates, which contribute to the alloy strength [48]. The higher Mg content in the Base+Mn alloy compared to the Base alloy explains the presence of a much higher number density of this type of precipitates in the Base+Mn alloy.

Figure 3-6c and 3-6d present the precipitation microstructures of both alloys in the T6 condition. Notably, the continuous Si-rich network has completely vanished, and coarse, isolated Si particles were observed in both alloys. In the Base alloy, a large number of needle-like precipitates were observed in the aluminum matrix (Figure 3-6c), which are identified as β′/β″-MgSi precipitates according to their size and morphology [35, 48]. The length of these nanoprecipitates was 50 nm with a number density of 43000 μm^{-3} in the Base alloy. In the Base+Mn alloy, there were also many needle-like β′/β″-MgSi precipitates in the matrix (see the inset of Figure 3-6d) with an average length of 45 nm and number density of 48000 μm^{-3}. Furthermore, a number of spherical α-Al(Mn,Fe)Si dispersoids had also precipitated in the matrix because of the Mn in the alloy (Figure 3-6d). These dispersoids have an average diameter of 97 nm and a number density of 46 μm^{-3}, which can provide complementary strengthening to the material in the T6 condition. It is reported that α-Al(Mn,Fe)Si dispersoids formed via the decomposition of the supersaturated solid solution during the T6 heat treatment [49, 50].

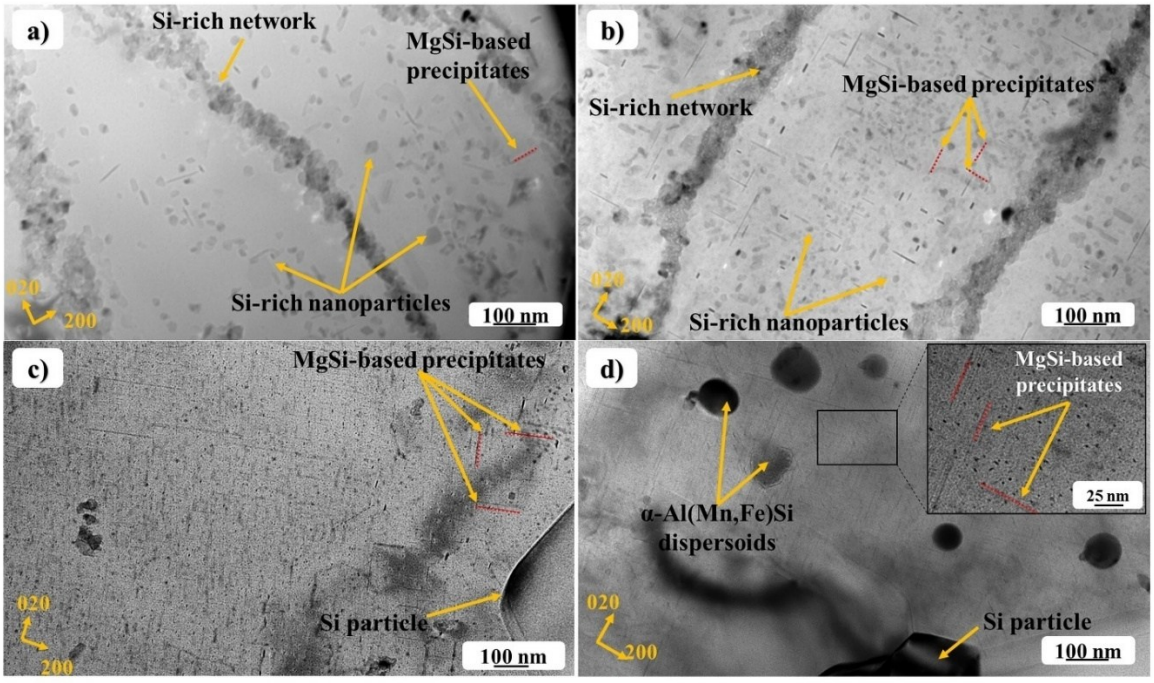

Figure 3-6: Bright-field TEM micrographs showing the precipitation microstructures: a) Base alloy in T5 condition; b) Base+Mn alloy in T5 condition; c) Base alloy in T6 condition; d) Base+Mn alloy in T6 condition.

A continuous heating procedure from room temperature to 530 °C, simulating the ramp-up to solution treatment, was employed to explore the microstructural and microhardness changes as the temperature increased. Figure 3-7 illustrates the microhardness measurements and the corresponding microstructures in both the Base and Base+Mn alloys. Before heating (i.e., in the F condition), the microhardness of the Base+Mn alloy was approximately 10 HV higher than that of the Base alloy. The microhardness and microstructural changes during heating can be divided into three distinct sections. The first section (below 200 °C) is characterized by precipitation at low temperature, which enhances the microhardness of both alloys. In this regime, both alloys show a microstructure similar to the T5 condition (Figure 3-5a and 3-6a, and Figure 3-5b and 3-6b). Upon reaching 200 °C, the microhardness of the Base alloy increased by about 10 HV, while the Base+Mn alloy

exhibited a more pronounced increase of approximately 20 HV. Such increases can be attributed to the precipitation of Si-rich and MgSi-based nanoprecipitates in the aluminum matrix, with the Base+Mn alloy exhibiting a much higher number density of both nanoprecipitates compared to the Base alloy, as illustrated in Figure 3-6a and 3-6b.

Beyond 200 °C, the microhardness of both alloys begins to decrease, accompanied by the dissolution of precipitates and a partial break-up of the Si-rich network, as evidenced by microstructural observations in this work and in the literature [29, 36]. This marks the second section, where the microhardness of both alloys continuously decreases and the microhardness levels are close to each other. In the third section, starting at 375 °C, the microhardness of both alloys continues to slowly decrease because of the full break-up of the Si-rich network and Ostwald ripening of isolated Si particles [29, 51, 52]. However, the Base+Mn alloy again shows a higher hardness than the Base alloy. Notably, the Base+Mn alloy exhibits a second peak at approximately 375 °C, which results from the precipitation of α-Al(Mn,Fe)Si dispersoids [49]. The greater microhardness of the Base+Mn alloy in this section can be attributed to the presence of thermally stable α-Al(Mn,Fe)Si dispersoids, as shown in Figure 3-5 and Figure 3-6.

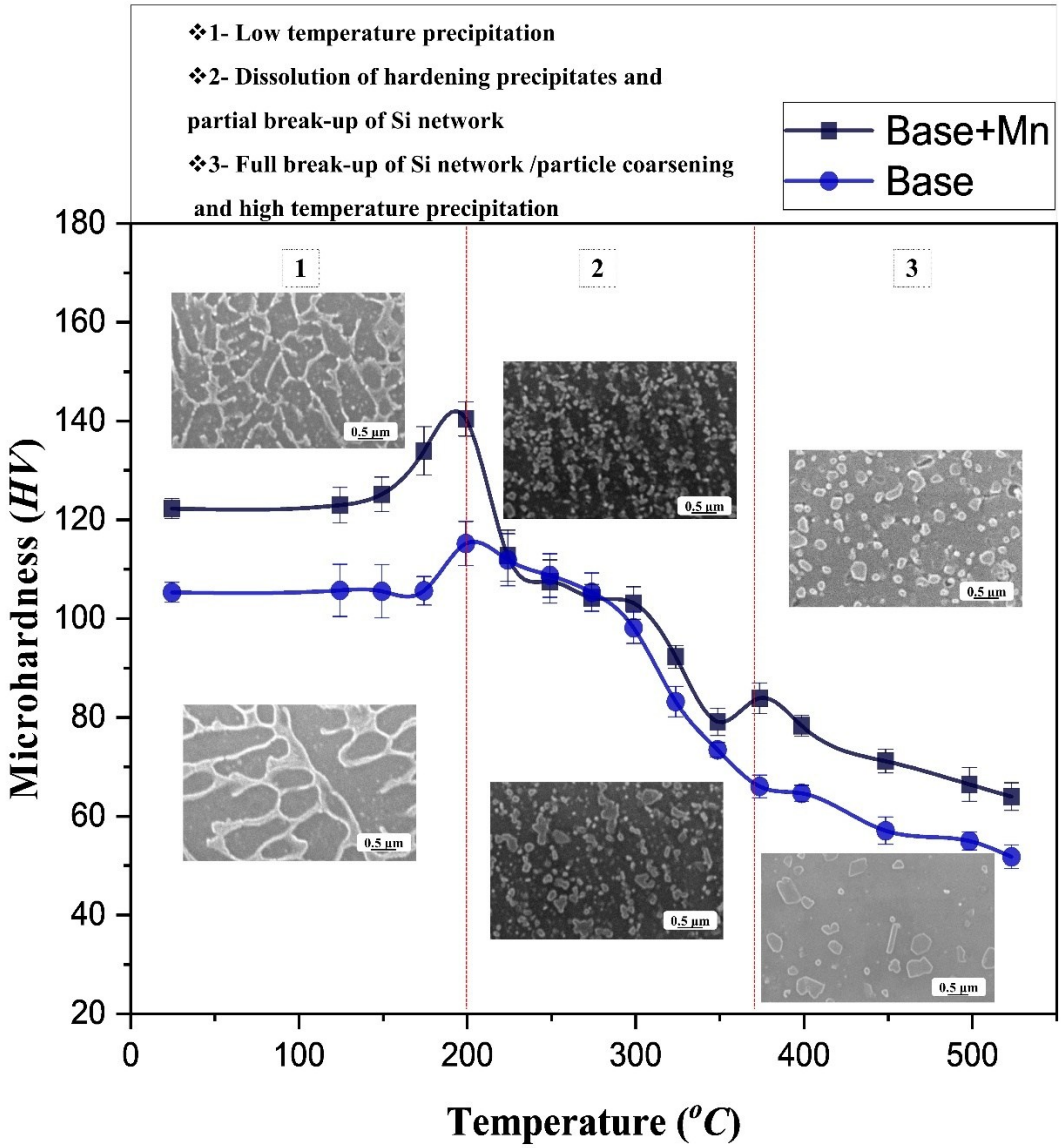

Figure 3-7: Microhardness measurements and associated microstructures during continuous heating at a heating rate of 50 °C/h for the Base and Base+Mn alloys (similar to the T6 solution treatment).

3.3.4 APT results in T5 condition

As illustrated in Figure 3-2, the best tensile strengths for SLM samples of both alloys were achieved in the T5 condition. Furthermore, the most significant differences in strengths between the two alloys were also observed in the T5 condition. Therefore, atom probe tomography (APT) analysis was conducted to investigate: (i) the Si-rich network, (ii) Si-rich

nanoparticles, and (iii) MgSi-based precipitates. Three-dimensional reconstructions of representative data volumes for the Base and Base+Mn alloys are shown in Figure 3-8a and Figure 3-9a, respectively.

In both alloys, Si-rich particles appear as a plate-like phase that solidifies within and between the aluminum cells, consistent with TEM observations (Figure 3-6a and 3-6b). The proximity histogram from the Base alloy in Figure 3-8b shows that the plate-like particles have a high Si concentration and are deficient in Al, but there is a trace of Mg. It is not clear from this data volume whether these particles come from within the cells or from the network boundary. However, in Figure 3-9a for the Base+Mn alloy, it appears to be the Si-rich network, which has a somewhat similar plate-like morphology and a similar chemical composition (Figure 3-9b). However, in addition to Mg, there are also traces of Mn and Fe segregated in the network, as shown in the inset of Figure 3-9b. Furthermore, the proximity concentration profile of a separate particle that is located in the Si-rich network (outlined with an orange dashed line in Figure 3-9a) reveals enrichment of Mn (Figure 3-9c), suggesting the presence of α-Al(Mn,Fe)Si intermetallic particles inside the Si-rich network. These particles, observed exclusively in the Base+Mn alloy, are evidence that the Mn in the alloy promotes the formation of α-Al(Mn,Fe)Si in the Si-rich network, which can strengthen the Si-rich network and enhance the mechanical properties of the Base+Mn alloy compared to the Base alloy. The nonequilibrium conditions can account for the variations in the chemical composition of these particles, particularly in the Fe content.

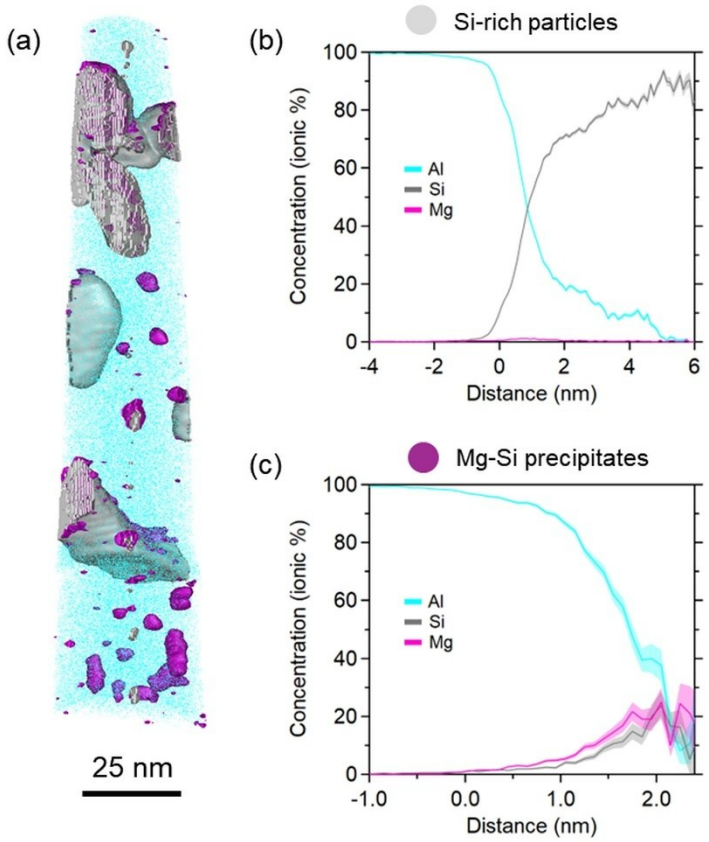

Figure 3-8: a) APT reconstruction of the Base alloy in the T5 condition. Proximity histograms are computed from the iso-concentration surfaces that identify b) Si-rich particles, and c) Mg-Si precipitates.

In contrast to the Base alloy, the APT results from the Base+Mn alloy in the T5 condition also reveal a high number density of Si-rich nanoparticles with spherical morphology and a diameter of about 5−10 nm (Figure 3-9a). The local chemical composition of these Si-rich nanoparticles is 67-75 at.% Si and 22-30 at.% Al, along with small amounts of Mn, Mg, and Fe (~ 0.5−1 at.% of each) that are noticeably higher than in the matrix (Figure 3-9d). Interestingly, there is a marked segregation of Fe (~4 at.%) at the interface, and the Si concentration decreases slightly towards the center of these small spherical Si-rich nanoparticles.

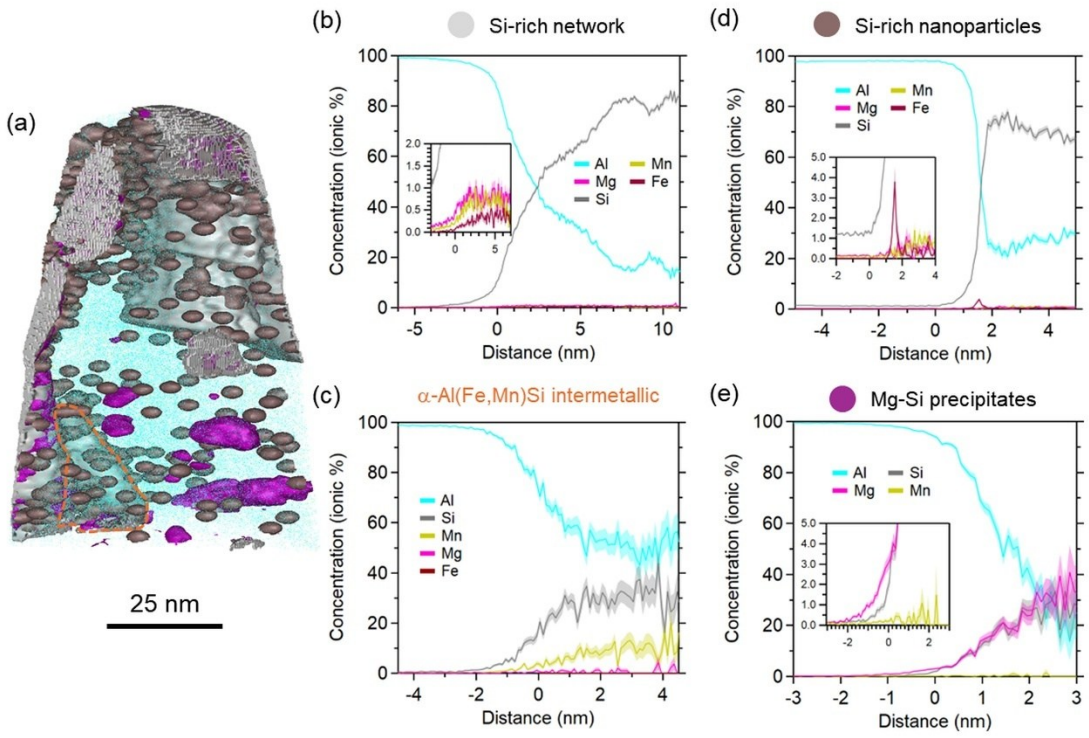

Figure 3-9: a) APT reconstructions of the Base+Mn alloy in the T5 condition. Proximity histograms are computed from the various isosurfaces that identify the b) Si-rich network, c) an α-Al(Fe,Mn)Si intermetallic particle, d) Si-rich nanoparticles, and e) Mg-Si precipitates.

Lastly, MgSi-based precipitates were observed in both the Base and Base+Mn alloys, as shown in Figure 3-8a and Figure 3-9a, along with the corresponding proximity histograms in Figure 3-8c and Figure 3-9e. These MgSi-based precipitates exhibit only slightly elongated morphologies (~5-20 nm length) and are probably on the lower end of the β″ particle size distribution range compared to the larger needle-like precipitates (β′/β″) observed in both alloys by TEM (Figure 3-6a and 3-6b). The proximity histograms reveal that these smaller precipitates have Mg/Si ratios of close to 1. Interestingly, Figure 3-9e

shows that these Mg-Si precipitates also contain ~0.5 at% Mn in the Base+Mn alloy (as for the Si-rich nanoparticles in Figure 3-9d).

3.3.5 Fracture analysis of tensile samples

Understanding the mechanisms of damage and their relationship to the microstructure is important in SLM-processed aluminum alloys, particularly for those demonstrating lower ductility compared with wrought materials. Figure 3-10a and 3-10b compare the fracture surfaces and nearby damage zones for the Base and Base+Mn alloys (respectively) in the F condition. Both alloys reveal cleavage planes along the fracture surface, indicating some signs of brittle fracture mode in this condition. This is consistent with the tensile test results (Figure 3-2) in which neither alloy exhibited necking prior to fracture, indicating brittle fracture behavior in the F condition. At higher magnification (inset images in Figure 3-10a and 3-10b), both alloys exhibit narrow, lamellar surfaces. This morphology of the cleavage planes resembles that of the Si-rich network, suggesting that fracture in both alloys is associated with this network [53]. The Si-rich network in both alloys is interconnected, and it does not show much ductility. It has been reported that once the crack initiates, the load-bearing effect of this network transfers to the matrix, and fracture occurs quickly [6, 54]. The interconnected network results in crack formation along the Si-rich network in the F condition for both alloys. Owing to the fine network and small damage spacing, cracks propagate quickly, contributing to a somewhat brittle fracture in the F condition, though still with a good 10-12% elongation (Figure 3-2).

Figure 3-10c and 3-10d show the fracture surfaces and damage zones of the Base and Base+Mn alloys in the T5 condition. Like the F condition, the fracture mechanism in the T5

condition is a somewhat brittle fracture, characterized by cleavage planes. The damage zones are predominantly located within the Si-rich network, as shown in the labelled inset images, whilst the high-magnification inset images reveal traces of the network in the fracture planes of both alloys. Overall, the brittle nature of the Si-rich network facilitates crack initiation and propagation, as in the F condition [54, 55], but the elongation is broadly similar despite the higher strength.

Figure 3-10e and 3-10f demonstrate a notable transition towards a classic ductile fracture mechanism for both the Base and Base+Mn alloys in the T6 condition, even though the tensile elongation values are only slightly higher than those in T5 condition (Figure 3-2). This shift is characterized by the presence of uniformly distributed equiaxed dimples, averaging approximately 2 μm in diameter, across the fracture surfaces of both alloys. The Si particles present in both alloys serve as fracture initiation sites during tensile testing, as shown with yellow arrows. The accumulation of dislocations around these silicon particles can lead to crack formation, a behavior previously reported for the Al-Si alloys [56, 57]. Additionally, the brittle and needle-like β-AlFeSi intermetallic phase in the Base alloy acts as a site for crack initiation during tensile testing (purple arrow in Figure 3-10e) [58]. In contrast, the rounded α-Al(Mn,Fe)Si dispersoids in the Base+Mn alloy show resistance to crack formation [59, 60].

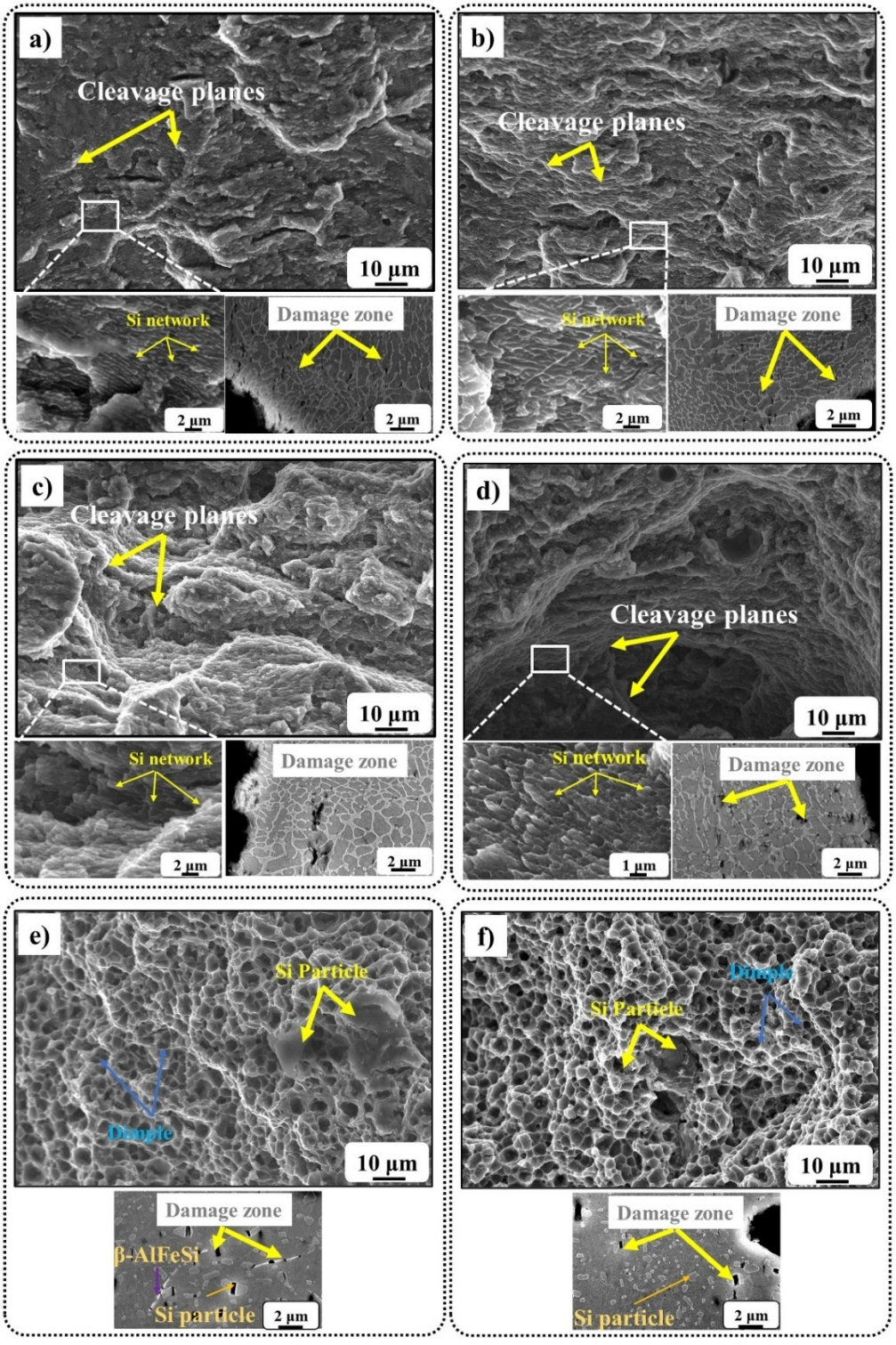

Figure 3-10: SEM images of the fracture surfaces and damage zones near the fracture surface (after polishing and etching) for the Base alloy in the a) F, c) T5, and e) T6 conditions; and similarly for the Base+Mn alloy in the b) F, d) T5, and f) T6 conditions.

3.4 Discussion

3.4.1 Effect of Mn on Si-rich network

Although SLM involves non-equilibrium processes, the phase diagram remains a valuable tool for understanding the potential phases that may form upon heat treatment after SLM. Thermodynamic equilibrium calculations for the Base and Base+Mn alloys were conducted using Thermo-Calc software (version 2023 with the TCAL7 database). Figure 3-11a and 3-11b present the stable phases in the Base and Base+Mn alloys as a function of temperature. The liquidus is located at approximately 600 °C for both alloys. Upon cooling, the solidification path for the Base alloy starts with α-Al, followed by the Si, β-AlFeSi, $Al_8FeMg_3Si_6$, and Mg_2Si phases, which are stable over various temperature ranges as shown in Figure 3-11a (equilibrium conditions). For the Base+Mn alloy, depending on the cooling conditions, the α-Al(Mn,Fe)Si phase can solidify prior to and/or together with α-Al and Si, followed by Mg_2Si. This alloy contains more Mg_2Si than the base alloy in Figure 3-11, implying that it should also contain more metastable Mg-Si precursor precipitates than the Base alloy.

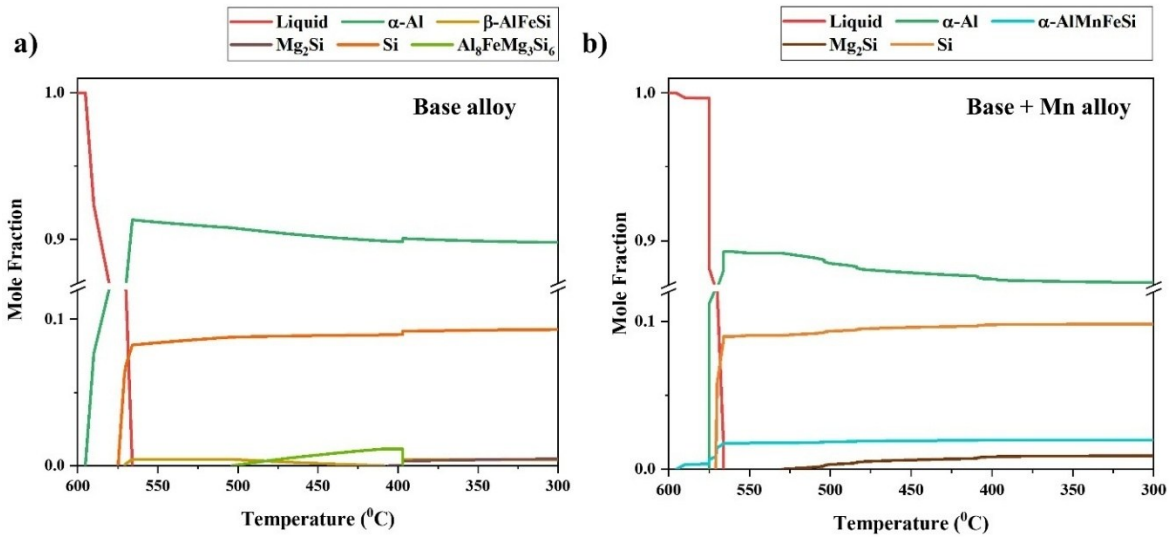

Figure 3-11: Equilibrium phase diagrams for the a) Base alloy and b) Base+Mn alloy, showing the stable phases at each temperature.

Both here and in previous studies, it has been shown that the rapid solidification of SLM-fabricated AlSi10Mg alloys, combined with a large thermal gradient, leads to the formation of a cellular structure [6, 14, 42]. The formation of the cellular α-Al phase is accompanied by micro-segregation of Si and other alloying elements, such as Mg and Fe, in the intercellular regions [30, 61-63]. The strong load-bearing effect of the Si-rich network and its role in alloy strengthening have been proven [6], and it is plastically deformed by twinning and the pile-up of dislocations [64]. In the Base+Mn alloy, Mn also segregates in the intercellular structure of the Si-rich network in the F condition, as shown in Figure 3-4f, and it remains there in the T5 condition (Figure 3-5, 3-6, and 3-9). Figure 3-12 further confirms these findings with TEM-EDS mapping results that highlight the segregation of Mn and Fe in specific regions of the Si-rich network to form α-Al(Mn,Fe)Si intermetallic particles. This is also consistent with the equilibrium phase diagram of the Base+Mn alloy (Figure 3-11b), which predicts the formation of the α-Al(Mn,Fe)Si intermetallic phase. The presence of this phase within the Si-rich network introduces an additional strengthening

contribution for the Base+Mn alloy compared to the Base alloy, providing additional obstacles to dislocation motion in both the F and T5 conditions.

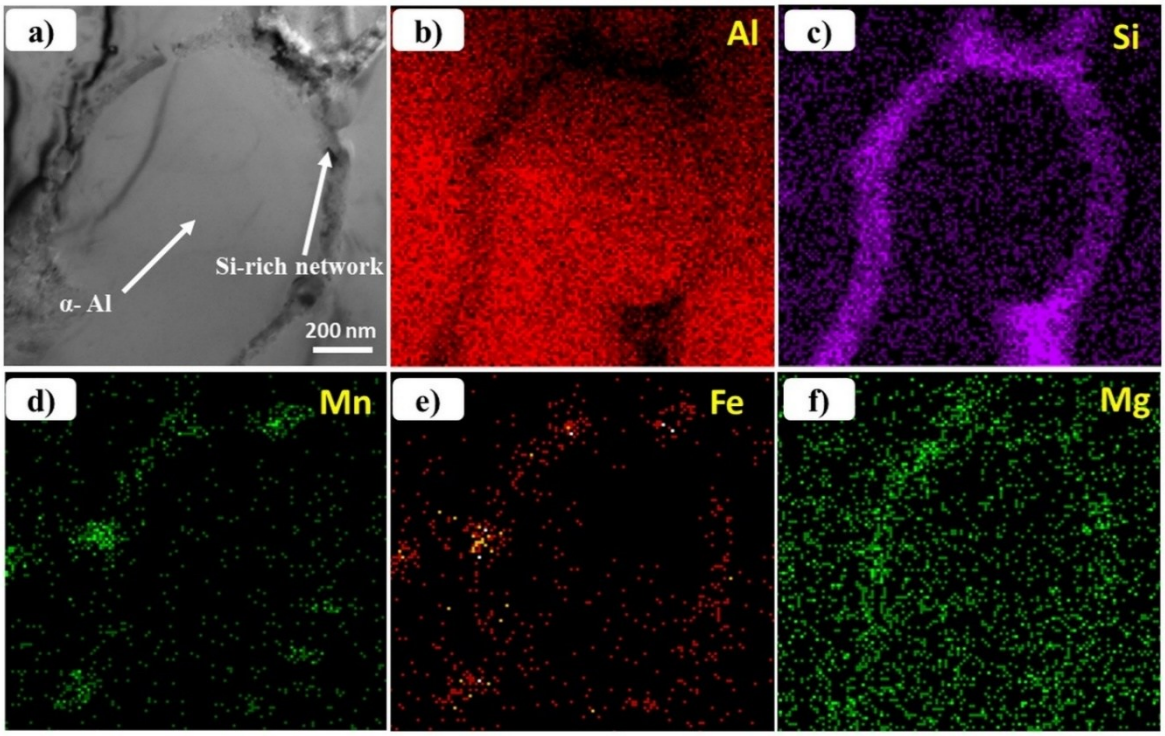

Figure 3-12: a) Bright-field TEM image showing the Si-rich network in the Base+Mn alloy in the T5 condition; b-f) TEM-EDS elemental mapping for Al, Si, Mn, Fe, and Mg, respectively.

Figure 3-13 depicts the strain hardening rate versus true strain curves in the stable region of deformation for the Base and Base+Mn alloys in the F condition. Interaction between dislocations and the Si-rich network has a significant effect on strain hardening [65]. The rate of strain hardening ($\theta = d\sigma/d\varepsilon$) in the Base+Mn alloy was higher than in the Base alloy. In the Base+Mn alloy, saturation of strain hardening (the drop in the hardening value) occurred at higher values of plastic strain. This indicates that the modified Si-rich network (including the presence of α-AlMnFeSi intermetallic particles) has a greater effect on strain hardening compared to the Base alloy.

Figure 3-14 presents a schematic representation of this strengthening mechanism, highlighting the role of Mn in enhancing the yield strength of the Base+Mn alloy in the F and T5 conditions. The presence of Mn promotes the formation of an α-Al(Mn,Fe)Si intermetallic phase, which increases the stress required to initiate dislocation pile-up within the network, compared to the Base alloy. This schematic illustrates how the incorporation of α-Al(Mn,Fe)Si intermetallic particles strengthens the Si-rich network by providing strong barriers to dislocation movement in all cellular structures, thereby improving its resistance to deformation under applied stress.

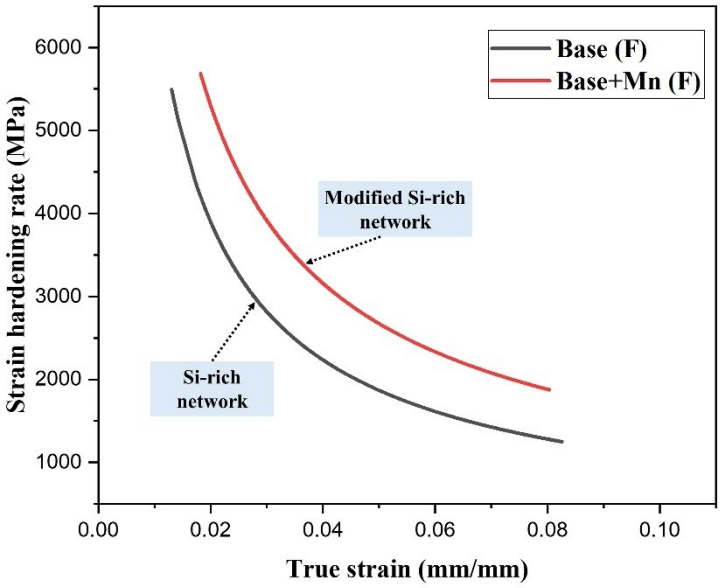

Figure 3-13: The strain hardening rate (θ) vs true strain (ε) curves for the Base and Base+Mn alloys in the F condition.

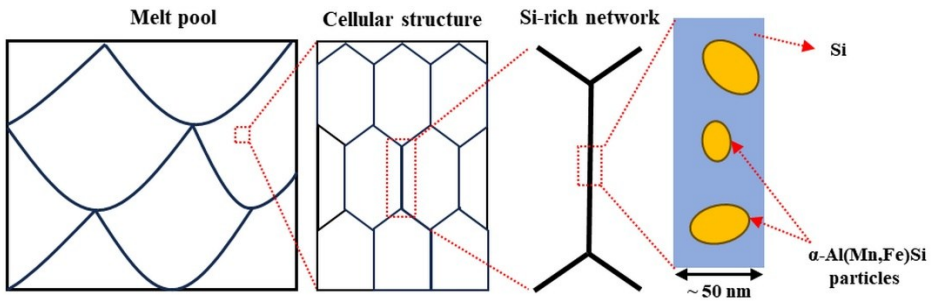

Figure 3-14: Schematic illustration of the modified Si-rich network in the Base+Mn alloy in the F and T5 conditions.

3.4.2 Effect of Mn on precipitation strengthening

It is crucial to highlight the significant impact of the high cooling rate during SLM, which substantially increases the Si supersaturation in the aluminum matrix [36]. Moreover, while a significant amount of Mn is found at cell boundaries, as shown in Figure 3-12, a fraction remains in solid solution within the cells and can improve the mechanical properties by solid solution strengthening. The increased level of Si supersaturation in both alloys promotes precipitation via direct aging. The TEM and APT observations confirm that the Base+Mn alloy exhibits a higher number density of Si-rich nanoparticles than the Base alloy in both the F and T5 conditions, as shown in Figures 4, 6(a, b), 8, and 9, thereby enhancing the strength (Figure 3-2). It also exhibits a higher number density of MgSi-based precipitates in both the T5 and T6 conditions.

The role of Mn in the matrix is crucial for distinguishing the number density of Si-rich nanoparticles in both the F and T5 conditions. Figure 3-7 reveals that the hardness of the Base+Mn alloy in the F condition exceeds that of the Base alloy. The difference in the

hardness between the two alloys became more pronounced around the peak hardness at 200 °C, where the Si-rich nanoparticles and the Mg-Si precipitates significantly enhanced the hardness. Using the Orowan bypass equation for Si-rich nanoparticle, it is predicted that the Base+Mn alloy experiences significantly higher precipitation hardening (by approximately 30 MPa YS) than the Base alloy, owing to the presence of finer and more numerous Si-rich nanoparticles. In addition, a higher amount of Mg in the Base+Mn alloy (Table 3-1) and hence a higher number density of MgSi-based nanoprecipitates (as it is predicted in Figure 3-11) can also provide a supplementary strengthening contribution in this condition. The APT result shown in Figure 3-9e indicates the presence of Mn within the core of the precipitates, suggesting that Mn also contributes to the precipitation process. This additional strengthening in Mn+Base alloy was calculated to be 30 MPa.

To explain the effect of Mn on Si-rich nanoparticle precipitation within the Base+Mn alloy, especially in the T5 condition, the enthalpy of mixing can be considered. Since Mn atoms have a strong binding energy with Si atoms [66], the addition of Mn is more effective in refining the cluster distribution, which results in a higher number density of smaller precipitates and hence a greater precipitation hardening response. The enthalpy of mixing is more negative for Mn-Si (-45 kJ/mol) compared to Al-Si (-19 kJ/mol) alloy systems [67]. This suggests that Mn in the matrix lowers the activation energy for the precipitation of Si-rich nanoparticles by acting as effective heterogeneous nucleation sites owing to the strong interaction between Mn and Si atoms. It has been reported that the yield strength of an Al–Mn–Si ternary alloy exceeds the prediction based on multi-element hardening models that assume no interaction among alloying elements. Researchers demonstrated that the Si–Mn interactions are particularly strong and can significantly contribute to the clustering process

[68]. Peng et al. [69] demonstrated a strong binding energy between Si and Mn, as determined through density functional theory (DFT) calculations. The APT results confirm the presence of Mn atoms within the Si-rich nanoparticles in the Base+Mn alloy (Figure 3-9d). Similar effects have been observed with La addition in Al-Mg-Si alloys [70]. Additionally, the large atomic radius of Mn [71] causes Mn to bind more favorably with quenched-in vacancies in the matrix. As Mn atoms combine with vacancies, it tends to mitigate the lattice strain caused by solute atoms in the matrix [72]. This could help to promote Si-rich cluster formation around Mn atoms in the matrix during low-temperature aging. These factors are likely to contribute to the higher number density of Si-rich nanoparticles observed in the Base+Mn alloy, as shown schematically in Figure 3-15. They likely also can contribute to the higher number density of fine Mn-containing MgSi precipitates in the Base+Mn alloy in the T5 condition (Figure 3-9a and 3-9e), which could have nucleated similarly from Mn-Si-vacancy clusters.

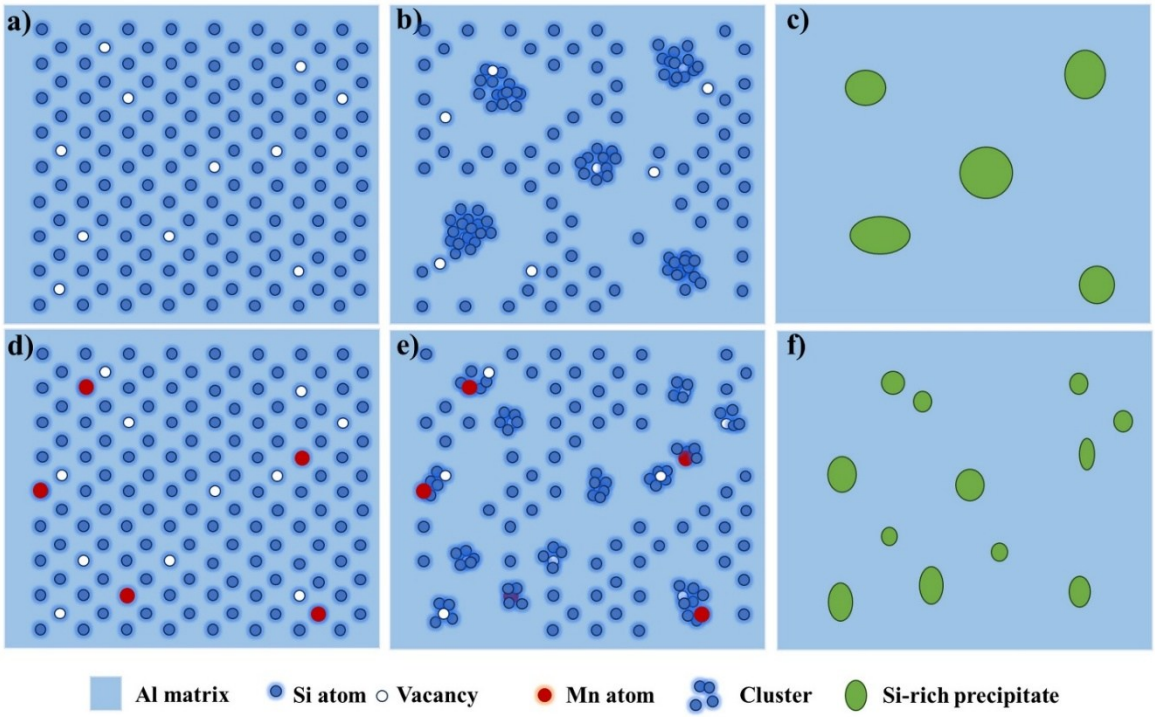

Figure 3-15: Schematic diagram of precipitation: a-c) Base alloy; d-f) Base+Mn alloy. a,d) Initial solid solution conditions after SLM; b,e) transition conditions where clusters are formed during aging; c,f) characteristics of Si-rich nanoparticles after aging.

3.4.3 Effect of Mn in the T6 condition

The presence of Fe in aluminum alloys is typically viewed as detrimental because of its association with impurities and brittle intermetallic compounds. The effects of the β-Al_5FeSi phase on the mechanical properties of high-silicon aluminum alloys have been investigated [73-75]. Research has indicated that the introduction of Fe correctors such as Mn, can prevent the formation of this brittle phase [76]. In the T6 heat treatment, both the Base and Base+Mn alloys were subjected to a high-temperature solution treatment at 530 °C, where the β-Al_5FeSi intermetallic phase was formed in the base alloy. The β-Al_5FeSi particles exhibit a needle-like morphology (Figure 3-5c), which acts as a site of weakness during tensile testing (Figure 3-10e) and can adversely affect the mechanical properties. As a result, the Base alloy

did not exhibit a higher elongation than the Base+Mn alloy despite its significantly lower T6 strength (Figure 3-2).

Owing to the Mn addition, the needle-like β-Al_5FeSi phase was completely eliminated in the Base+Mn alloy (Figure 3-5). Instead, a number of spherical α-Al(Mn,Fe)Si dispersoids were formed and uniformly distributed in the aluminum matrix (Figure 3-6d), which provides complementary strengthening to the Base+Mn alloy in addition to the MgSi-based nanoprecipitates, which are the main strengthening phase in the T6 condition. The YS increment induced by the presence of α-Al(Mn,Fe)Si dispersoids can be estimated by the Orowan bypass mechanism, as described by [77]:

$$\Delta\sigma_{Orowan} = \frac{MGb}{l} \qquad (1)$$

where G is the shear modulus (27.2 GPa), M is the Taylor factor (3.02), b is Burgers vector for dislocations in the aluminum matrix (0.286 nm), and l is the precipitation spacing in the glide plane, which can be expressed by Eq. 2:

$$l = \frac{d_{pre}}{2}\sqrt{\frac{2\pi}{3f_v}} \qquad (2)$$

where d_{pre} is the diameter of the particles and f_v is the volume fraction of the dispersoids. The α-Al(Mn,Fe)Si dispersoids exhibited an average diameter of 97 nm and a volume fraction of 2.3%.

Calculation based on the above indicates that α-Al(Mn,Fe)Si dispersoids provide an additional YS contribution of 50 MPa. Therefore, the increased yield strength of the Base+Mn alloy relative to the Base alloy in the T6 condition (Figure 3-2) can be largely

attributed to this contribution from the α-Al(Mn,Fe)Si dispersoids, in addition to the existing strengthening contributions from the MgSi-based precipitates and Si particles.

3.5 Conclusions

1- The addition of 0.5 wt.% Mn to a standard AlSi10Mg alloy manufactured by selective laser melting considerably improved the strength while maintaining a similar elongation level. Relative to the base alloy, the Mn-modified alloy exhibited yield strength increases of 17%, 30%, and 29% in the as-manufactured (F), T5, and T6 conditions, respectively.

2- In the F and T5 conditions, the Mn-modification resulted in the formation of α-Al(Mn,Fe)Si intermetallic particles inside the Si-rich eutectic network, which reinforced the network and improved the strength. Moreover, the presence of Mn in the matrix promoted the precipitation of a higher number density of Si-rich nanoparticles and MgSi-based precipitates, which provided significantly higher precipitation hardening than in the base alloy. Among all the heat treatment and alloy conditions studied, the Mn-modified alloy in the T5 condition achieved the highest yield and ultimate tensile strengths of 386 MPa and 532 MPa, respectively.

3- After T6 heat treatment, the Si-rich network completely disappeared and a large amount of MgSi-based precipitates were present in both alloys. The Mn-modification not only eliminated the harmful needle-like β-Al5FeSi phase in the matrix, but also promoted the formation of α-Al(Mn,Fe)Si dispersoids. The increased strength of the Mn-modified alloy relative to the base alloy in the T6 condition is largely attributed to the significant additional strengthening contribution from these dispersoids.

References

[1] B. Blakey-Milner, P. Gradl, G. Snedden, M. Brooks, J. Pitot, E. Lopez, M. Leary, F. Berto, A. du Plessis, Metal additive manufacturing in aerospace: A review, Materials & Design 209 (2021) 110008.https://doi.org/10.1016/j.matdes.2021.110008

[2] E.M. Sefene, State-of-the-art of selective laser melting process: A comprehensive review, Journal of Manufacturing Systems 63 (2022) 250-274.https://doi.org/10.1016/j.jmsy.2022.04.002

[3] P.A. Rometsch, Y. Zhu, X. Wu, A. Huang, Review of high-strength aluminium alloys for additive manufacturing by laser powder bed fusion, Materials & Design 219 (2022) 110779.https://doi.org/10.1016/j.matdes.2022.110779

[4] J. Zhang, B. Song, Q. Wei, D. Bourell, Y. Shi, A review of selective laser melting of aluminum alloys: Processing, microstructure, property and developing trends, Journal of Materials Science & Technology 35(2) (2019) 270-284.https://doi.org/10.1016/j.jmst.2018.09.004

[5] I.M. Kusoglu, B. Gökce, S. Barcikowski, Research trends in laser powder bed fusion of Al alloys within the last decade, Additive Manufacturing 36 (2020) 101489.https://doi.org/10.1016/j.addma.2020.101489

[6] L. Zhao, L. Song, J.G. Santos Macías, Y. Zhu, M. Huang, A. Simar, Z. Li, Review on the correlation between microstructure and mechanical performance for laser powder bed fusion AlSi10Mg, Additive Manufacturing 56 (2022).https://doi.org/10.1016/j.addma.2022.102914

[7] E.O. Olakanmi, R.F. Cochrane, K.W. Dalgarno, A review on selective laser sintering/melting (SLS/SLM) of aluminium alloy powders: Processing, microstructure, and properties, Progress in Materials Science 74 (2015) 401-477.https://doi.org/10.1016/j.pmatsci.2015.03.002

[8] C.C. Roth, T. Tancogne-Dejean, D. Mohr, Plasticity and fracture of cast and SLM AlSi10Mg: High-throughput testing and modeling, Additive Manufacturing 43 (2021) 101998.https://doi.org/10.1016/j.addma.2021.101998

[9] N. Limbasiya, A. Jain, H. Soni, V. Wankhede, G. Krolczyk, P. Sahlot, A comprehensive review on the effect of process parameters and post-process treatments on microstructure and mechanical properties of selective laser melting of AlSi10Mg, Journal of Materials Research and Technology 21 (2022) 1141-1176.https://doi.org/10.1016/j.jmrt.2022.09.092

[10] Q. Lu, B. Xu, C. Liu, Y. Peng, K. Miao, H. Wu, R. Li, X. Li, G. Fan, Interplay of heat treatment and deformation temperature on the microstructural evolution and mechanical behavior of SLM AlSi10Mg alloy, Journal of Alloys and Compounds 999 (2024) 174995.https://doi.org/10.1016/j.jallcom.2024.174995

[11] J. Wu, X.Q. Wang, W. Wang, M.M. Attallah, M.H. Loretto, Microstructure and strength of selectively laser melted AlSi10Mg, Acta Mater 117 (2016) 311-320.https://doi.org/10.1016/j.actamat.2016.07.012

[12] J. Fiocchi, A. Tuissi, C.A. Biffi, Heat treatment of aluminium alloys produced by laser powder bed fusion: A review, Materials & Design 204 (2021) 109651.https://doi.org/10.1016/j.matdes.2021.109651

[13] J. Fite, S. Eswarappa Prameela, J.A. Slotwinski, T.P. Weihs, Evolution of the microstructure and mechanical properties of additively manufactured AlSi10Mg during room temperature holds and low temperature aging, Additive Manufacturing 36 (2020).https://doi.org/10.1016/j.addma.2020.101429

[14] M. Fousová, D. Dvorský, A. Michalcová, D. Vojtěch, Changes in the microstructure and mechanical properties of additively manufactured AlSi10Mg alloy after exposure to elevated temperatures, Materials Characterization 137 (2018) 119-126.https://doi.org/10.1016/j.matchar.2018.01.028

[15] S.Y. Ahn, J. Moon, Y.T. Choi, E.S. Kim, S.G. Jeong, J.M. Park, M. Kang, H. Joo, H.S. Kim, A precipitation-hardened AlSi10Mg alloy fabricated using selective laser melting, Materials Science and Engineering: A 844 (2022) 143164.https://doi.org/10.1016/j.msea.2022.143164

[16] A. Hadadzadeh, B.S. Amirkhiz, B. Langelier, J. Li, M. Mohammadi, Microstructural consistency in the additive manufactured metallic materials: A study on the laser powder bed fusion of AlSi10Mg, Additive Manufacturing 46 (2021).https://doi.org/10.1016/j.addma.2021.102166

[17] W. Lefebvre, G. Rose, P. Delroisse, E. Baustert, F. Cuvilly, A. Simar, Nanoscale periodic gradients generated by laser powder bed fusion of an AlSi10Mg alloy, Materials & Design 197 (2021).https://doi.org/10.1016/j.matdes.2020.109264

[18] W. Li, S. Li, J. Liu, A. Zhang, Y. Zhou, Q. Wei, C. Yan, Y. Shi, Effect of heat treatment on AlSi10Mg alloy fabricated by selective laser melting: Microstructure evolution, mechanical properties and fracture mechanism, Materials Science and Engineering: A 663 (2016) 116-125.https://doi.org/10.1016/j.msea.2016.03.088

[19] T. Kimura, T. Nakamoto, Microstructures and mechanical properties of A356 (AlSi7Mg0.3) aluminum alloy fabricated by selective laser melting, Materials & Design 89 (2016) 1294-1301.https://doi.org/10.1016/j.matdes.2015.10.065

[20] H.R. Kotadia, G. Gibbons, A. Das, P.D. Howes, A review of Laser Powder Bed Fusion Additive Manufacturing of aluminium alloys: Microstructure and properties, Additive Manufacturing 46 (2021) 102155.https://doi.org/10.1016/j.addma.2021.102155

[21] J. Zhang, J. Gao, B. Song, L. Zhang, C. Han, C. Cai, K. Zhou, Y. Shi, A novel crack-free Ti-modified Al-Cu-Mg alloy designed for selective laser melting, Additive Manufacturing 38 (2021) 101829.https://doi.org/10.1016/j.addma.2020.101829

[22] D. Zhang, Y. Han, Z. Sun, Z. Liu, Y. Xing, H. Yin, Study on the laser selective melting and forming process and organizational properties of a TiSi2-modified 7075 aluminum alloy,

Materials Today Communications 42 (2025) 111110.https://doi.org/10.1016/j.mtcomm.2024.111110

[23] D. Gu, X. Rao, D. Dai, C. Ma, L. Xi, K. Lin, Laser additive manufacturing of carbon nanotubes (CNTs) reinforced aluminum matrix nanocomposites: Processing optimization, microstructure evolution and mechanical properties, Additive Manufacturing 29 (2019) 100801.https://doi.org/10.1016/j.addma.2019.100801

[24] Y.K. Xiao, H. Chen, Z.Y. Bian, T.T. Sun, H. Ding, Q. Yang, Y. Wu, Q. Lian, Z. Chen, H.W. Wang, Enhancing strength and ductility of AlSi10Mg fabricated by selective laser melting by TiB2 nanoparticles, Journal of Materials Science & Technology 109 (2022) 254-266.https://doi.org/10.1016/j.jmst.2021.08.030

[25] X.P. Li, G. Ji, Z. Chen, A. Addad, Y. Wu, H.W. Wang, J. Vleugels, J. Van Humbeeck, J.P. Kruth, Selective laser melting of nano-TiB2 decorated AlSi10Mg alloy with high fracture strength and ductility, Acta Mater 129 (2017) 183-193.https://doi.org/10.1016/j.actamat.2017.02.062

[26] J. Yi, X. Zhang, J.H. Rao, J. Xiao, Y. Jiang, In-situ chemical reaction mechanism and non-equilibrium microstructural evolution of (TiB2 + TiC)/AlSi10Mg composites prepared by SLM-CS processing, Journal of Alloys and Compounds 857 (2021).https://doi.org/10.1016/j.jallcom.2020.157553

[27] Y. Chen, Y. Ren, K. Li, B. Dang, Z. Jian, Laser powder bed fusion of oxidized microscale SiC-particle-reinforced AlSi10Mg matrix composites: Microstructure, porosity, and mechanical properties, Materials Science and Engineering: A 870 (2023) 144860.https://doi.org/10.1016/j.msea.2023.144860

[28] D. Zhang, D. Yi, X. Wu, Z. Liu, W. Wang, R. Poprawe, J.H. Schleifenbaumc, S. Zieglerd, SiC reinforced AlSi10Mg composites fabricated by selective laser melting, Journal of Alloys and Compounds 894 (2022) 162365.https://doi.org/10.1016/j.jallcom.2021.162365

[29] Y. Chen, L. Wang, Z. Feng, W. Zhang, Effects of heat treatment on microstructure and mechanical properties of SLMed Sc-modified AlSi10Mg alloy, Progress in Natural Science: Materials International 31(5) (2021) 714-721.https://doi.org/10.1016/j.pnsc.2021.08.003

[30] Y. Guo, W. Wei, H. Huang, S. Wen, W. Shi, X. Zhou, X. Wu, K. Gao, L. Rong, P. Qi, Z. Nie, Approaching an ultrafine microstructure and excellent tensile properties of a novel Er/Zr modified Al–7Si-0.6 Mg alloy fabricated by selective laser melting, Journal of Materials Research and Technology 22 (2023) 1625-1637.https://doi.org/10.1016/j.jmrt.2022.12.040

[31] M.R. Jandaghi, A. Aversa, D. Manfredi, F. Calignano, L. Lavagna, M. Pavese, In situ alloying of AlSi10Mg-5 wt% Ni through laser powder bed fusion and subsequent heat treatment, Journal of Alloys and Compounds 904 (2022).https://doi.org/10.1016/j.jallcom.2022.164081

[32] X. Ai, J. Wang, T. Wen, F. Yang, X. Dong, H. Yang, S. Ji, A high Fe-containing AlSi12 alloy fabricated by laser powder bed fusion, Journal of Materials Research and Technology 18 (2022) 4513-4521.https://doi.org/10.1016/j.jmrt.2022.04.008

[33] J. Fiocchi, C.A. Biffi, A. Tuissi, Selective laser melting of high-strength primary AlSi9Cu3 alloy: Processability, microstructure, and mechanical properties, Materials & Design 191 (2020) 108581.https://doi.org/10.1016/j.matdes.2020.108581

[34] A.V. Pozdniakov, A.Y. Churyumov, I.S. Loginova, D.K. Daubarayte, D.K. Ryabov, V.A. Korolev, Microstructure and properties of novel AlSi11CuMn alloy manufactured by selective laser melting, Materials Letters 225 (2018) 33-36.https://doi.org/10.1016/j.matlet.2018.04.077

[35] Z. Chen, E.M. Elgallad, K. Liu, X.G. Chen, Precipitation Characteristics of HPVDC AlSi10Mg0.3Mn Alloy Under Different Temper Conditions, Metallography, Microstructure, and Analysis (2022).https://doi.org/10.1007/s13632-022-00858-7

[36] E. Pourkhorshid, P. Rometsch, X.G. Chen, Evolution of mechanical properties and microstructure of selective laser melted AlSi10MgMn alloy with different post heat treatments, Materials Science and Engineering: A 915 (2024).https://10.1016/j.msea.2024.147249

[37] B. Gault, M.P. Moody, J.M. Cairney, S.P. Ringer, Specimen Preparation, in: B. Gault, M.P. Moody, J.M. Cairney, S.P. Ringer (Eds.), Atom Probe Microscopy, Springer New York, New York, NY, 2012, pp. 71-110.https://doi.org/10.1007/978-1-4614-3436-8_4

[38] O.C. Hellman, J.A. Vandenbroucke, J. Rüsing, D. Isheim, D.N. Seidman, Analysis of Three-dimensional Atom-probe Data by the Proximity Histogram, Microsc Microanal 6(5) (2000) 437-444

[39] N. Takata, H. Kodaira, K. Sekizawa, A. Suzuki, M. Kobashi, Change in microstructure of selectively laser melted AlSi10Mg alloy with heat treatments, Materials Science and Engineering: A 704 (2017) 218-228.https://doi.org/10.1016/j.msea.2017.08.029

[40] B. Zhang, W. Wei, W. Shi, Y. Guo, S. Wen, X. Wu, K. Gao, L. Rong, H. Huang, Z. Nie, Effect of heat treatment on the microstructure and mechanical properties of Er-containing Al–7Si–0.6 Mg alloy by laser powder bed fusion, Journal of Materials Research and Technology 18 (2022) 3073-3084.https://doi.org/10.1016/j.jmrt.2022.04.023

[41] K.V. Yang, P. Rometsch, C.H.J. Davies, A. Huang, X. Wu, Effect of heat treatment on the microstructure and anisotropy in mechanical properties of A357 alloy produced by selective laser melting, Materials & Design 154 (2018) 275-290.https://doi.org/10.1016/j.matdes.2018.05.026

[42] P. Van Cauwenbergh, V. Samaee, L. Thijs, J. Nejezchlebova, P. Sedlak, A. Ivekovic, D. Schryvers, B. Van Hooreweder, K. Vanmeensel, Unravelling the multi-scale structure-property relationship of laser powder bed fusion processed and heat-treated AlSi10Mg, Sci Rep 11(1) (2021) 6423.https://doi.org/10.1038/s41598-021-85047-2

[43] H. Hu, X. Ding, L. Wang, Numerical analysis of heat transfer during multi-layer selective laser melting of AlSi10Mg, Optik 127(20) (2016) 8883-8891.https://doi.org/10.1016/j.ijleo.2016.06.115

[44] Q. Cai, C.L. Mendis, I.T.H. Chang, Z. Fan, Microstructure evolution and mechanical properties of new die-cast Al-Si-Mg-Mn alloys, Materials & Design 187 (2020).https://doi.org/10.1016/j.matdes.2019.108394

[45] A. Martin, M. San Sebastian, E. Gil, C.Y. Wang, S. Milenkovic, M.T. Pérez-Prado, C.M. Cepeda-Jiménez, Effect of the heat treatment on the microstructure and hardness evolution of a AlSi10MgCu alloy designed for laser powder bed fusion, Materials Science and Engineering: A 819 (2021).https://doi.org/10.1016/j.msea.2021.141487

[46] N. Takata, M. Liu, H. Kodaira, A. Suzuki, M. Kobashi, Anomalous strengthening by supersaturated solid solutions of selectively laser melted Al–Si-based alloys, Additive Manufacturing 33 (2020).https://doi.org/10.1016/j.addma.2020.101152

[47] Y.J. Li, A.M.F. Muggerud, A. Olsen, T. Furu, Precipitation of partially coherent α-Al(Mn,Fe)Si dispersoids and their strengthening effect in AA 3003 alloy, Acta Mater 60(3) (2012) 1004-1014.https://doi.org/10.1016/j.actamat.2011.11.003

[48] S.J. Andersen, H.W. Zandbergen, J. Jansen, C. TrÆholt, U. Tundal, O. Reiso, The crystal structure of the β″ phase in Al–Mg–Si alloys, Acta Mater 46(9) (1998) 3283-3298.https://doi.org/10.1016/S1359-6454(97)00493-X

[49] K. Liu, X.G. Chen, Development of Al–Mn–Mg 3004 alloy for applications at elevated temperature via dispersoid strengthening, Materials & Design 84 (2015) 340-350.https://doi.org/10.1016/j.matdes.2015.06.140

[50] A.Y. Algendy, K. Liu, X.G. Chen, Evolution of dispersoids during multistep heat treatments and their effect on rolling performance in an Al-5% Mg-0.8% Mn alloy, Materials Characterization 181 (2021) 111487.https://doi.org/10.1016/j.matchar.2021.111487

[51] R. Khajeh, M. Javidani, M. Mofarrehi, X.G. Chen, M. Ahmed, A. Farzaneh, A. Heidarzadeh, Enhancing microstructure and mechanical properties of laser powder bed fusion-fabricated AlSi10Mg alloy through tailored friction stir processing and post-heat treatment, Materials Science and Engineering: A 889 (2024) 145855.https://doi.org/10.1016/j.msea.2023.145855

[52] M. Khoshghadam-Pireyousefan, M. Javidani, A. Maltais, J. Lévesque, X.G. Chen, Breaking the strength-conductivity paradigm in hypoeutectic Al–Si alloy via annealing-induced Si nanoprecipitation, Materials Science and Engineering: A 911 (2024) 146924.https://doi.org/10.1016/j.msea.2024.146924

[53] J. Mei, Y. Han, J. Sun, M. Jiang, G. Zu, X. Song, W. Zhu, X. Ran, Improving the comprehensive mechanical property of the AlSi10Mg alloy via parameter adaptation of selective laser melting and heat treatment, Journal of Alloys and Compounds 981 (2024) 173623.https://doi.org/10.1016/j.jallcom.2024.173623

[54] L. Zhao, J.G. Santos Macías, L. Ding, H. Idrissi, A. Simar, Damage mechanisms in selective laser melted AlSi10Mg under as built and different post-treatment conditions, Materials Science and Engineering: A 764 (2019).https://doi.org/10.1016/j.msea.2019.138210

[55] K. Żaba, P. Snopiński, D. Wałach, G.P. Kaczmarczyk, S. Rusz, Insight into the fracture behaviour and mechanical response of ECAP processed cast and LPBF AlSi10Mg alloy, Engineering Fracture Mechanics 295 (2024) 109785.https://doi.org/10.1016/j.engfracmech.2023.109785

[56] J. Fite, S. Eswarappa Prameela, J. Slotwinski, T.P. Weihs, Enhanced mechanical properties by eutectic cells in AlSi10Mg - A promising paradigm for strengthening aluminum in additive manufacturing, Materials Characterization 204 (2023) 113179.https://doi.org/10.1016/j.matchar.2023.113179

[57] M. Khoshghadam-Pireyousefan, M. Javidani, A. Maltais, J. Lévesque, X.G. Chen, Strength-conductivity synergy in hypoeutectic Al-Si conductors via ultrafine-grained embedded Si nanoprecipitates, Materials Science and Engineering: A 929 (2025) 148124.https://doi.org/10.1016/j.msea.2025.148124

[58] L.E.B. Dæhli, S.N. Olufsen, T.A. Kristensen, T. Børvik, O.S. Hopperstad, Influence of constituent particles on fracture of aluminum alloys under high-triaxiality loading, Materials Science and Engineering: A 864 (2023) 144531.https://doi.org/10.1016/j.msea.2022.144531

[59] G. Wang, T. Hua, Y. Liu, S. Chen, Y. Zhou, J. Cao, Effects of Mn addition on the static and dynamic mechanical performance and fracture behavior of Al-8Si-xMn alloy sheets, Journal of Materials Research and Technology (2025).https://doi.org/10.1016/j.jmrt.2025.03.203

[60] S. Chen, K. Liu, X.G. Chen, Precipitation behavior of dispersoids and elevated-temperature properties in Al–Si–Mg foundry alloy with Mo addition, Journal of Materials Research 34(18) (2019) 3071-3081.10.1557/jmr.2019.217

[61] N.T. Aboulkhair, M. Simonelli, L. Parry, I. Ashcroft, C. Tuck, R. Hague, 3D printing of Aluminium alloys: Additive Manufacturing of Aluminium alloys using selective laser melting, Progress in Materials Science 106 (2019).https://doi.org/10.1016/j.pmatsci.2019.100578

[62] D. Knoop, A. Lutz, B. Mais, A. von Hehl, A Tailored AlSiMg Alloy for Laser Powder Bed Fusion, Metals 10(4) (2020).https://doi.org/10.3390/met10040514

[63] L. Zhou, A. Mehta, E. Schulz, B. McWilliams, K. Cho, Y. Sohn, Microstructure, precipitates and hardness of selectively laser melted AlSi10Mg alloy before and after heat treatment, Materials Characterization 143 (2018) 5-17.https://doi.org/10.1016/j.matchar.2018.04.022

[64] D.-K. Kim, J.-H. Hwang, E.-Y. Kim, Y.-U. Heo, W. Woo, S.-H. Choi, Evaluation of the stress-strain relationship of constituent phases in AlSi10Mg alloy produced by selective laser melting using crystal plasticity FEM, Journal of Alloys and Compounds 714 (2017) 687-697.https://doi.org/10.1016/j.jallcom.2017.04.264

[65] E. Cerri, E. Ghio, On the work-hardening behaviour of the additively manufactured Al-Si-Mg alloys: composite-like versus networked microstructure, Materialia (2024) 102282.https://doi.org/10.1016/j.mtla.2024.102282

[66] B. Legendre, Y. Li, P. Kolby, Enthalpy of formation of the α-phase AlMnSi, Thermochimica Acta 354(1) (2000) 1-6.https://doi.org/10.1016/S0040-6031(00)00480-9

[67] A. Takeuchi, A. Inoue, Classification of Bulk Metallic Glasses by Atomic Size Difference, Heat of Mixing and Period of Constituent Elements and Its Application to Characterization of the Main Alloying Element, MATERIALS TRANSACTIONS 46(12) (2005) 2817-2829.https://doi.org/10.2320/matertrans.46.2817

[68] Q. Zhao, B. Holmedal, Y. Li, E. Sagvolden, O.M. Løvvik, Multi-component solid solution and cluster hardening of Al–Mn–Si alloys, Materials Science and Engineering: A 625 (2015) 153-157.https://doi.org/10.1016/j.msea.2014.12.006

[69] J. Peng, S. Bahl, A. Shyam, J.A. Haynes, D. Shin, Solute-vacancy clustering in aluminum, Acta Mater 196 (2020) 747-758.https://doi.org/10.1016/j.actamat.2020.06.062

[70] H. Jiang, Q. Zheng, Y. Song, Y. Li, S. Li, J. He, L. Zhang, J. Zhao, Influence of minor La addition on the solidification, aging behaviors and the tensile properties of Al-Mg-Si alloys, Materials Characterization 185 (2022) 111750.https://doi.org/10.1016/j.matchar.2022.111750

[71] W. Shen, A. Hu, S. Liu, H. Hu, Al-Mn alloys for electrical applications: A review, Journal of Alloys and Metallurgical Systems 2 (2023) 100008.https://doi.org/10.1016/j.jalmes.2023.100008

[72] M. Mizuno, K. Sugita, H. Araki, Structure and stability of vacancy–solute complexes in Al–Mg–Si alloys, Materialia 13 (2020) 100853.https://doi.org/10.1016/j.mtla.2020.100853

[73] D. Bösch, S. Pogatscher, M. Hummel, W. Fragner, P.J. Uggowitzer, M. Göken, H.W. Höppel, Secondary Al-Si-Mg High-pressure Die Casting Alloys with Enhanced Ductility, Metallurgical and Materials Transactions A 46(3) (2014) 1035-1045.https://doi.org/10.1007/s11661-014-2700-8

[74] C.M. Dinnis, J.A. Taylor, A.K. Dahle, Interactions between iron, manganese, and the Al-Si eutectic in hypoeutectic Al-Si alloys, Metallurgical and Materials Transactions A 37(11) (2006) 3283-3291.https://doi.org/10.1007/BF02586163

[75] X.-l. Wang, H.-d. Zhao, Q.-y. Xu, Z.-q. Han, Clustering characteristics of Fe-rich intermetallics in high vacuum die cast AlSiMgMn alloys with high resolution μ-CT inspection, Materials Characterization 207 (2024) 113607.https://doi.org/10.1016/j.matchar.2023.113607

[76] B. Callegari, T.N. Lima, R.S. Coelho, The Influence of Alloying Elements on the Microstructure and Properties of Al-Si-Based Casting Alloys: A Review, Metals 13(7) (2023) 1174.https://doi:10.3390/met13071174

[77] S.N. Khangholi, M. Javidani, A. Maltais, X.G. Chen, Effects of natural aging and pre-aging on the strength and electrical conductivity in Al-Mg-Si AA6201 conductor alloys, Materials Science and Engineering: A 820 (2021) 141538.https://doi.org/10.1016/j.msea.2021.141538

Chapter 4

Laser-based additive manufacturing processability and mechanical properties of Al-Cu 224 alloys with TiB grain refiner additions

(This article is published in: Materials 18 (2025) 516)

Abstract

This study investigated the impact of TiB grain refiner additions on the microstructural evolution, hot tearing susceptibility, and mechanical properties of Al-Cu 224 alloys to enhance their processing performance in the Selective Laser Melting (SLM) process. A simple laser surface remelting method was utilized to simulate the laser-based rapid solidification. The results revealed that the addition of appropriate amounts of TiB grain refiner could completely eliminate the solidification cracks during the laser surface remelting process. The introduction of TiB_2 particles in the melt pools through the TiB grain refiner changed the grain morphology from a coarse columnar to a fine equiaxed structure, and the grain sizes were reduced from 13-15 μm in the base alloys to 5.5 μm and 3.2 μm in the alloys with 0.34 wt% Ti (B-3TiB) and 0.65 wt% Ti (ZV-6TiB) additions, respectively. The hardness values of the modified B-3TiB and ZV-6TiB alloys reached 117 and 130 HV after a T6 heat treatment, which surpassed the hardness of conventional AlSi10Mg alloys by at least 15-30%. This improvement was attributed to the finer grains and from nanoscale θ′/θ″

precipitation. The results demonstrate that the TiB grain refiner addition can significantly improve the processability and mechanical properties of Al-Cu 224 alloys for SLM applications, offering a promising solution to the challenge of high hot tearing susceptibility in high-strength aluminum alloys.

Keywords: Al-Cu 224 alloy, Selective laser melting, TiB grain refiner, Hot tearing susceptibility, Microstructural Characterization, Mechanical properties.

4.1 Introduction

The demand for high-strength aluminum alloys has significantly increased recently, driven by advancements in high-tech industries such as aerospace, automotive, and electronics [1, 2]. Among these alloys, Al-Cu alloys, including typical 206 and 224 cast alloys, and AA2024 and AA2219 wrought alloys, are able to achieve tensile strengths of 400-500 MPa [3-5]. This is primarily due to the presence of numerous nanoscale precipitates (Al_2Cu and S-Al_2CuMg), which form after solutionizing and subsequent artificial aging and provide the main strengthening effect [6]. The precipitation strengthening can be further enhanced by adding transition alloying elements, such as Zr, V, Ti and Sc. It has been reported that microalloying with Zr, V and Ti in Al-Cu 224 cast alloys can significantly affect the mechanical properties at both room and elevated temperatures, thereby enhancing their industrial applicability in internal combustion engines, heat-resistant materials, and fire-resistant structures [7-9], thereby enhancing their industrial applicability in internal combustion engines, heat-resistant materials, and fire-resistant structures.

Selective laser melting (SLM), a powerful additive manufacturing process, has gained great attention in recent years owing to its ability to create complex-shaped materials

[10]. For example, some components of vehicle engines require high strength at both room and elevated temperatures and can be efficiently built by SLM, thereby reducing production time and increasing efficiency [11]. However, the rapid solidification nature of the SLM process introduces challenges such as residual stresses and a high risk of solidification cracks [10, 12, 13]. Consequently, the production of aluminum products by SLM has primarily been limited to alloys that are highly castable or weldable. Although high-Si aluminum alloys, such as typical AlSi10Mg, are good candidates for SLM, their mechanical properties are much lower than those of high-strength aluminum alloys, such as 2xxx, 6xxx, and 7xxx alloys [14]. However, high-strength aluminum alloys are generally susceptible to severe hot tearing during SLM, which limits their widespread use [15].

Controlling hot tearing in high-strength aluminum alloys during SLM has emerged as a critical area of research. The research can be broadly divided into two main approaches: optimizing the SLM process parameters [16, 17] and modifying the chemical composition of alloys [13, 18, 19]. While the former requires a higher energy density, which usually reduces the production rate, the latter can effectively modify the solidification and control cracking. Preheating the powder during the SLM process has demonstrated certain advantages in enhancing processability. For instance, Uddin et al. [20] utilized powder bed preheating up to 500 °C to achieve crack-free fabrication of the alloy AA6061. However, using high-temperature heating in SLM alone is not an efficient method owing to high energy consumption. Tan et al. [21] reported that the processing parameter window of alloy AA2024 for the lowest hot-cracking produced the highest porosity fraction and the lowest sample density. In recent years, chemical composition modification has been widely used. Benoit et al. [18] studied the effect of minor Fe additions on the crack susceptibility of alloy AA6060

and reported that the solidification cracks of AA6060 could be controlled with increasing Fe content up to 0.5 wt%. The co-incorporation effect of Si and TiB_2 for increasing the fracture toughness to resist hot cracking in the 7xxx alloys was studied by Zhou et al. [22]. While Si added extra fluidity to the alloy and reduced solidification shrinkage, TiB_2 remained stable during SLM and functioned as a nucleating agent. Zheng et al. [23] recently examined the effect of TiC nanoparticles in 7075 alloy during SLM. Their results showed that dispersed TiC nanoparticles in AA7075 powders successfully eliminated hot cracking during the SLM process. Sun et al. [19] investigated Er- and Zr-modified Al-Mg alloys after SLM, and reported that the good processability of the modified alloys was associated with the grain-refining effects of Er and Zr. A Ti-modified Al-Cu-Mg alloy was developed specifically for SLM by Zhang et al [24]. The results indicated that the Ti addition can effectively promote the transition from columnar to equiaxed grains in the modified alloy owing to the heterogeneous nucleation effect provided by Al_3Ti. It was also reported that a 2 wt% Zr addition to the base Al-Cu-Mg alloy reduced cracks in SLM by preventing the formation and propagation of cracks [25].

Although some work has been done on modifying the Al-Cu alloy system for the SLM process [21, 26, 27], controlling hot tearing in high-strength Al-Cu alloys is not fully resolved yet. In addition, the feasibility of utilizing a commercial Al-Cu 224 alloy in SLM has not been reported in the literature. This study aims to demonstrate an approach for eliminating solidification cracks in rapidly solidified 224 through the addition of appropriate amounts of TiB grain refiner. Using TiB grain refiner, a widely utilized grain refiner in industrial applications, and preparing the powder without additional mechanical alloying steps can significantly reduce production costs in industrial application. The effect of the TiB

grain refiner on the performance of the SLM process was investigated using a laser surface remelting method [28-30], which simulated the rapid solidification conditions, especially in laser-based manufacturing processes. Five Al-Cu 224 alloys with and without TiB grain refiner modification were prepared by casting and laser surface remelting techniques to compare the hot tearing susceptibility, microstructure, and mechanical properties, and to assess the potential processability of such alloys. This study provides a new approach and insights into enhancing the hot tearing resistance and mechanical properties of high-strength Al-Cu 224 alloys for SLM applications.

4.2 Materials and methods

4.2.1 Materials preparation

Five Al-4.5Cu based alloys were prepared. The first alloy was a typical Al-Cu 224 cast alloy containing 4.7% Cu and 0.35% Mn with minor Mg and Fe additions (0.10-0.12% for each), and is denoted as the base alloy. The second alloy was modified with a 0.34% Ti addition to the base alloy using Al-5Ti-1B master alloy and is denoted as B-3TiB alloy. The third alloy includes 0.15% Zr and 0.20% V additions to the base alloy and is designated as the ZV alloy. The fourth and fifth alloys were modified with 0.3% and 0.65% Ti additions to the third alloy, respectively, using Al-5Ti-1B master alloy, and are designated as ZV-3TiB and ZV-6TiB alloys. Ti concentrations were chosen based on preliminary results and cost-effectiveness, ensuring effective control of hot tearing. All alloys were batched in an electric resistance furnace with a melting temperature of 750 °C, and then poured into a copper permanent mold to obtain thin-wall cast plates measuring 110 mm × 110 mm × 4 mm with a solidification cooling rate of ~20 ^{o}C/s. The chemical compositions of the five alloys analyzed using optical emission spectroscopy are listed in Table 4-1. All chemical

compositions in this paper are given in wt.% unless otherwise indicated. Samples with dimensions of 40 × 10 × 4 mm were machined from the cast plates, sand-blasted, and then ground using SiC paper to maintain the same surface roughness.

These samples were placed on the substrate of an SLM SOLUTIONS 125 machine equipped with a 400 W IPG laser for laser surface remelting (LSR) under an Ar atmosphere. During the LSR process, linear remelting tracks were produced with a laser power of 370 W, a spot size of 100 µm, and scan speeds of 300, 500, and 700 mm/s. In addition, 20 parallel line scans with the same laser power and spot size, a scan speed of 500 mm/s and a hatch distance of 130 µm were performed for each alloy to generate a region of overlapping melt pools for hardness measurement. This approach was used to explore the effects of the process parameters and alloy compositions on the processability of Al-Cu alloys under conditions that are similar to the rapid solidification processing by SLM. A schematic of the LSR process is shown in Figure 4-1.

To study the aging response and the potential of precipitation strengthening, a part of the LSR samples was subjected to a T6 heat treatment, which included a two-step solution treatment at 495-528 °C followed by water quenching and artificial aging at 160 °C for different times. The heat treatment procedure is illustrated in Figure 4-2.

Table 4-1: Chemical compositions of experimental alloys (wt.%).

	Si	Fe	Cu	Mn	Mg	Zr	V	Ti	Al
Base	0.06	0.12	4.7	0.35	0.14	0.01	0.01	**0.05**	Bal.
B-3TiB	0.22	0.12	4.59	0.36	0.10	0.01	0.02	**0.34**	Bal.
ZV	0.04	0.11	4.69	0.34	0.12	0.15	0.21	**0.05**	Bal.
ZV-3TiB	0.11	0.12	4.35	0.34	0.08	0.15	0.22	**0.31**	Bal.
ZV-6TiB	0.09	0.13	4.36	0.34	0.07	0.14	0.24	**0.65**	Bal.

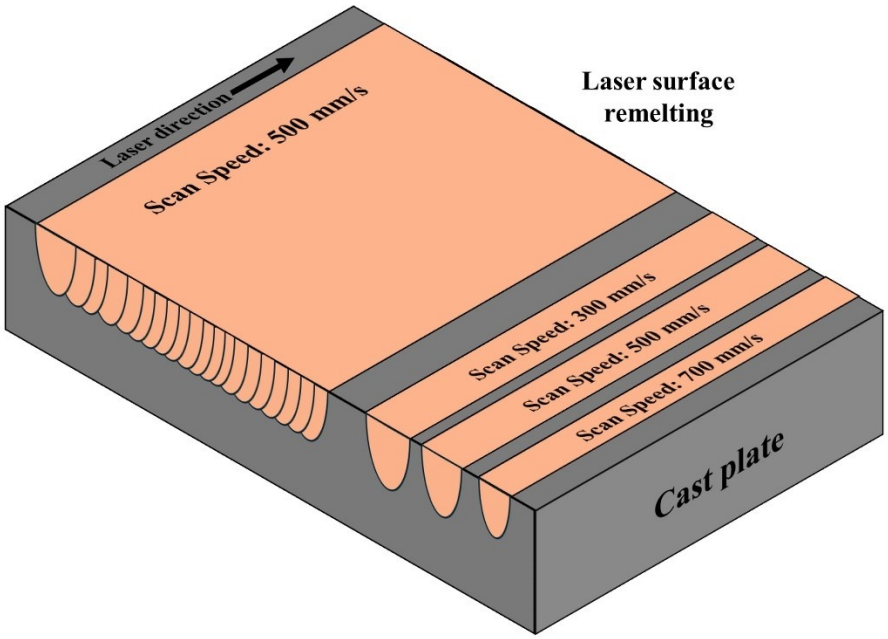

Figure 4-1: Schematic of the laser surface remelting process.

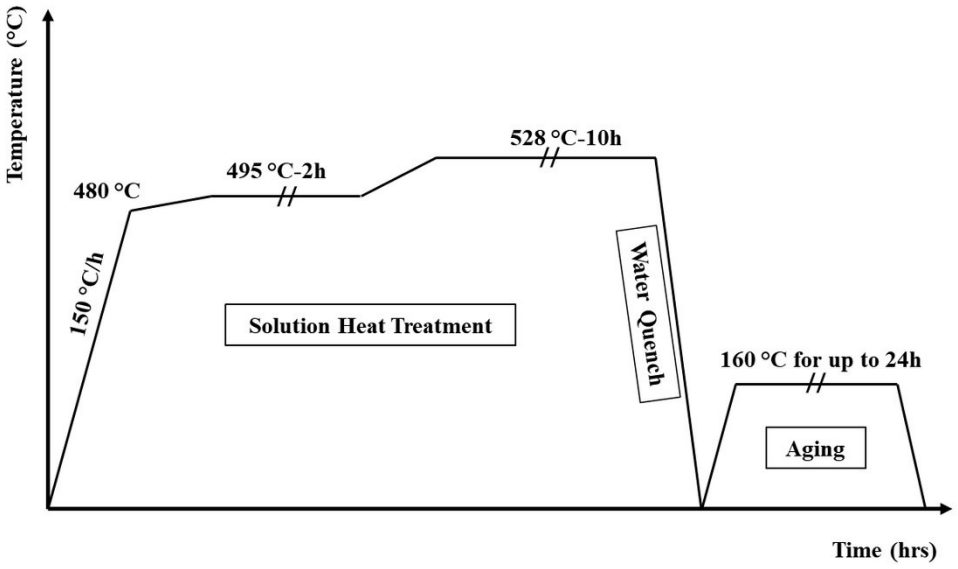

Figure 4-2: Schematic of the T6 heat treatment applied in this study.

4.2.3 Microstructural and mechanical characterization

Transverse cross-sections of the laser-melted linear tracks were prepared by a standard metallographic procedure for microstructural analysis. At least five cross-sections along the length of the tracks were investigated for each alloy composition and process condition. An optical microscope and a scanning electron microscope (SEM, JEOL JSM-6480LV) were used to examine the melt pool microstructures. The grain structures were characterized using the electron backscatter diffraction (EBSD) technique. The EBSD orientation maps were collected using an accelerating voltage of 20 kV and a step size of 1 μm, and the data were processed using the HKL Channel 5 software. A transmission electron microscope (TEM, JEOL JEM-2100) was also used to investigate the precipitation microstructures inside the pool after the T6 heat treatment. The TEM samples were prepared in a twin-jet polishing unit operated at 20 V in a solution consisting of 30 vol% nitric acid and 70 vol% methanol at -30 °C after the grinding and polishing procedure. The thicknesses of the TEM samples were measured using a convergent beam diffraction pattern. The mechanical properties of each pool were evaluated based on the Vickers hardness using an NG-1000 CCD machine. The hardness measurements were performed at a load of 25 g and a dwell time of 20 s. At least ten indentations were made to obtain the average value in the parallel scan areas.

4.2.3 Solidification simulation and hot tearing index

ThermoCalc software (version 2023 with the TCAL7 database) was used to simulate the solidification of the alloys. The Scheil-Gulliver (non-equilibrium) solidification model was used for the simulation, with a maximum temperature step size of 1 °C. The simulation predicted the temperature (T) versus solid fraction (fs) curve and the formation of

intermetallic phases. The hot tearing susceptibility of the studied alloys was accessed using the Easton criterion with the following equation [31]:

$$HTI_E = \int_{T_0}^{T_{CO}} f_s(T).\, dT \qquad (1)$$

In this method, two parameters are considered: T_0, denoting the temperature of coherency, where feeding transitions interdendritically, and T_{CO}, the temperature of coalescence, where solidification reaches a point of solidity. In this study, T_0 was set at 0.7, and T_{CO} was set at 0.98.

4.3 Results

4.3.1 As-cast microstructures

The as-cast microstructures of the base and ZV alloys are shown in Figure 4-3a and b. Both alloys exhibited similar microstructures, which consisted of Al grains with Al_2Cu and Fe-rich intermetallics distributed along the cell/grain boundaries. Fe-rich intermetallics were mainly Al_7Cu_2(Fe, Mn) and Al(Fe, Mn)Si, determined by the phase morphology and SEM-EDS analyses, and relevant literature [7, 9]. The majority of the Zr and V in the ZV alloy was dissolved in the matrix, which accounts for the scarcity of Zr/V-containing intermetallics found in the matrix [7]. With the addition of TiB grain refiner in both alloys, the most notable changes were the presence of Ti-containing intermetallics and TiB_2 particles in the matrix, as shown in the ZV-6TiB alloy as an example (Figure 3c and d). The excess Ti produced Al_3Ti-type intermetallic particles, and the SEM-EDS analysis revealed that some Zr, and V dissolved in the Al_3Ti-type particles (Figure 3e). The average size of those particles is 10 μm. An enlarged SEM image of ZV-6TiB alloy showed some fine particles with an average

size of 1 µm mostly distributed in the middle of the Al grains (Figure 3d). The SEM-EDS analysis indicated that these particles were TiB_2 (Figure 4-3e).

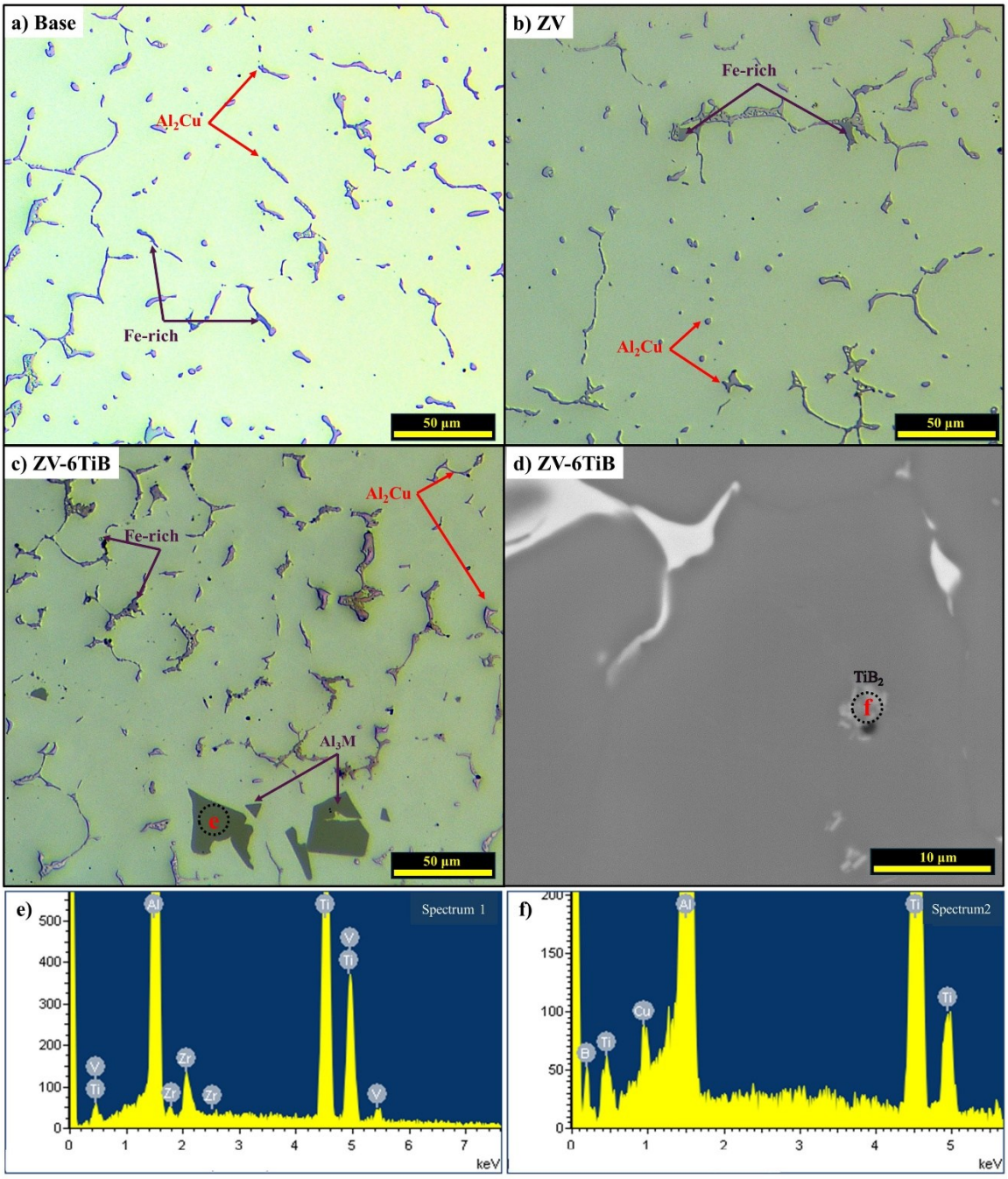

Figure 4-3: As-cast optical microstructures: a) base, b) ZV, and c) ZV-6TiB alloys, d) an enlarged SEM backscattered image from ZV-6TiB alloy showing fine TiB_2 particles, e) SEM-EDS spectrum of Al_3Ti particles in Fig. 3c, f) SEM-EDS spectrum of TiB_2 particles in Fig. 3d.

4.3.2. Microstructures after laser surface remelting

4.3.2.1 Cracking in the melt pools

The melt pools after LSR for the base and B-3TiB alloys are shown in Figure 4-4. In the base alloy, macro cracks can be seen in all melt pools regardless of the laser scan speed (a-d). These cracks, indicated by red arrows, were principally in the middle of the melt pool and localized between adjacent grains. It was reported that such cracks occur during the last stages of solidification, where coherency in the solidifying melt pool begins [18]. The large solidification interval of Al-Cu alloys was identified as the main reason for the high cracking susceptibility in the final stage of solidification [16], where the liquid phase cannot fully penetrate between the grains, and the thermal contraction of the solidified material causes high stresses that exacerbate cracking [32]. In contrast, the melt pools of the B-3TiB alloy were solidified completely without any cracks (Figure 4e-h). This indicates that the incorporation of the TiB grain refiner can effectively control cracking in the melt pools.

The melt pools for the ZV alloy and two other modified alloys are presented in Figure 4-5. In the ZV alloy (Figure 4-5a-d), severe macro cracks occurred in all melt pools regardless of the scan speeds used in the LSR process. In the ZV-3TiB alloy (Figure 4-5e-h), some light cracks were observed in the single scan melt pools at different speeds, but severe cracks were still observable in the multilayer area scanned at 500 mm/s. Compared with the cracks in the ZV alloy, the number and severity of cracks in the melt pools decreased. While the cracking in the B-3TiB alloy could be controlled with the addition of 0.3%Ti from an Al-5Ti-1B grain refiner, the same amount of grain refiner in the ZV-3TiB alloy could not avoid some cracks in the melt pools. This clearly demonstrates a higher tendency for cracking in the ZV alloy than in the base alloy. With further modification by a

higher amount of grain refiner in the ZV-6TiB alloy (Figure 4-5i-l), all cracks disappeared in the melt pools, whether in single tracks with different scan speeds or in multilayer areas.

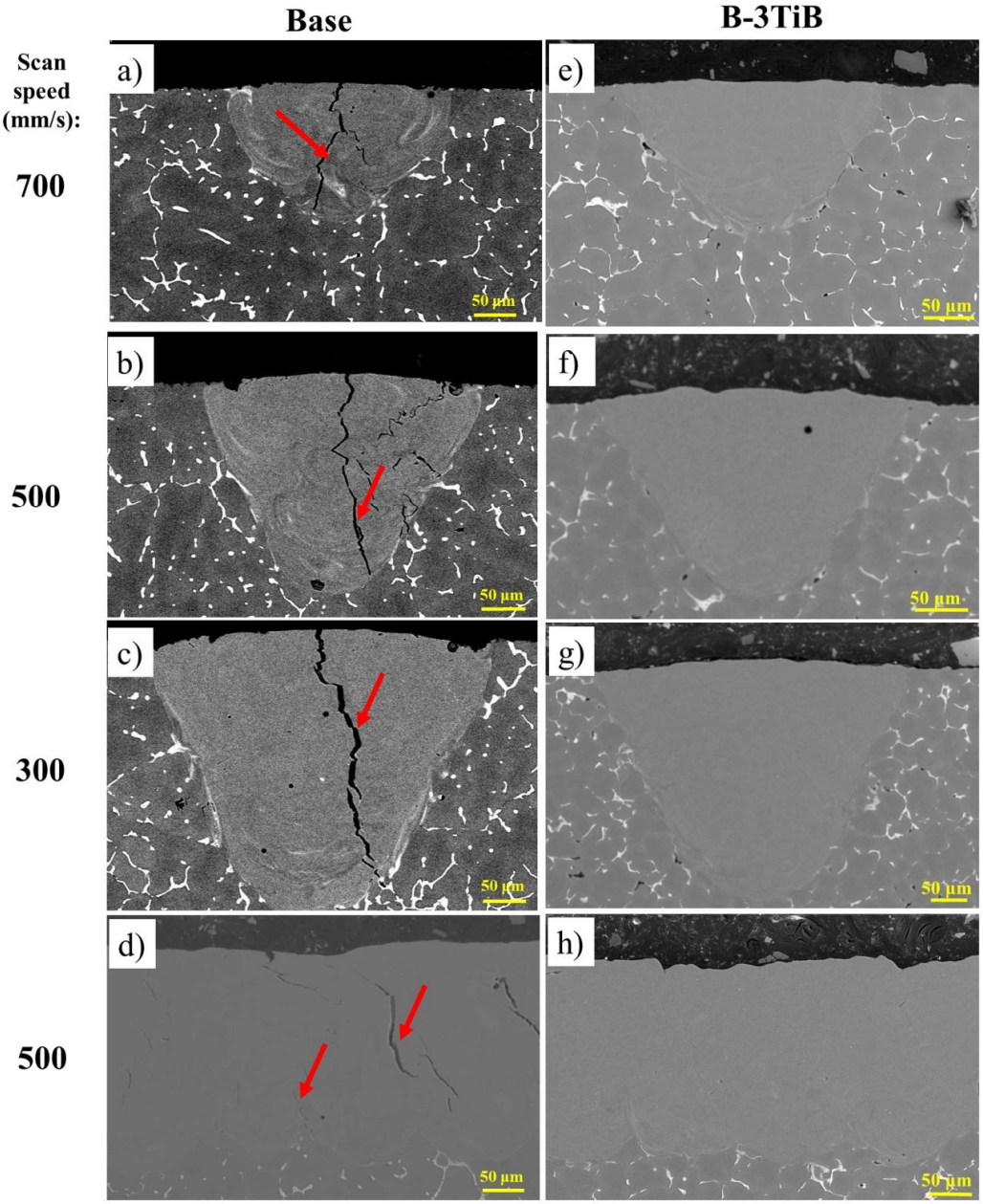

Figure 4-4: SEM micrographs showing cross-sections of melt pools at different laser scan speeds: (a, b, c, and d) the base alloy, with cracks indicated by red arrows; and (e, f, g, and h) the B-3TiB alloy.

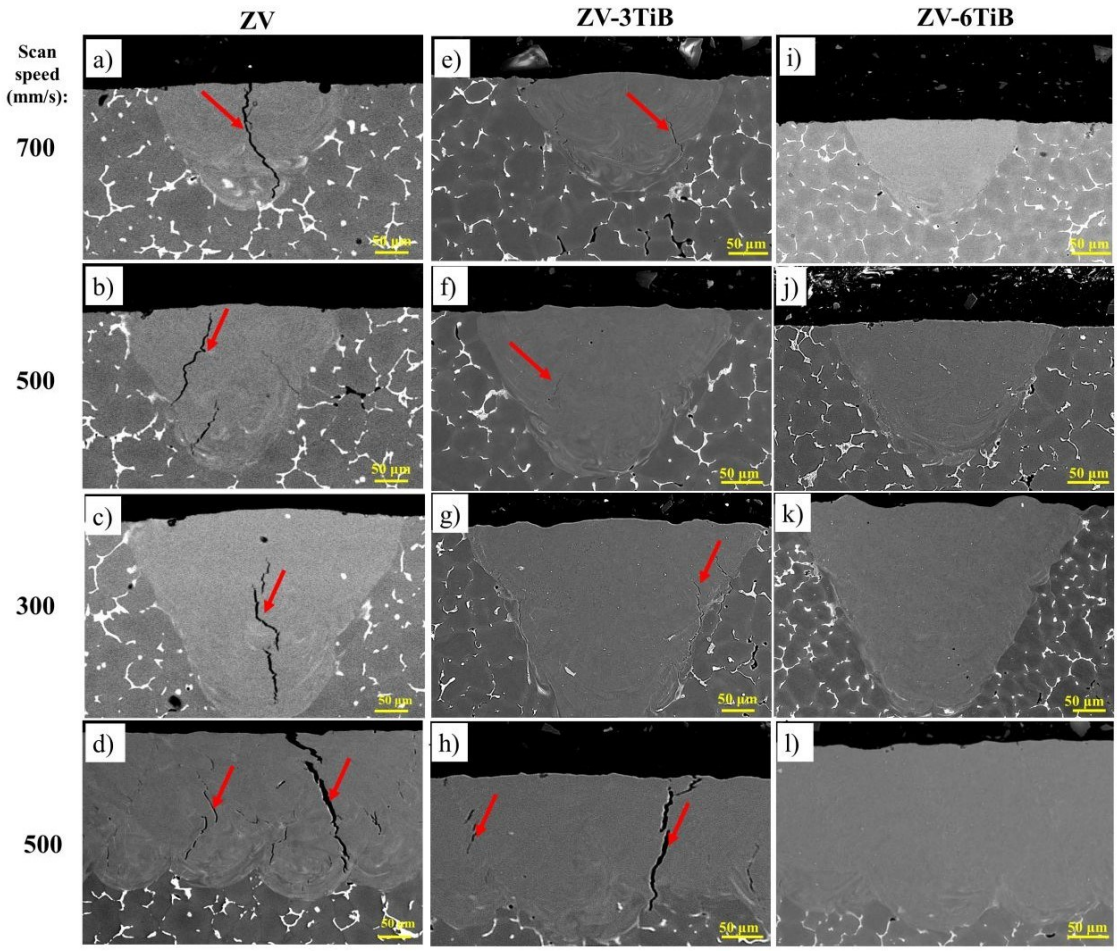

Figure 4-5: SEM micrographs showing cross-sections of melt pools under different laser scan conditions: (a, b, c, and d) the ZV alloy, (e, f, g, and h) the ZV-3TiB alloy, and (i, j, k, and l) the ZV-6TiB alloys. The cracks are indicated by red arrows.

4.3.2.2 Grain sizes in the melt pools

In conventional casting, grain refinement can be achieved through inoculation treatments that add potent nucleation particles or suitable solutes to inhibit grain growth [33]. In contrast, the high cooling rate of LSR reduces constitutional supercooling effects, even with a high level of Cu as the main solute in the base and ZV alloys, thereby causing large elongated grains to form due to epitaxial growth (Figure 4-6c and 4-7c). Therefore, researchers have adopted inoculation treatments using nucleation particles such as Al_3Ti [34]

and Al_3Zr [25], or adding Er and Zr [19] in SLMed aluminum alloys to control the grain structure.

The melt pools in the base and B-3TiB alloys are shown in Figure 4-6a and 4-6b, respectively. The EBSD orientation map of the base alloy shows that most grains in the melt pool were large and elongated in the heat transfer direction (Figure 4-6c). These grains were grew epitaxially from the partially melted substrate at the melt pool boundary, as in other observations [35]. The average grain size in the base alloy was measured to be 13.4 μm.

In contrast, the EBSD orientation map of the modified B-3TiB alloy shows mostly equiaxed and smaller grains with an average grain size of 5.5 μm (Figure 4-6d). The incorporation of the TiB grain refiner significantly reduced the grain size in the melt pools. Similar effects were reported in that TiC nanoparticles promoted the columnar-to-equiaxed grain transition in SLMed AA2024 Al alloys [35]. Martin et al. reported [13] that ZrH_2 pre-alloyed 7075 and 6061 Al powders increased nucleation sites, leading to a fully equiaxed grain structure in SLM-processed alloys. It was also observed that microscale $Al_3(Sc,Zr)$ precipitates facilitated a fully equiaxed grain structure in an Al-Mg-Sc-Zr alloy produced via direct energy deposition [36].

Figure 4-7a and 4-7b shows the melt pools for the ZV and ZV-6TiB alloys, respectively. The EBSD orientation map of the ZV alloy revealed that most grains were mainly elongated in the heat transfer direction (Figure 4-7c). In contrast, the ZV-6TiB alloy exhibited a fine, equiaxed grain structure. The average grain sizes were reduced from 15.4 μm in the ZV alloy to 3.2 μm in the modified ZV-6TiB alloy. These results also show that the higher level of grain refiner addition in the ZV-6TiB alloy reduced the grain size more effectively than that in the B-3TiB alloy.

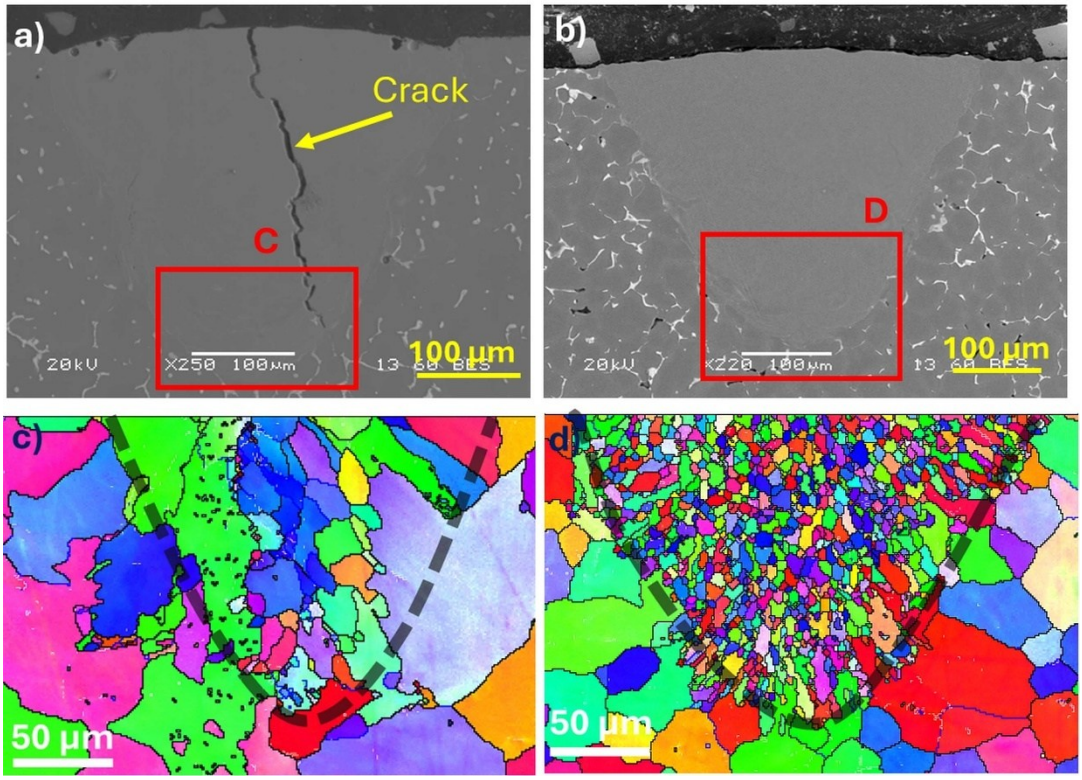

Figure 4-6: SEM micrographs of the melt pools at a 300mm/s scan speed for: a) the base alloy and b) the B-3TiB alloy; c) EBSD orientation map of the base alloy from the selected area C of Fig. 4-6a, and d) EBSD orientation map of the B-3TiB alloy from the selected area D of Fig. 4-6b. The dotted gray lines indicate the melt pool boundaries.

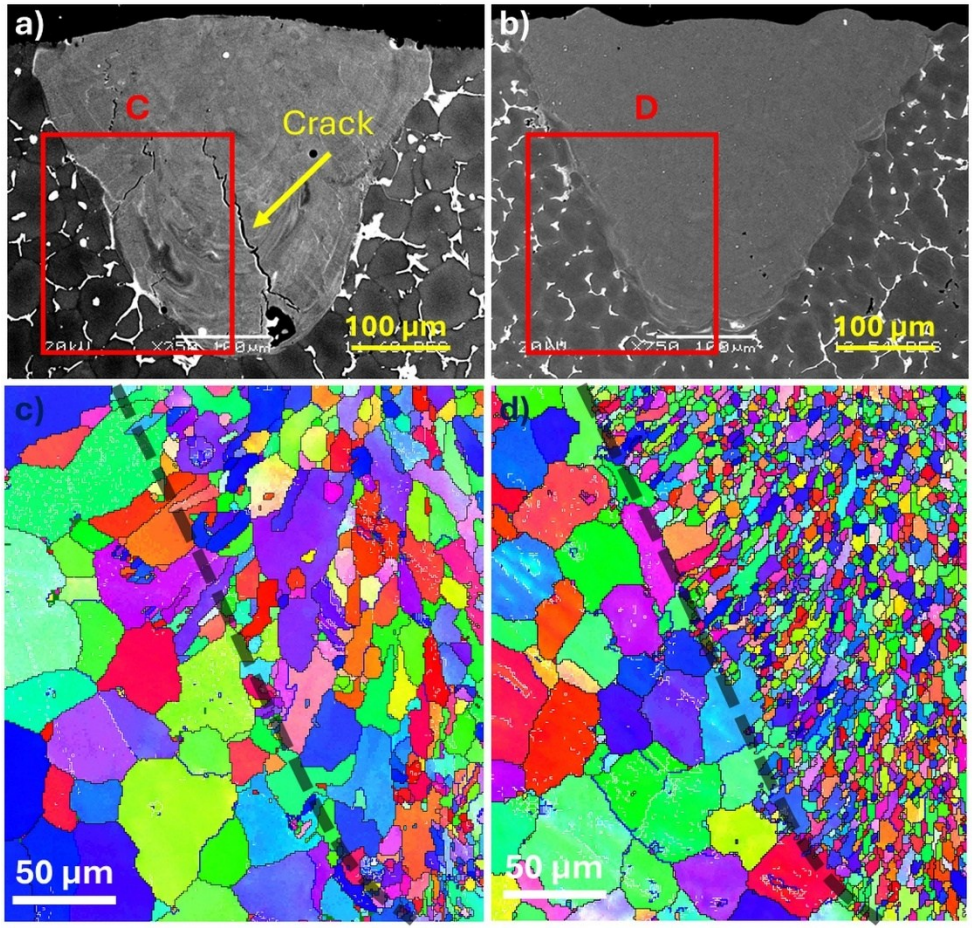

Figure 4-7: SEM micrographs of the melt pools at a 300mm/s scan speed for: a) the ZV alloy and b) the ZV-6TiB alloy; c) EBSD orientation map of the ZV alloy from the selected area C in Fig. 4-7a, and d) EBSD orientation map of the ZV-6TiB alloy from the selected area D in Fig. 4-7b. The dotted gray lines indicate the melt pool boundaries.

Figure 4-8 shows the microstructures of the B-3TiB and ZV-6TiB alloys in the centers of melt pools. In both alloys, α-Al solidified with cellular structures, while Cu-rich intermetallics solidified in the intercellular regions. Both alloys exhibit small equiaxed grains, which is also demonstrated in Fig. 6d and Fig. 7d. Small particles were observed in the middle of the majority of the grains, and they appear as white spots in the backscatter SEM images (as in the yellow circles in Figure 4-8a and 8b). The EDS analysis of those particles in both alloys indicates that they are TiB_2 particles (Figure 4-8c). The average size

of those TiB_2 particles is ~0.9 μm in both alloys. The number densities of the TiB_2 particles in the B-3TiB and ZV-6TiB alloys are 2.8×10^{-3} and 5.6×10^{-3} μm^{-2}, respectively. In general, TiB_2 particles have excellent compatibility with aluminum alloys owing to their good wettability with Al liquid and their excellent properties such as high hardness, high stiffness, high melting point and considerable chemical stability. It is reported that the TiB_2 particle is an excellent grain growth inhibitor in the Al matrix, which can provide low-energy-barrier heterogeneous nucleation sites ahead of the solidification front and induce a change in the grain morphology from a columnar to a fine equiaxed structure [13].

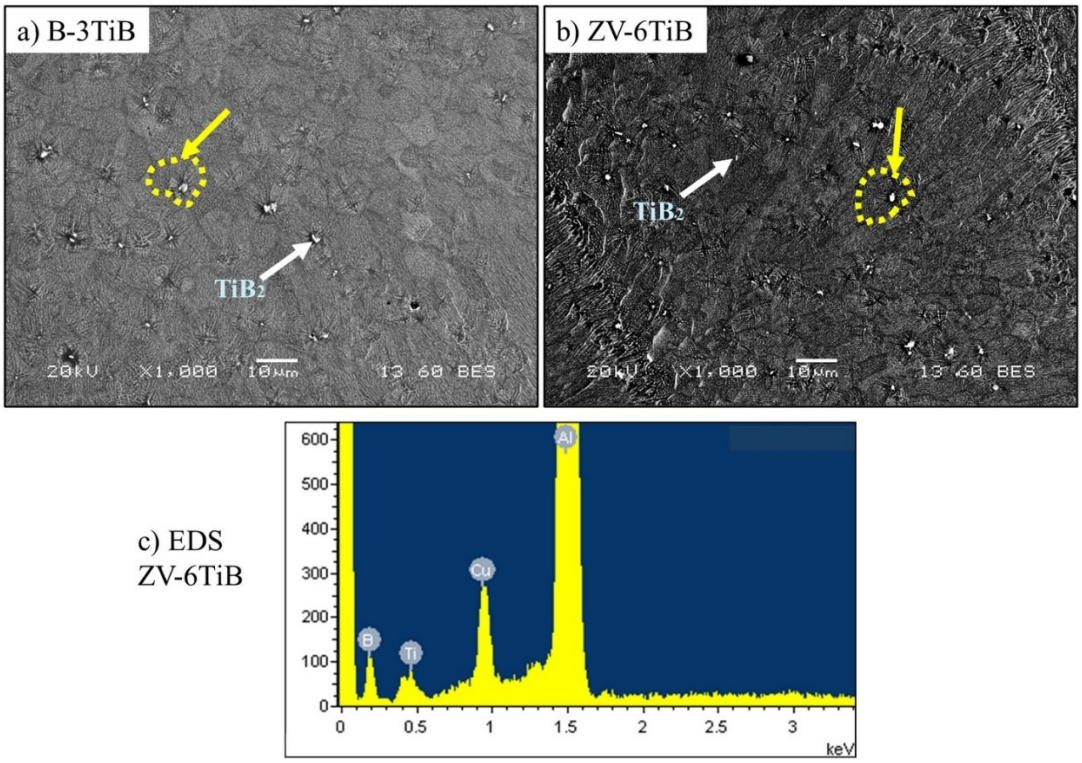

Figure 4-8: Microstructures in the centers of melt pools (300 mm/s) for: a) the B-3TiB alloy and b) the ZV-6TiB alloy; c) SEM-EDS result of a small TiB2 particle in Figure 4-8b. The dotted yellow circles indicate the small equiaxed grain boundaries.

4.3.3. Effect of T6 heat treatment

4.3.3.1 Mechanical properties

To achieve the maximum mechanical properties of the two TiB-modified alloys (B-3TiB and ZV-6TiB), they were subjected to a T6 heat treatment including a solution treatment followed by water quenching and artificial aging at 160 °C (Figure 4-2). The microhardness of both alloys as a function of aging times are shown in Figure 4-9. The initial hardness of tested samples before the LSR process was approximately 75 HV, and then the hardness of two tested materials increased to 85-90 HV after the LSR process. After aging for 3 h, the T6 treatment improved the hardnesses to ~110 HV, which is attributed to precipitation strengthening in the T6 condition [7]. After more than 8 h of aging, the hardnesses of the ZV-6TiB sample were clearly higher than those of the B-3TiB sample. The B-3TiB alloy was already peak-aged after 6 h, while the ZV-6TiB alloy was only peak-aged after 20 h but with a hardness of 130 HV, compared to 117 HV for alloy B-3TiB in the peak-aged condition. The peak-aged B-3TiB and ZV-6TiB samples were selected for further microstructural characterization.

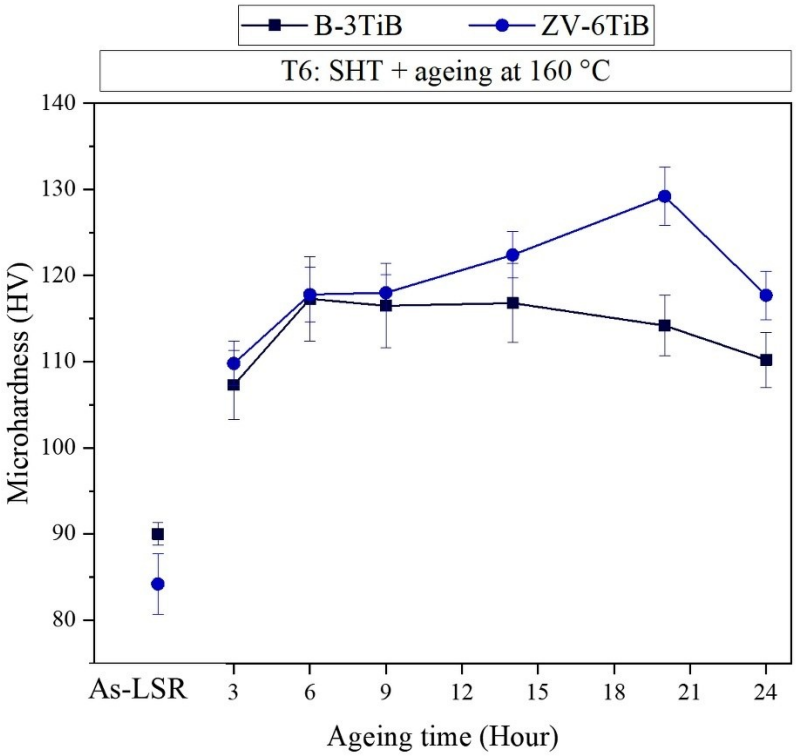

Figure 4-9: Aging response of the B-3TiB and ZV-6TiB alloys during T6 heat treatment.

4.3.3.2 Microstructural evolution

The microstructures and grain structures in the melt pools of the B-3TiB and ZV-6TiB alloys after peak-aged T6 treatments are presented in Figure 4-10. Following T6 treatment, the cellular structures in both samples completely disappeared, although some intermetallic particles persist in the Al matrix. EBSD analysis indicates that the average grain size of the B-3TiB alloy slightly increased to 6.5 μm compared to the as-laser scanned condition, while the average grain size of the ZV-6TiB alloy remained approximately the same at 3.5 μm. SEM-EDS analysis of the intermetallic particles indicated that they are Ti-rich intermetallics (Figure 4-10c and 4-10d). This suggests that the high density of such intermetallic particles in the ZV-6TiB alloy plays a significant role in maintaining its small equiaxed grain size after the solution treatment in the T6 condition.

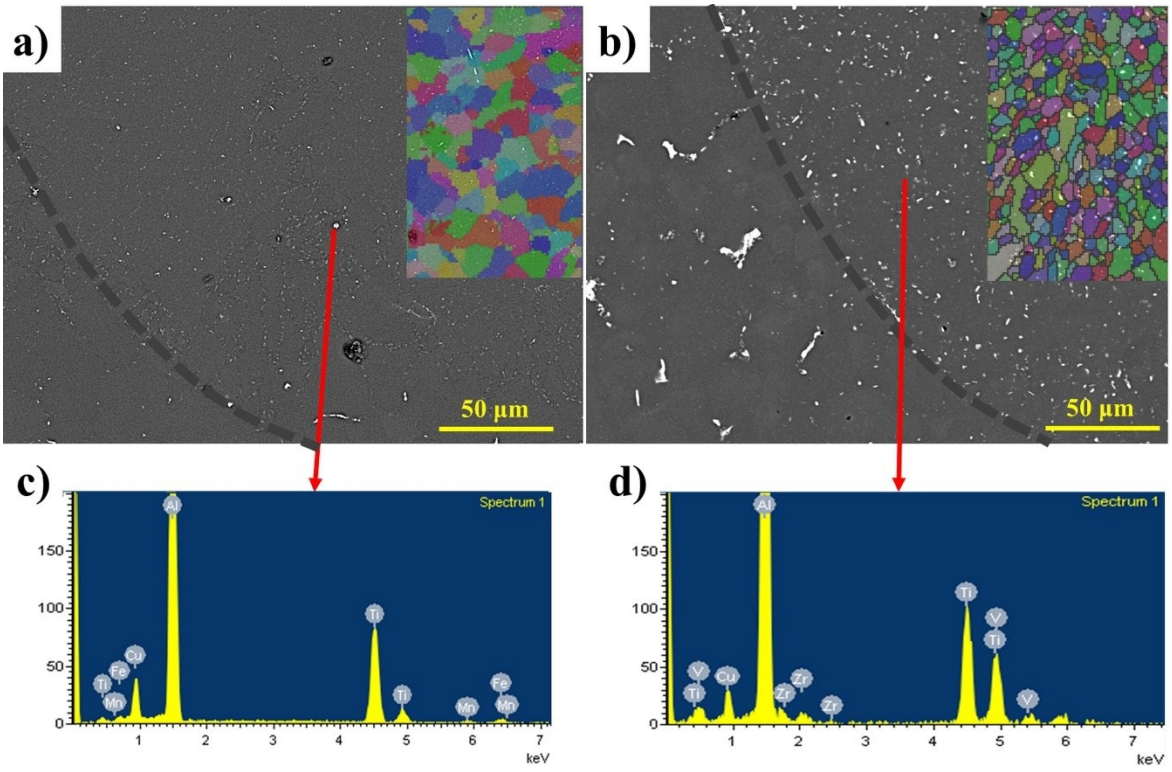

Figure 4-10: Microstructures of the melt pools after T6 heat treatment: a) the B-3TiB alloy and b) the ZV-6TiB alloy; c) SEM-EDS result of the particles in Figure 4-10a; d) SEM-EDS result of the particles in Figure 4-10b.

The bright-field TEM images in Figure 4-11, viewed along the <001>α-Al direction, show the precipitation microstructures of the B-3TiB and ZV-6TiB alloys after T6 treatment. Two types of disk-shaped Al_2Cu precipitates were observed in the Al matrix. According to their size, shape, and the corresponding selected area diffraction patterns (SADP), these nanoscale precipitates were mainly θ′-phase, and to a lesser extent, θ″-Al_2Cu phase [7, 8], which were the main strengthening phases in both alloys. The average length of the Al_2Cu precipitates in the B-3TiB alloy was measured to be 42 nm, and the average thickness was 3 nm. On the other hand, the average length and thickness of these precipitates in the ZV-6TiB alloy were 40 and 2.8 nm, respectively. The number density N_v was calculated based on the

measured number of precipitates ($N_1 + N_2$) along the two explicit (001)Al directions in the TEM images using the following equation:

$$N_V = (N_1 + N_2)\frac{(1+\frac{t+d_t}{2\sqrt{A_s}})}{A_s(t+d_t)} \qquad (2)$$

Where A_s is the area of the TEM images, t is the thickness of the TEM foil and d_t is the effective width of the precipitates. The number densities of the θ′/θ″-Al_2Cu precipitates in the B-3TiB and ZV-6TiB alloys were determined to be 12100 and 16000 μm^{-3}, respectively. Owing to its higher number density of θ′/θ″-Al_2Cu precipitates in the Al matrix, it is expected that the strength of the ZV-6TiB alloy is higher than that of the B-3TiB alloy, which is consistent with results in Figure 4-9.

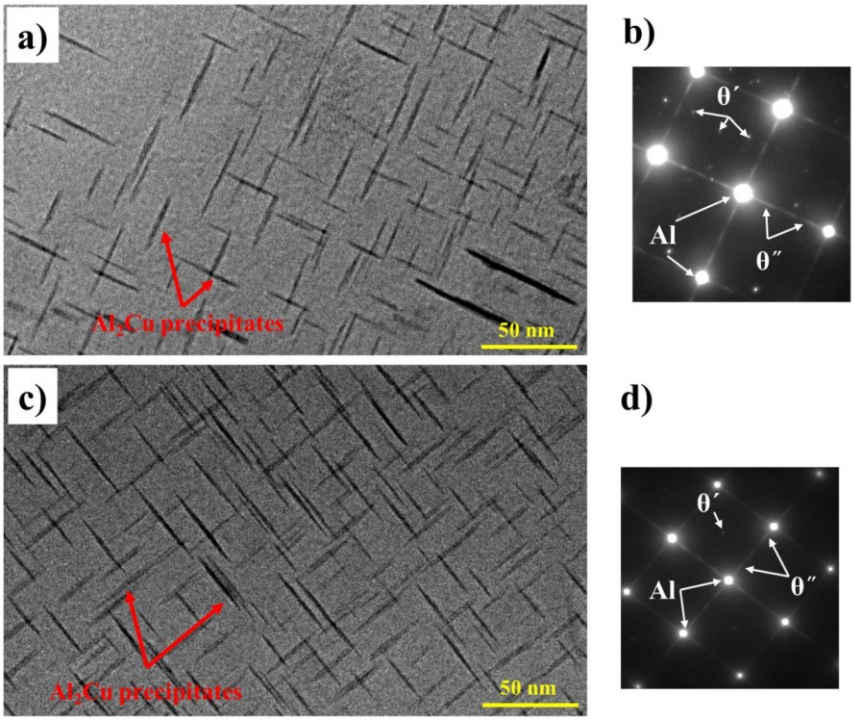

Figure 4-11: Bright-field TEM images viewed along <001>α-Al showing the precipitation microstructures of: a) the B-3TiB alloy, and c) the ZV-6TiB alloy in their respective peak-aged T6 conditions. The disk-shaped precipitates in the Al matrix were θ′- and θ″-Al2Cu precipitates as indicated by the corresponding SADPs in the b) B-3TiB alloy, and d) ZV-6TiB alloy.

4.4 Discussion

4.4.1. Effect of energy density on melt pools

Energy density is a critical parameter in materials processing, particularly in techniques such as laser welding and SLM manufacturing. It represents the amount of energy delivered per unit area and directly influences the characteristics of the melt pool, which is important for optimizing SLM processing to achieve the desired material properties. The linear energy density, ED_l, is one of the most commonly used parameters in the literature, as shown in the following equation [10]:

$$ED_l = \frac{P}{v} \qquad (3)$$

Where P is the laser power (W), and v is the scan speed (mm/s). This parameter is used in this study to compare the melt pool sizes in a single track of the LSR process. The effect of the linear energy density on the melt pool sizes of different alloys is shown in Figure 4-12. The presence of alloying elements and TiB_2 particles in the alloys studied did not significantly affect the melt pool sizes at each energy density. However, as the linear energy density increased from 0.52 to 0.74 J/mm and further to 1.23 J/mm, the average melt pool areas increased by 88% and then by another 68%, respectively. Despite this, no relationship between energy density and cracking susceptibility was observed across all the samples. This is likely because of the similar range of input energy densities for the studied alloys, resulting in a comparable solidification rate under all conditions.

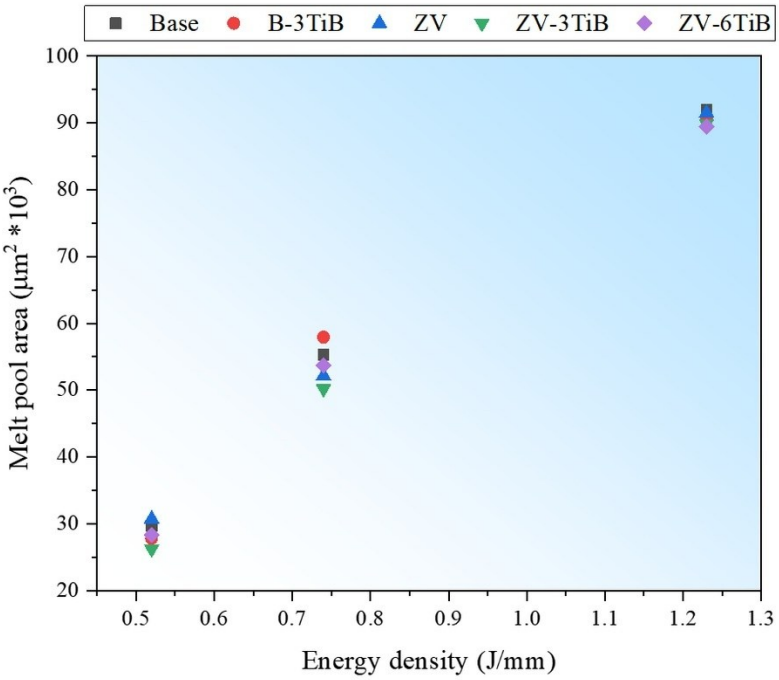

Figure 4-12: Effect of energy density on melt pool sizes for different alloys in single tracks of the LSR process.

4.4.2. Hot tearing susceptibility

4.4.2.1 Thermocalc calculation

Figure 4-13a presents the solidification sequence of the base 224 alloy. The solidification began at approximately 650 °C with α-Al. The Mn-rich and Fe-rich intermetallic phases started to be precipitated around 612 °C and 580 °C, respectively. In the final stage of solidification, Al_2Cu intermetallics emerged at ~530 °C, and solidification ended at 513 °C. The solidification interval of this alloy is considerably broad at approximately 140 °C. This is significantly broader than that of the commonly used alloys in SLM, such as AlSi10Mg alloys, which have a solidification interval of approximately 35 °C. The extensive interval in Al-Cu 224 alloys significantly increases the susceptibility to hot tearing during solidification. To numerically compare the hot tearing susceptibility for the studied alloys, Easton's criterion using the hot tearing index, HTI_E in Eq. 1, was applied [31]. For the alloys modified with TiB grain refiner, it was assumed that all B reacts with Ti to form TiB_2 particles, and hence only excess Ti in the Al matrix was considered [37].

Figure 4-13b shows the comparison of the hot tearing index for the studied alloys. All alloys, including the modified ones, exhibited a higher HTI_E compared to the conventional AlSi10Mg alloys. The ZV alloy showed a higher HTI_E than the base alloy. With the addition of TiB grain refiner to modify the chemical composition, the HTI_E only slightly decreased in the modified alloys, and it remains significantly higher than that of the more commonly castable AlSi10Mg alloys. The TiB additions in the B-3TiB and ZV-6TiB alloys completely eliminated the hot cracks in the laser surface remelting process and this corresponds to the lower HTI_E values for these alloys in Figure 13b. However, since these

HTI_E values are only slightly lower than the others, this suggests that the modification of the chemical composition is not the primary factor for reducing the hot tearing susceptibility.

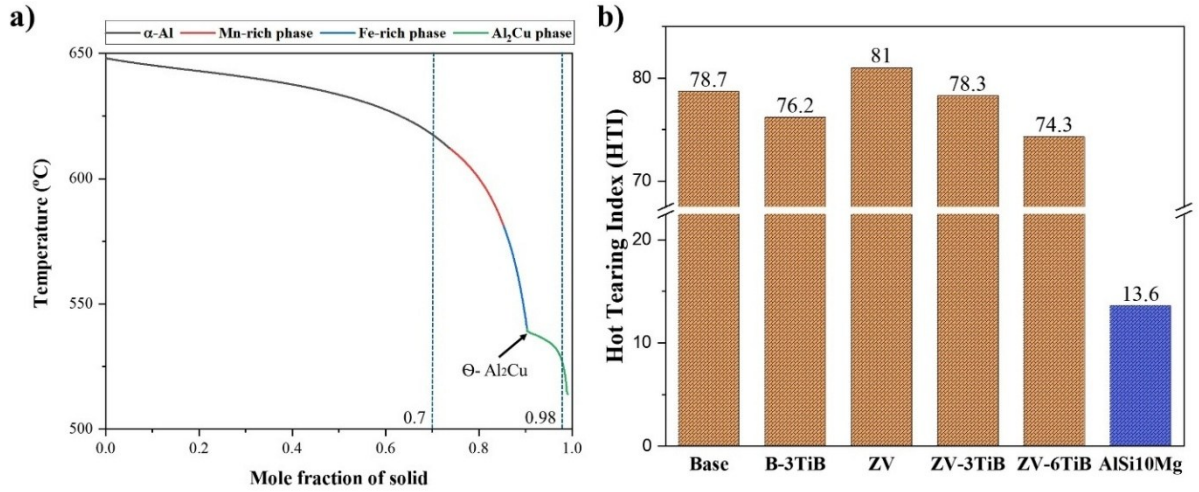

Figure 4-13: a) Solidification sequence and temperature vs solid fraction predicted for the base 224 alloy using the Scheil-Gulliver (non-equilibrium) model in ThermoCalc, and b) hot tearing susceptibility for the studied alloys predicted using Equation 1.

4.4.2.2 Effect of the grain size

In general, thermal shrinkage, along with a broad solidification interval, is primarily responsible for the occurrence of hot tearing during solidification, especially in high-strength aluminum alloys such as the 2xxx, 6xxx, and 7xxx series [13, 38]. In this study, the base and ZV alloys have a solidification interval of around 140 °C, which can cause high shrinkage tension in the final stages of solidification. The linear thermal shrinkage can be described by the following equation:

$$\varepsilon = \alpha \, d \, \Delta T \qquad (4)$$

where ε is the thermal contraction in the solidified part, α is the coefficient of thermal contraction, d is the average grain size of the solidified part, and ΔT is the solidification interval. It is evident that larger grains produce higher shrinkage contraction in the final

stages of solidification, leading to greater stress. This increased stress is applied to the liquid film between the grains. Additionally, surface tension exists within the liquid film between two adjacent grains during the final stage of solidification. This surface tension induces a compressive stress σ on the liquid film and can be expressed by [39]:

$$\sigma = \frac{2\gamma}{b} \qquad (5)$$

where γ is the surface tension, and b is the thickness of the liquid film between two grains. When smaller grains are present, the grain boundary area significantly increases, and the liquid film thickness is smaller compared to bigger grains. According to Eq. 5, the compressive stress acting on the liquid film between two grains is therefore lower with large grains. When the tensile stress caused by thermal contraction is larger than the compressive stress, cracking will occur in the liquid film between two grains. Therefore, the occurrence of the cracks is more likely in the coarse grained structure.

Inside the melt pools of the base and ZV alloys, the grains are almost columnar and their size is large (Figure 4-6c and 4-7c). The addition of TiB_2 particles shifts the grain growth from columnar to equiaxed (Figure 4-8), significantly reducing the grain size in the B-3TiB and ZV-6TiB alloys. In terms of the effectiveness of grain refinement, the growth restriction factor (GRF) serves as a powerful parameter [40]. While Ti has the highest GRF, V, and Zr also exhibit higher GRF values compared to Cu. The higher concentrations of Ti, Zr, and V in the ZV-6TiB alloy compared to the B-3TiB alloy effectively contribute to the significant grain size reduction observed after LSR, as shown in Figure 4-6 and 4-7. The main reason for crack mitigation is the grain structure modification. A schematic of the cracking mechanism in terms of grain structure and size is shown in Figure 4-14. In this

illustration, d_1, d_2, and b_1, b_2 are the grain sizes and liquid film thicknesses in the final stages of solidification.

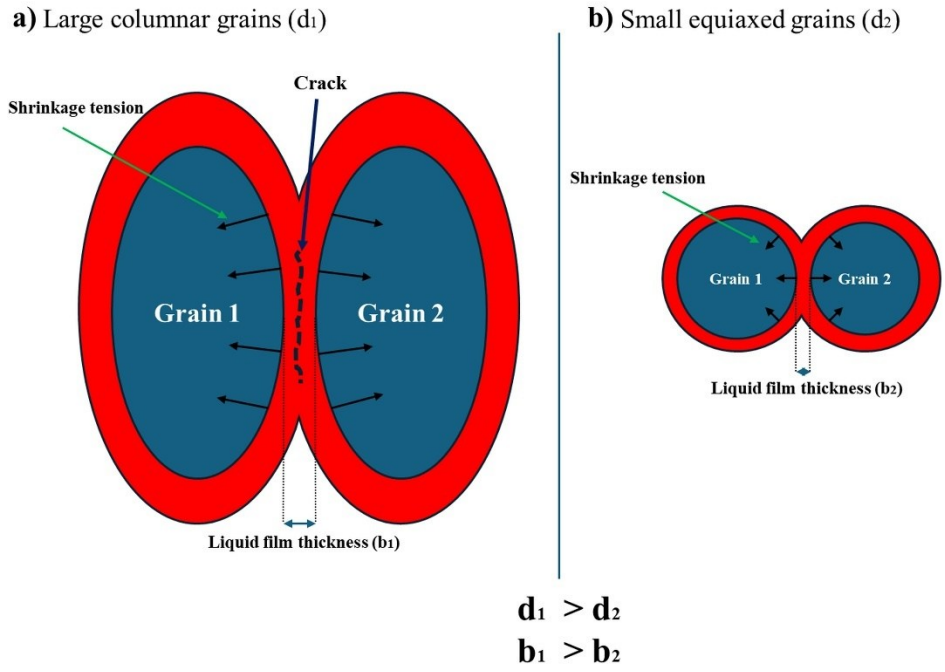

Figure 4-14: Schematic illustration of the cracking mechanism in the final stages of solidification: a) large columnar grains, b) small equiaxed grains.

4.4.3 Advantage and limitation

Al-Si-based AlSi10Mg alloys are the most commonly used aluminum alloys in the additive SLM process owing to their excellent processability and adaptability. In industrial applications involving complex-shaped materials, a stress-relieving treatment is often adopted because of the high residual stresses in the printed components. However, this treatment leads to a significant reduction in the mechanical properties, which necessitates a subsequent T6 heat treatment to restore the mechanical properties. Despite numerous efforts to optimize the heat treatments of conventional AlSi10Mg alloys, the mechanical properties

after a T6 treatment remain relatively low with yield strengths (YS) typically remaining below 250 MPa [10].

A comparison of T6 mechanical properties between AlSi10Mg and the Al-Cu alloys in this study reveals a notable difference of mechanical performance. As shown in Table 4-2, the microhardness of the B-3TiB and ZV-6TiB alloys reached 117-130 HV, whereas the SLMed AlSi10Mg alloys typically ranged from 60 to 100 HV. This indicates that the Al-Cu alloys in the present study surpass the T6 mechanical properties of conventional AlSi10Mg alloys by at least 15-30%. This improvement is most likely attributed to the fine grain strengthening and nanoscale θ′/θ″ precipitation strengthening, particularly in the ZV-6TiB alloy. The TiB-containing Al-Cu alloys in this study present a promising opportunity for new additive manufacturing materials with high mechanical performance while maintaining good processability.

Table 4-2: Comparison of mechanical properties between the current Al-Cu alloys and conventional SLMed AlSi10Mg alloys

	Alloys	HV	Heat treatment	References
1	B-3TiB	117	T6	Present study
2	ZV-6TiB	130	T6	Present study
2	AlSi10Mg	80*	T6	[41]
3	AlSi10Mg	83	T6	[42]
4	AlSi10Mg	79	T6	[43]
5	AlSi10Mg	100	T6	[44]
6	AlSi10Mg	70*	Stress relief	[45]
7	AlSi10Mg	88	Stress relief	[46]

* Converted from the yield stress, assuming that the yield stress is three times the hardness.

The high-strength Al-Cu alloys are generally susceptible to solidification cracks during rapid solidification [15]. The hot tearing susceptibility and microstructural evolution of Al-Cu 224 alloys during rapid solidification were investigated using laser surface

remelting. This study provided a scientific basis and practical method for developing Al-Cu alloys with good processability for rapid solidification processes, particularly the SLM process. The results revealed that the addition of appropriate amounts of TiB grain refiner could eliminate the solidification cracks and significantly improve the grain structure of Al-Cu alloys during the LSR process.

The approach used for developing B-3TiB and ZV-6TiB alloys offers significant potential for designing high-strength Al-Cu alloys tailored for SLM processes. Al-Cu alloys typically require high energy density [47], low scan speed, and low power during the SLM process, which increases production time and costs. The modification presented in this study improves the processability of 224 aluminum alloys, enabling more efficient melting and solidification. This advancement can potentially reduce the energy input required, thereby lowering both production time and costs, while enhancing the final components' mechanical performance. Such improvements could pave the way for broader industrial adoption of Al-Cu alloys in SLM. Nevertheless, the implications and limitations of this study must be carefully considered. The enhancement of cracking resistance during rapid solidification with increasing TiB_2 particle content in the cracking-prone Al-Cu alloys is undeniable. However, the use of laser-surface-melted tracks in the current approach did not take into account the impacts of powder-based processing, thermal cycling, and the overlapping of re-melted tracks in subsequent layers, as in a typical SLM process. Therefore, the results herein provide only a first estimation of the attainable T6 strength and processing performance of these TiB-modified Al-Cu 224 alloys in a real SLM process. In this study, the laser surface remelting (LSR) process was used as a practical method to evaluate the grain refinement and mechanical properties of the modified alloys. However, a comprehensive evaluation under

real SLM production conditions remains a key limitation and will be the primary focus of our future research.

4.5 Conclusions

In the present study, the microstructural evolution, hot tearing susceptibility, and mechanical properties of five Al-Cu 224 alloys with and without TiB grain refiner additions were investigated using a laser surface remelting method. The following conclusions were drawn from the main findings:

1- The addition of 0.3-0.65 wt% Ti to Al-Cu 224 alloys by means of grain refinement with Al-5Ti-1Bsignificantly reduced the hot tearing susceptibility during laser-based rapid solidification. With sufficient amounts of TiB grain refiner, solidification cracks could be completely eliminated in these Al-Cu alloys, making them promising high-strength alloys for the SLM process.

2- The introduction of TiB_2 particles into the melt pools from the TiB grain refiner changed the grain morphology from a coarse columnar to a fine equiaxed structure and significantly reduced the grain size. Following TiB-modification, the grain sizes were reduced from 13-15 μm in the base alloys to 5.5 and 3.2 μm in the alloys with 0.3 wt% Ti (B-3TiB) and 0.65 wt% Ti (ZV-6TiB) additions, respectively.

3- The modified B-3TiB and ZV-6TiB alloys reached hardness values of 117 and 130 HV after a T6 heat treatment, which surpassed the conventional AlSi10Mg alloys by at least 15-30%. This was attributed to extra strengthening contributions from fine equiaxed grains and from nanoscale θ′/θ″precipitation.

4- The laser surface remelting used in this study provides a simple and practical methodology to assess and optimize the processability and mechanical properties of high-strength aluminum alloys during laser-based rapid solidification processes. This study presents modified 224 alloys suitable for practical SLM production, which will be a focus of our future research efforts.

References

[1] Q. Lv, F. Zhang, H. Wei, Z. Li, J. Zhang, Effect of rare earth (La, Ce, Nd, Sc) on strength and toughness of 6082 aluminum alloy, Vacuum 215 (2023) 112333.https://doi.org/10.1016/j.vacuum.2023.112333

[2] X. You, Z. Xing, S. Jiang, Y. Zhu, Y. Lin, H. Qiu, R. Nie, J. Yang, D. Hui, W. Chen, Y. Chen, A review of research on aluminum alloy materials in structural engineering, Developments in the Built Environment 17 (2024) 100319.https://doi.org/10.1016/j.dibe.2023.100319

[3] K. Liu, X. Cao, X.G. Chen, Tensile Properties of Al-Cu 206 Cast Alloys with Various Iron Contents, Metallurgical and Materials Transactions A 45(5) (2014) 2498-2507.https://doi.org/10.1007/s11661-014-2207-3

[4] S. Gairola, R. Jayaganthan, J. Ajay, Laser powder bed fusion on Ti modified Al 2024 alloy: Influence of build orientation and T6 treatment on mechanical behaviour, microstructural features and strengthening mechanisms, Materials Science and Engineering: A 896 (2024) 146296.https://doi.org/10.1016/j.msea.2024.146296

[5] H. Yu, F. Lyu, X. Jiang, Y. Jin, Y. Xu, Mechanical properties and microscopic mechanisms of 2219-T6 aluminum alloy under dynamic tension with cryogenic temperatures, Materials Science and Engineering: A 891 (2024) 145920.https://doi.org/10.1016/j.msea.2023.145920

[6] J. Wei, C. He, R. Dong, N. Tian, G. Qin, Enhancing mechanical properties and defects elimination in 2024 aluminum alloy through interlayer friction stir processing in wire arc additive manufacturing, Materials Science and Engineering: A 901 (2024) 146582.https://doi.org/10.1016/j.msea.2024.146582

[7] D. Li, K. Liu, J. Rakhmonov, X.G. Chen, Enhanced thermal stability of precipitates and elevated-temperature properties via microalloying with transition metals (Zr, V and Sc) in Al–Cu 224 cast alloys, Materials Science and Engineering: A 827 (2021) 142090.https://doi.org/10.1016/j.msea.2021.142090

[8] L. Cui, K. Liu, Z. Zhang, X.G. Chen, Enhanced elevated-temperature mechanical properties of hot-rolled Al–Cu alloys: effect of zirconium addition and homogenization, Journal of Materials Science 58(27) (2023) 11424-11439.https://doi.org/10.1007/s10853-023-08728-5

[9] P. Hu, K. Liu, L. Pan, X.G. Chen, Effects of individual and combined additions of transition elements (Zr, Ti and V) on the microstructure stability and elevated-temperature properties of Al–Cu 224 cast alloys, Materials Science and Engineering: A 867 (2023) 144718.https://doi.org/10.1016/j.msea.2023.144718

[10] N.T. Aboulkhair, M. Simonelli, L. Parry, I. Ashcroft, C. Tuck, R. Hague, 3D printing of Aluminium alloys: Additive Manufacturing of Aluminium alloys using selective laser

melting, Progress in Materials Science 106 (2019).https://doi.org/10.1016/j.pmatsci.2019.100578

[11] S. Dixit, S. Liu, Laser Additive Manufacturing of High-Strength Aluminum Alloys: Challenges and Strategies, Journal of Manufacturing and Materials Processing 6(6) (2022) 156.https://doi.org/10.3390/jmmp6060156

[12] Q. Jia, P. Rometsch, S. Cao, K. Zhang, X. Wu, Towards a high strength aluminium alloy development methodology for selective laser melting, Materials & Design 174 (2019) 107775.https://doi.org/10.1016/j.matdes.2019.107775

[13] J.H. Martin, B.D. Yahata, J.M. Hundley, J.A. Mayer, T.A. Schaedler, T.M. Pollock, 3D printing of high-strength aluminium alloys, Nature 549(7672) (2017) 365-369.https://doi.org/10.1038/nature23894

[14] P.A. Rometsch, Y. Zhu, X. Wu, A. Huang, Review of high-strength aluminium alloys for additive manufacturing by laser powder bed fusion, Materials & Design 219 (2022) 110779.https://doi.org/10.1016/j.matdes.2022.110779

[15] A. Mehta, L. Zhou, T. Huynh, S. Park, H. Hyer, S. Song, Y. Bai, D.D. Imholte, N.E. Woolstenhulme, D.M. Wachs, Y. Sohn, Additive manufacturing and mechanical properties of the dense and crack free Zr-modified aluminum alloy 6061 fabricated by the laser-powder bed fusion, Additive Manufacturing 41 (2021) 101966.https://doi.org/10.1016/j.addma.2021.101966

[16] Z. Hu, X. Nie, Y. Qi, H. Zhang, H. Zhu, Cracking criterion for high strength Al–Cu alloys fabricated by selective laser melting, Additive Manufacturing 37 (2021) 101709.https://doi.org/10.1016/j.addma.2020.101709

[17] J. Elambasseril, M.J. Benoit, S. Zhu, M.A. Easton, E. Lui, C.A. Brice, M. Qian, M. Brandt, Effect of process parameters and grain refinement on hot tearing susceptibility of high strength aluminum alloy 2139 in laser powder bed fusion, Progress in Additive Manufacturing (2022).https://doi.org/10.1007/s40964-021-00259-2

[18] M.J. Benoit, M.A. Whitney, S.M. Zhu, D. Zhang, M.R. Field, M.A. Easton, The beneficial effect of minor iron additions on the crack susceptibility of rapidly solidified aluminum alloy 6060 toward additive manufacturing applications, Materials Characterization 205 (2023).https://doi.org/10.1016/j.matchar.2023.113287

[19] Y. Sun, J. Wang, Y. Shi, Q. Fei, N. Zhao, C. Ni, J. Wu, Y. Dong, T. Dai, H. Ding, M. Hao, An SLM-processed Er- and Zr- modified Al–Mg alloy: Microstructure and mechanical properties at room and elevated temperatures, Materials Science and Engineering: A 883 (2023) 145485.https://doi.org/10.1016/j.msea.2023.145485

[20] S.Z. Uddin, L.E. Murr, C.A. Terrazas, P. Morton, D.A. Roberson, R.B. Wicker, Processing and characterization of crack-free aluminum 6061 using high-temperature heating in laser powder bed fusion additive manufacturing, Additive Manufacturing 22 (2018) 405-415.https://doi.org/10.1016/j.addma.2018.05.047

[21] Q. Tan, Y. Liu, Z. Fan, J. Zhang, Y. Yin, M.-X. Zhang, Effect of processing parameters on the densification of an additively manufactured 2024 Al alloy, Journal of Materials Science & Technology 58 (2020) 34-45.https://doi.org/10.1016/j.jmst.2020.03.070

[22] S.Y. Zhou, Y. Su, H. Wang, J. Enz, T. Ebel, M. Yan, Selective laser melting additive manufacturing of 7xxx series Al-Zn-Mg-Cu alloy: Cracking elimination by co-incorporation of Si and TiB2, Additive Manufacturing 36 (2020) 101458.https://doi.org/10.1016/j.addma.2020.101458

[23] T. Zheng, S. Pan, N. Murali, B. Li, X. Li, Selective laser melting of novel 7075 aluminum powders with internally dispersed TiC nanoparticles, Materials Letters 319 (2022) 132268.https://doi.org/10.1016/j.matlet.2022.132268

[24] J. Zhang, W. Yuan, B. Song, S. Yin, X. Wang, Q. Wei, Y. Shi, Towards understanding metallurgical defect formation of selective laser melted wrought aluminum alloys, Advanced Powder Materials 1(4) (2022) 100035.https://doi.org/10.1016/j.apmate.2022.100035

[25] H. Zhang, H. Zhu, X. Nie, J. Yin, Z. Hu, X. Zeng, Effect of Zirconium addition on crack, microstructure and mechanical behavior of selective laser melted Al-Cu-Mg alloy, Scripta Materialia 134 (2017) 6-10.https://doi.org/10.1016/j.scriptamat.2017.02.036

[26] X. Liu, Y. Liu, Z. Zhou, K. Wang, Q. Zhan, X. Xiao, Grain refinement and crack inhibition of selective laser melted AA2024 aluminum alloy via inoculation with TiC–TiH2, Materials Science and Engineering: A 813 (2021) 141171.https://doi.org/10.1016/j.msea.2021.141171

[27] G. Del Guercio, D.G. McCartney, N.T. Aboulkhair, S. Robertson, R. Maclachlan, C. Tuck, M. Simonelli, Cracking behaviour of high-strength AA2024 aluminium alloy produced by Laser Powder Bed Fusion, Additive Manufacturing 54 (2022) 102776.https://doi.org/10.1016/j.addma.2022.102776

[28] Q. Jia, P. Rometsch, S. Cao, K. Zhang, A. Huang, X. Wu, Characterisation of AlScZr and AlErZr alloys processed by rapid laser melting, Scripta Materialia 151 (2018) 42-46.https://doi.org/10.1016/j.scriptamat.2018.03.035

[29] D. Carluccio, M.J. Bermingham, Y. Zhang, D.H. StJohn, K. Yang, P.A. Rometsch, X. Wu, M.S. Dargusch, Grain refinement of laser remelted Al-7Si and 6061 aluminium alloys with Tibor® and scandium additions, Journal of Manufacturing Processes 35 (2018) 715-720.https://doi.org/10.1016/j.jmapro.2018.08.030

[30] M. Roscher, Z. Sun, E.A. Jägle, Designing Al alloys for laser powder bed fusion via laser surface melting: Microstructure and processability of 7034 and modified 2065, Journal of Materials Processing Technology 326 (2024) 118334.https://doi.org/10.1016/j.jmatprotec.2024.118334

[31] M.A. Easton, M.A. Gibson, S. Zhu, T.B. Abbott, An A Priori Hot-Tearing Indicator Applied to Die-Cast Magnesium-Rare Earth Alloys, Metallurgical and Materials Transactions A 45(8) (2014) 3586-3595.https://doi.org/10.1007/s11661-014-2272-7

[32] S. Zhang, S. Zhang, F. Li, Y. Wang, Z. Li, Y. Chen, L. Wang, B. Liu, P. Bai, Study on defects of Zr-containing Al–Cu–Mn–Mg alloys manufactured by selective laser melting,

Journal of Materials Research and Technology 29 (2024) 119-129.https://doi.org/10.1016/j.jmrt.2024.01.073

[33] M. Easton, D. StJohn, Grain refinement of aluminum alloys: Part I. the nucleant and solute paradigms—a review of the literature, Metallurgical and Materials Transactions A 30(6) (1999) 1613-1623.https://doi.org/10.1007/s11661-999-0098-5

[34] Q. Tan, J. Zhang, Q. Sun, Z. Fan, G. Li, Y. Yin, Y. Liu, M.-X. Zhang, Inoculation treatment of an additively manufactured 2024 aluminium alloy with titanium nanoparticles, Acta Mater 196 (2020) 1-16.https://doi.org/10.1016/j.actamat.2020.06.026

[35] Z. Fan, C. Li, H. Yang, Z. Liu, Effects of TiC nanoparticle inoculation on the hot-tearing cracks and grain refinement of additively-manufactured AA2024 Al alloys, Journal of Materials Research and Technology 19 (2022) 194-207.https://doi.org/10.1016/j.jmrt.2022.05.039

[36] Z. Wang, X. Lin, N. Kang, Y. Hu, J. Chen, W. Huang, Strength-ductility synergy of selective laser melted Al-Mg-Sc-Zr alloy with a heterogeneous grain structure, Additive Manufacturing 34 (2020) 101260.https://doi.org/10.1016/j.addma.2020.101260

[37] X. Wang, Z. Liu, W. Dai, Q. Han, On the Understanding of Aluminum Grain Refinement by Al-Ti-B Type Master Alloys, Metallurgical and Materials Transactions B 46(4) (2015) 1620-1625.https://doi.org/10.1007/s11663-014-0252-3

[38] J. Zhang, J. Gao, B. Song, L. Zhang, C. Han, C. Cai, K. Zhou, Y. Shi, A novel crack-free Ti-modified Al-Cu-Mg alloy designed for selective laser melting, Additive Manufacturing 38 (2021) 101829.https://doi.org/10.1016/j.addma.2020.101829

[39] Y. Li, H. Li, L. Katgerman, Q. Du, J. Zhang, L. Zhuang, Recent advances in hot tearing during casting of aluminium alloys, Progress in Materials Science 117 (2021) 100741.https://doi.org/10.1016/j.pmatsci.2020.100741

[40] Z. Lei, S. Wen, H. Huang, W. Wei, Z. Nie, Grain Refinement of Aluminum and Aluminum Alloys by Sc and Zr, Metals 13(4) (2023) 751.https://doi.org/10.3390/met13040751

[41] N.T. Aboulkhair, I. Maskery, C. Tuck, I. Ashcroft, N.M. Everitt, The microstructure and mechanical properties of selectively laser melted AlSi10Mg: The effect of a conventional T6-like heat treatment, Materials Science and Engineering: A 667 (2016) 139-146.https://doi.org/10.1016/j.msea.2016.04.092

[42] L.F. Wang, J. Sun, X.L. Yu, Y. Shi, X.G. Zhu, L.Y. Cheng, H.H. Liang, B. Yan, L.J. Guo, Enhancement in mechanical properties of selectively laser-melted AlSi10Mg aluminum alloys by T6-like heat treatment, Materials Science and Engineering: A 734 (2018) 299-310.https://doi.org/10.1016/j.msea.2018.07.103

[43] N.T. Aboulkhair, C. Tuck, I. Ashcroft, I. Maskery, N.M. Everitt, On the Precipitation Hardening of Selective Laser Melted AlSi10Mg, Metallurgical and Materials Transactions A 46(8) (2015) 3337-3341.https://10.1007/s11661-015-2980-7

[44] C.D. Clement, J. Masson, A.S. Kabir, Effects of Heat Treatment on Microstructure and Mechanical Properties of AlSi10Mg Fabricated by Selective Laser Melting Process, Journal

of Manufacturing and Materials Processing 6(3) (2022) 52.https://doi.org/10.3390/jmmp6030052

[45] P. Van Cauwenbergh, V. Samaee, L. Thijs, J. Nejezchlebova, P. Sedlak, A. Ivekovic, D. Schryvers, B. Van Hooreweder, K. Vanmeensel, Unravelling the multi-scale structure-property relationship of laser powder bed fusion processed and heat-treated AlSi10Mg, Sci Rep 11(1) (2021) 6423.https://doi.org/10.1038/s41598-021-85047-2

[46] N. Takata, H. Kodaira, K. Sekizawa, A. Suzuki, M. Kobashi, Change in microstructure of selectively laser melted AlSi10Mg alloy with heat treatments, Materials Science and Engineering: A 704 (2017) 218-228.https://doi.org/10.1016/j.msea.2017.08.029

[47] H. Zhang, H. Zhu, T. Qi, Z. Hu, X. Zeng, Selective laser melting of high strength Al–Cu–Mg alloys: Processing, microstructure and mechanical properties, Materials Science and Engineering: A 656 (2016) 47-54.https://doi.org/10.1016/j.msea.2015.12.101

Chapter 5

Conclusions and recommendations

5.1 General conclusions

This project focused on the production of Al-Si and Al-Cu alloys using Selective Laser Melting (SLM), aiming to achieve strength levels exceeding those of the conventional AlSi10Mg alloy. The influence of heat treatments on the properties of the alloys produced in this study was systematically examined. Based on the experimental data and analyses, the following conclusions were drawn:

1- An AlSi10MgMn alloy with 0.5 wt% Mn was successfully fabricated using the SLM process for the first time. This alloy demonstrated yield strength (YS) values of 299 MPa in the as-fabricated (F) condition, 386 MPa in the directly-aged (T5) condition, and 321 MPa in the solution-treated and aged (T6) condition. The tensile properties of the AlSi10MgMn alloy significantly exceeded those of conventional AlSi10Mg alloys under comparable F, T5, and T6 conditions.

2- In the as-fabricated (F) condition, fine Si-rich nanoparticles were observed within the aluminum cells, accompanied by fine α-Al(Mn,Fe)Si intermetallic particles dispersed in the Si-rich network of the AlSi10MgMn alloy. These microstructural features, combined with substantial solid solution strengthening, contributed to an improved yield strength (YS) compared to conventional AlSi10Mg alloys.

3- In the T5 condition, a high density of Si-rich nanoparticles and MgSi-based precipitates was observed within the aluminum cells of AlSi10MgMn alloy, while the continuous Si-rich network remained intact. Precipitation strengthening, primarily driven by these nanosized Si-rich and MgSi-based precipitates, emerged as the dominant strengthening mechanism, with the Si-rich nanoparticles playing a particularly significant role.

4- In the F and T5 conditions, the addition of Mn led to the formation of α-Al(Mn,Fe)Si particles within the Si-rich eutectic network. These intermetallic particles enhanced the strength of the AlSi10MgMn alloy by creating additional obstacles to dislocation movement. Atom probe tomography (APT) confirmed the presence of these particles in the Si-rich network. It was demonstrated that these particles can improve the strain hardening rate of the Mn-modified alloy compared to the base alloy.

5- The presence of Mn in the matrix can promote the formation of Si-rich precipitates in the F and T5 conditions. Mn and Si exhibit a negative enthalpy of mixing, which facilitates the attraction of Si atoms by Mn from the supersaturated solid solution. This enhances the tendency for the formation of Si-rich particles. The presence of Mn can therefore provide smaller precipitates with a higher number density in the AlSi10MgMn alloy compared to the common AlSi10Mg alloy, which can provide a better barrier for dislocation movement and hence a higher YS. The higher number density of Si-rich precipitates in the Mn-modified alloy has been demonstrated by means of TEM and APT observations.

6- While a high amount of MgSi-based precipitates were present in AlSi10Mg and AlSi10MgMn alloys after the T6 heat treatment, the presence of α-Al(Mn,Fe)Si dispersoids in the presence of Mn contributed to additional strengthening in AlSi10MgMn alloy compared to the common AlSi10Mg alloy.

7- The forth section of this thesis utilized laser surface remelting, a straightforward and effective method to evaluate and enhance the processability and mechanical characteristics of high-strength Al-Cu 224 aluminum alloys in laser-based rapid solidification processes. The addition of 0.3-0.65 wt% Ti to Al-Cu 224 alloys by means of grain refinement with Al-5Ti-1B significantly reduced the hot tearing susceptibility during laser-based rapid solidification. With sufficient amounts of TiB grain refiner, solidification cracks could be completely eliminated in these Al-Cu 224 alloys, making them promising high-strength alloys for the SLM process.

8- The introduction of TiB_2 particles into the melt pools from the TiB grain refiner changed the grain morphology from a coarse columnar to a fine equiaxed structure and significantly reduced the grain size. Following TiB-modification, the grain sizes were reduced from 13-15 μm in the base alloys to 5.5 and 3.2 μm in the alloys with 0.3 wt% Ti (B-3TiB) and 0.65 wt% Ti (ZV-6TiB) additions, respectively.

9- The modified B-3TiB and ZV-6TiB alloys reached hardness values of 117 and 130 HV after a T6 heat treatment, which surpassed the conventional AlSi10Mg alloys by at least 15-30%. This was attributed to extra strengthening contributions from fine equiaxed grains and from nanoscale θ′/θ″precipitation.

5.2 Recommendations

Based on the recent findings of this study, the following recommendations could be given for future work in this area.

1- The newly developed AlSi10MgMn alloy for SLM production is a promising choice for complex-shaped components in high-tech industries. Comparing its fatigue behavior with conventional alloys, such as AlSi10Mg and AlSi12, can provide a comprehensive dataset, offering valuable insights for industrial and engineering applications.

2- Previous studies have demonstrated that incorporating a grain refiner can effectively reduce the grain size in AlSi10Mg alloy during the SLM process. Besides, the current study investigates the impact of Mn modification under various heat treatment conditions. The synergistic effect of combining a grain refiner with Mn modification can further enhance the alloy's mechanical properties, paving the way for new opportunities in its application within SLM.

3- The newly developed ZV-6TiB and B-TiB alloys, designed for SLM using LSR, hold significant potential for high-tech industries requiring complex-shaped components. Conducting fatigue and creep tests at elevated temperatures is essential to fully evaluate their performance. Such testing would generate a comprehensive dataset, offering valuable insights into the industrial and engineering applications of these advanced SLM-produced alloys.

4- Previous studies have shown that Si can enhance the fluidity of the aluminum melt, which is crucial for SLM to ensure uniform layer formation and avoid defects like porosity

or incomplete melting. Modifying the ZV-6TiB alloy in this study with microalloying (up to 0.5%wt) with Si will be a good topic to check the processability of this alloy during SLM.

List of publications

Journal papers:

1. Evolution of mechanical properties and microstructure of selective laser melted AlSi10MgMn alloy with different post heat treatments, “Esmaeil Pourkhorshid, Paul Rometsch, X.-Grant Chen” **Materials Science and Engineering: A, 147249 (2024).**
2. Effect of Mn on Microstructural Characteristics and Mechanical Behavior of AlSi10Mg Alloys Produced by Selective Laser Melting, “Esmaeil Pourkhorshid, Paul Rometsch, X.-Grant Chen” **under internal review.**
3. Laser-based additive manufacturing processability and mechanical properties of Al-Cu 224 alloys with TiB grain refiner additions, “Esmaeil Pourkhorshid, Paul Rometsch, X.-Grant Chen” **Materials 18 (2025) 516.**

Scientific Posters:

1. Feasibility of production of high strength aluminum alloys by laser powder bed fusion as an additive manufacturing process, “Esmaeil Pourkhorshid, Paul Rometsch, X.-Grant Chen” REGAL Students’ Day, Canada, November. 2021.
2. Mechanical properties and microstructure of AlSi10Mg alloy after Selective Laser Melting, “Esmaeil Pourkhorshid, Paul Rometsch, X.-Grant Chen” REGAL Students’ Day, Canada, October. 2022.

3. Investigating the Impact of Mn Modification on Microstructure and Mechanical Properties of Selective Laser Melted AlSi10Mg Alloy: As-Built and T6 conditions, "Esmaeil Pourkhorshid, Paul Rometsch, X.-Grant Chen" REGAL Students' Day, Canada, October. 2023 (Awarded 3rd posters prize).
4. Microstructure evolution of Al-Cu 224 alloy with Ti-B grain refiner additions for SLM applications, "Esmaeil Pourkhorshid, Paul Rometsch, X.-Grant Chen" REGAL Students' Day, Canada, October. 2024 (Awarded ICSOBA posters prize).

Patents and inventions:

1- AlSiMgMn alloy for additive manufacturing, "Paul Arthur Rometsch, X-Grant Chen, Esmaeil Pourkhorshid", CA3181573A1 and US20240149348A1 patent applications published 2024/05/09.

2- High-Strength Alloy For Additive Manufacturing, "Paul Arthur Rometsch, X-Grant Chen, Esmaeil Pourkhorshid" UQAC invention declaration 2024, with US provisional patent application 63/621731 filed in January 2024, and PCT patent application filed in January 2025.

3- High Strength SiC-reinforced Al-based Metal Matrix Composites for Additive Manufacturing, "Paul Arthur Rometsch, X-Grant Chen, Abhishek Ghosh, Esmaeil Pourkhorshid" UQAC invention declaration 2024